

The Pennsylvania State University

The Graduate School

College of Engineering

**VIBRATION ENERGY HARVESTING FROM ROTORCRAFT DRIVE
SYSTEMS USING THERMOELECTRIC CONVERSION OF HEAT
GENERATED BY MECHANICAL DAMPING**

A Thesis in

Aerospace Engineering

by

Raheel S. Mahmood

© 2014 Raheel S. Mahmood

Submitted in Partial Fulfillment
of the Requirements
for the Degree of

Master of Science

December 2014

The thesis of Raheel S. Mahmood was reviewed and approved* by the following:

Edward C. Smith
Professor of Aerospace Engineering
Thesis Co-Adviser

Namiko Yamamoto
Assistant Professor of Aerospace Engineering

George A. Lesieutre
Professor of Aerospace Engineering
Head of the Department of Aerospace Engineering
Thesis Co-Adviser

*Signatures are on file in the Graduate School.

Abstract

Energy harvesting from ambient structural vibrations on rotorcraft continues to generate increasing interest due to its potential use in powering wireless sensors for applications such as structural health monitoring. Vibration energy harvesters developed in the past have used piezoelectric or electromagnetic devices to convert mechanical work into electrical energy for use by accelerometers, strain gauges, or other devices. Vibrations from rotorcraft drive systems typically occur within a frequency range of 500 to 3000 Hz as a result of transmission gear meshing.

An alternative method for vibration energy harvesting employs a thermoelectric generator which converts thermal energy dissipated by a damped mechanical oscillator installed on the vibrating structure to electrical energy. Damping of the oscillator is provided by either a viscoelastic spring or by forces due to eddy current induction in a metal plate moving relative to a magnetic field.

Two harvester designs implementing oscillators damped by either viscoelastic or electromagnetic forces are described, and one-dimensional analytical models are developed to model heat generation and conduction for each design. Test articles are designed for experimental evaluation of the two heating methods, and the analytical models are used to predict the behavior of the test articles. An analogous thermal circuit model is used to model transient heat flow, and a finite element model is used to model magnetic flux distribution to aid in prediction of temperature response of the test articles.

Experimental characterization of a stiff, low damping elastomer indicated decreasing stiffness and loss factor with increasing base acceleration. The average measured stiffness was found to be slightly lower than the expected value based on the material specification, and the average loss

factor was also lower than expected but aligned with the expected value at low acceleration levels. An increase in the temperature of the viscoelastic test article driven at resonance was recorded at a slightly lower rate than predicted.

Induction heating measurements of aluminum plates of varying thicknesses showed an increase in surface heating with plate thickness. The measured temperature over the test period increased quadratically with relative velocity, as predicted by the analytical model. Measurement of the power output of two thermoelectric generators with changing surface temperature revealed differences in the response for upward and downward temperature change, indicating nonlinearities in the behavior of these units.

Results of the study showed limited applicability of the considered approaches for high frequency vibration energy harvesting applications due to the long time required for heating of the elastomer, or the high velocities required for magnetic induction heating. Suggestions for improving the performance and efficiency of the proposed harvesters are provided along with recommendations for future work.

Contents

List of Figures	ix
List of Tables	xii
List of Symbols	xiii
Acknowledgments	xv
Chapter 1: Introduction	1
1.1 Electromagnetic harvesters	2
1.1.1 Electromagnetic power generation	2
1.1.2 Electromagnetic vibration energy harvesters	4
1.2 Piezoelectric harvesters	6
1.2.1 The piezoelectric effect	7
1.2.2 Piezoelectric vibration energy harvesters	9
1.2.3 Multi-modal and composite devices	10
1.3 Heat generation and harvesting	12
1.3.1 Viscoelastic materials	13
1.3.1.1 Dynamic material properties	14
1.3.1.2 Nonlinearity with frequency and temperature	15
1.3.2 Eddy currents and induction	16

1.3.2.1	Material electrical properties	17
1.3.2.2	Induction heating	18
1.3.3	Thermal energy harvesting	19
1.3.3.1	Thermoelectric generator operation	19
1.4	Objectives	20
1.4.1	Approach	21
Chapter 2: Analysis Methods		23
2.1	Harvester description	23
2.2	Forced linear motion	27
2.3	Heat generation	28
2.3.1	Viscoelastic heating	28
2.3.2	Magnetic induction heating	29
2.3.2.1	Electrical resistance and Joule heating	30
2.3.2.2	Heating in a uniform magnetic field	31
2.3.2.3	Heating in a varying magnetic field	32
2.4	Linear heat flow model	33
2.4.1	Steady-state heat conduction	34
2.4.2	Transient heat flow	36
2.4.2.1	Heat conduction from elastomer	37
2.4.2.2	Heat conduction from magnetic induction heater	37
2.5	Test articles	39
2.5.1	Visco-thermoelectric test article	39
2.5.2	Magneto-thermoelectric test article	40
2.5.2.1	Magnetic field estimation	41
Chapter 3: Experimental Facilities and Methods		44
3.1	Concept validation hardware	44

3.1.1	Visco-thermoelectric test fixture	44
3.1.2	Magneto-thermoelectric test fixture	46
3.2	Test equipment configuration	48
3.2.1	Control and data acquisition	50
3.2.1.1	Software settings	51
3.2.1.2	Output and monitoring	51
3.2.1.3	Recording data	53
3.2.2	Vibration measurement	53
3.2.3	Thermal characterization and temperature measurement	54
3.3	Test description	56
3.3.1	Elastomer characterization	56
3.3.1.1	Data preparation	56
3.3.1.2	Transfer function estimation and parameter identification	58
3.3.2	Elastomer heating	59
3.3.3	Induction heating	60
3.3.4	Power output	61
Chapter 4:	Results	63
4.1	Experimental characterization of elastomer	63
4.2	Elastomer heating simulation	68
4.2.1	Notional test article	68
4.2.2	Actual test article	72
4.3	Induction heating simulation	75
4.3.1	Magnetic field analysis	75
4.3.2	Temperature model	75
4.4	Heat generation measurements	80
4.4.1	Viscoelastic heating	80
4.4.2	Induction heating	81

4.5 Thermoelectric generator characterization	83
Chapter 5: Conclusions	86
5.1 Summary of results	86
5.1.1 Elastomer characterization and heating	87
5.1.2 Magnetic induction heating	88
5.1.3 Power generation	88
5.2 Feasibility	89
5.3 Future related research	89
References	95
Appendix A: MATLAB Code	96
A.1 Temperature prediction from heating model	96
A.1.1 VTE test article response	96
A.1.2 MTE test article response	99
A.2 Data analysis	99
A.2.1 Elastomer characterization	99
A.2.2 Heating tests	101
A.2.3 Referenced functions	101
Appendix B: LabVIEW Code	105

List of Figures

1.1	Simple electromagnetic power generator	3
1.2	Cantilever magnet generator	3
1.3	Electromagnetic harvester power output vs. operating frequency	5
1.4	LORD-MicroStrain Magnetoinductive Vibration Energy Harvester (MVEH)	6
1.5	Material axis definitions for a thin piezoelectric sheet	7
1.6	Piezoelectric material integrated into cantilever beam with tip mass	7
1.7	LORD-MicroStrain Piezoelectric Vibration Energy Harvester (PVEH)	9
1.8	Cantilever beam piezoelectric vibration energy harvester using single crystal material	10
1.9	Integrated piezoelectric and electromagnetic vibration energy harvester	11
1.10	Non-linear piezoelectric vibration energy harvester)	12
1.11	Piezo-magneto-elastic harvester design	12
1.12	Dynamic heating of cyclically loaded elastomer	13
1.13	Variation in elastomer properties with temperature	16
1.14	Non-linearity in complex modulus of an elastomer	17
1.15	Thermoelectric generator implementation	19
1.16	Thermoelectric generator architecture	20
1.17	Energy flow for conceptual vibration energy harvester	21
2.1	Vibration energy harvesting concept	24
2.2	Conceptual drawings of vibration energy harvesting devices (not to scale)	26
2.3	Transient heat flow circuit model for elastomer test article	38

2.4	Heat flow model for metal plate heated by induction	38
2.5	Concept for elastomer test article showing deformed oscillator shape (exaggerated) .	40
2.6	Induction heating test article conceptual configurations and flux path (not to scale) .	41
2.7	Induction heating permanent magnet fixture drawing and mesh for finite element magnetics analysis	43
3.1	Test fixture for elastomer characterization and heating	45
3.2	Proposed test fixture for variable frequency elastomer characterization	46
3.3	Magnetic fixture for induction heating test, shown in parallel magnet configuration .	48
3.4	Lab test equipment interconnectivity	49
3.5	Control and measurement VI front panel	50
3.6	Available settings on VI Setup page	52
3.7	Dual thermistor conditioning circuit layout	55
3.8	Relative temperature calculation from thermistor data	56
3.9	Test setup for elastomer characterization	57
3.10	Sample data frequency spectra and coherence	58
3.11	Illustration of parameter identification from transfer function Bode plot (not to scale)	59
3.12	Thermal insulation and temperature measurement of VTE test article	60
3.13	Test setup for magnetic induction heating	61
3.14	Thermoelectric generators used for characterization tests	62
3.15	Test setup for TEG characterization	62
4.1	Commanded base excitation input voltage profiles	64
4.2	Measured RMS acceleration response of electrodynamic shaker base (over 500–1500 Hz) with test article installed	65
4.3	Measured elastomer natural frequency vs. input amplitude	66
4.4	Measured elastomer loss factor vs. input amplitude	67
4.5	Predicted transient temperature response for notional simulation cases	71

4.6	Predicted transient temperature response for notional simulation Case B with reduced insulation thickness	71
4.7	Predicted transient temperature response for actual VTE test article	74
4.8	Magnetic flux density plot for permanent magnet fixture from finite element magnetics analysis	77
4.9	Magnetic flux density along length within air gap of permanent magnet fixture . . .	78
4.10	Simulated steady-state temperature increase due to induction heating of aluminum plates	79
4.11	Measured VTE test article temperature response to base excitation	80
4.12	Al coupon temperature increase vs. peak base velocity for different coupon thicknesses	83
4.13	Voltage and power response of TEG to increasing surface temperature differential . .	85

List of Tables

3.1	Elastomer test article properties	46
3.2	PCB accelerometer calibration data	54
4.1	Measured and specified elastomer material properties	68
4.2	Elastomer properties for initial conceptual test cases	69
4.3	Predicted oscillator properties and response for notional cases	69
4.4	Component material thermal properties	70
4.5	Elastomer test article thermal circuit parameters, notional cases	70
4.6	Elastomer dimensions for experimental VTE test article	72
4.7	Predicted test article response for VTE test article	72
4.8	Elastomer thermal circuit parameters for VTE test article	72
4.9	Induction heating test parameters	82

List of Symbols

A	Oscillator displacement amplitude, m
a	Area, m ²
B	Magnetic flux density, T
C_T	Thermal capacitance, J/°C
c_p	Specific heat capacity, J/kg-°C
E	Electric field, V/m
F	Force, N
G	Shear modulus, Pa
h_0	Convective heat transfer coefficient, W/m ² -°C
I	Current, A
J	Current density, A/m ²
k	Elastic stiffness, N/m
L	Length, m
M	Transmissibility
m	Mass, kg
P	Power, W
Q	Heat, J
\dot{Q}	Rate of heat generation or dissipation, W
q	Electric charge, C

\dot{q}	Heat flux, W/m ²
R	Resistance, Ω
R_T	Thermal resistance, °C/W
S	Base displacement amplitude, m
T	Temperature, °C
V	Voltage, V
v	Velocity, m/s
W	Work, J
x	Position, m
y	Position, m
Γ	Volume, m ³
ζ	Damping ratio
η	Loss factor
κ	Thermal conductivity, W/m-°C
ρ	Electrical resistivity, Ω-m
ρ_m	Mass density, kg/m ³
σ	Electrical conductivity, (Ω-m) ⁻¹
ω	Angular frequency, rad/s

Acknowledgments

I would like to thank my advisors, Professors Smith and Lesieurte, for their guidance, support, and patience. This project and resulting thesis would not have been possible without their mentorship and sage advice. Funding for this project was provided by a research fellowship sponsored by LORD Corporation through the Penn State Vertical Lift Research Center of Excellence (VLRCOE). A very special thanks to Dr. Mark Jolly, Dr. Lane Miller, Haris Halilovic, Jeff Allred, Matt Smith, Andrew Deering, and Mark Downing for their creative input, technical guidance, and assistance with obtaining necessary test hardware. I would also like to thank Mike Wozniak, Justin Long, Rick Auhl, and JD Miller for providing valuable assistance with laboratory equipment.

Chapter 1

Introduction

THE harvesting of ambient energy to generate usable power has continued to gain popularity over the last several years as evidenced by the increasing prevalence of wind turbines and solar panels in our communities. Power sources that exploit thermal or solar energy are commonly integrated into personal electronics such as calculators, watches, and cell phone backup batteries.

Whereas photovoltaic cells have provided power to satellites since the early days of the space program, the adaptation of other energy harvesting technologies to sensing applications on aerospace platforms has only gained interest in recent years. In particular, increasing research into structural health monitoring (SHM) and condition-based maintenance (CBM) of aerospace structures has prompted the need for energy harvesting methods to power the associated sensors and electronics without the need for cables or batteries.

Various sources of unused energy are present on a helicopter: mechanical energy manifests as vibration of the structure or as acoustic noise, thermal energy is dissipated by electrical systems or friction in moving components, and electromagnetic radiation is released from the power and communication systems. Every effort is made during the design process to reduce the sources of wasted energy, but it can be challenging to eliminate them completely. Energy harvesting devices would be strategically placed at locations throughout the aircraft to collect energy that would otherwise be wasted and convert it into usable electrical power.

The conversion of mechanical energy originating from periodic structural vibrations is of particular interest to energy harvesting on helicopters. Vibrations originating in the drive system can result from elastic deformations or physical imperfections of the gear teeth in the main rotor transmission. These vibrations occur at the gear meshing frequency, typically around 500–3000 Hz [1, 2].

A new method for harvesting mechanical energy from periodic structural vibrations is described in this study for possible application to health monitoring on rotorcraft drive systems. This chapter presents an overview of materials and concepts relevant to vibration energy harvesting, describes research applicable to the present study, and identifies some devices that are available for vibration energy harvesting.

1.1 Electromagnetic harvesters

A typical electromagnetic generator consists of a permanent magnet moving relative to a stationary coil [3]. When vibration energy is to be harvested by the generator, the motion of the permanent magnets relative to the coil can be achieved by integrating the magnets into a mass-spring oscillator, as illustrated in Figure 1.1; the motion of the magnets is amplified due to resonance and results in power induced in the coil. A practical realization of this concept is illustrated in Figure 1.2, wherein the magnets are integrated onto a tuned beam installed on a vibrating base.

1.1.1 Electromagnetic power generation

Power generation from electromagnetic induction is governed by Faraday’s law, which states that the voltage V induced in a circuit is proportional to the rate of change of magnetic flux ϕ through the circuit. A simple manifestation of an electromagnetic generator is a wire loop moving relative to a stationary magnetic field, wherein a voltage will be induced through the loop in the direction opposite the rate of change of the magnetic flux [6]. For a circuit with N loops, the total flux linkage through the circuit will be $N\phi$, which allows Faraday’s law to be written as Eq. (1.1).

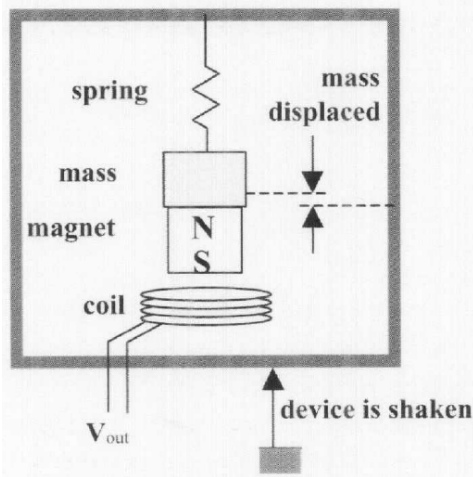


Figure 1.1: Simple electromagnetic power generator [4]

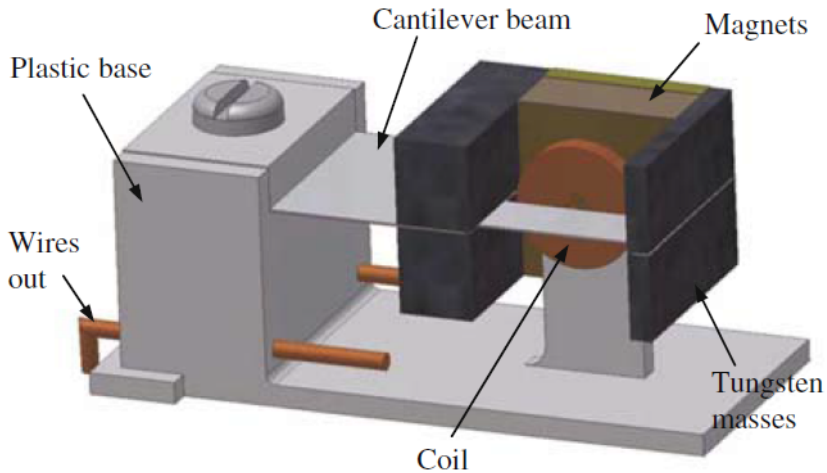


Figure 1.2: Cantilever magnet generator [5]

$$V = -N \frac{d\phi}{dt} \quad (1.1)$$

For a system where the motion of the wire loop (or of the magnetic field) is restricted to a single direction y , Faraday's law can be rewritten in terms of the flux gradient $d\phi/dy$ and linear velocity $\dot{y} = dy / dt$.

$$V = -N \frac{d\phi}{dy} \dot{y} \quad (1.2)$$

For a circuit with total resistance R , the power P is given by Joule's law, which states that $P = V^2/R$. The power can also be expressed as the product of the velocity \dot{y} and a damping force F_d .

$$P = \frac{V^2}{R} = \frac{1}{R} \left(N \frac{d\phi}{dy} \right)^2 \dot{y}^2 = F_d \dot{y} \quad (1.3)$$

In general, as evidenced by Eq. (1.3), increasing the flux linkage gradient and minimizing the impedance through the generator circuit maximizes the power output [5]. For vibration energy harvesting at a particular frequency, a spring is integrated into the device allowing the coil or permanent magnets to oscillate relative to the other, and the oscillator mass and spring stiffness are selected such that the device resonates at the desired excitation frequency.

1.1.2 Electromagnetic vibration energy harvesters

Particularly for aerospace applications, minimizing the size and weight of any installed device is an important design consideration. A review of existing electromagnetic energy harvesting devices in [5] found that the devices designed to operate at higher frequencies produce a much lower power output per unit volume, and that scaling these devices down to a smaller scale is not feasible for many applications. However, they also noted that electromagnetic harvesters can have better performance properties, endurance, and frequency bandwidth than piezoelectric devices for applications where size or weight is not a constraint. The normalized output power density, which is the power generated per unit volume per unit base acceleration, for various devices is plotted against the operating frequency in Figure 1.3.

Much of the research effort into electromagnetic vibration energy harvesting has been focused around microelectronic devices [5, 7]. A field test of a prototype electromagnetic harvester described in [7] for health monitoring of automotive transmissions (around 3 kHz) resulted in an average power

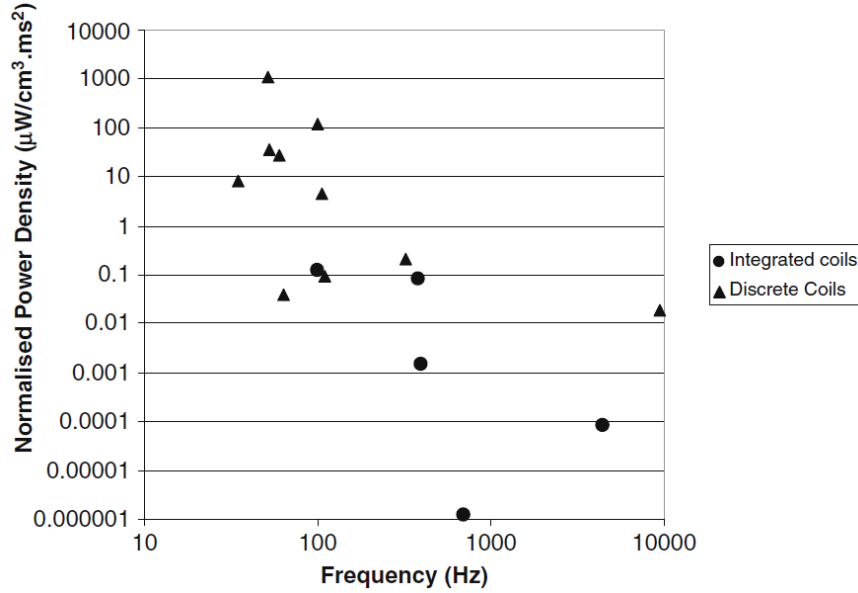


Figure 1.3: Electromagnetic harvester power output vs. operating frequency [5]

output of 0.157 μW . Other electromagnetic harvesters designed to operate at high frequencies (500–5000 Hz) have resulted in power output on the order of tens of micro-watts [5, 4].

Lower frequency (10–100 Hz) electromagnetic harvesters are generally capable of producing a power output on the order of hundreds of micro-watts, or higher. For example, the MVEH device pictured in Figure 1.4 can be tuned to 15–60 Hz and can generate up to 4 mW of power at 3.2 VDC at 0.2 g's [8]. The use of electromagnetic devices for vibration energy harvesting has also been studied for application to load sensing on rotorcraft pitch link rod ends [9, 10]. The target power output for this application was 1 mW at an operating frequency of about 4 Hz.

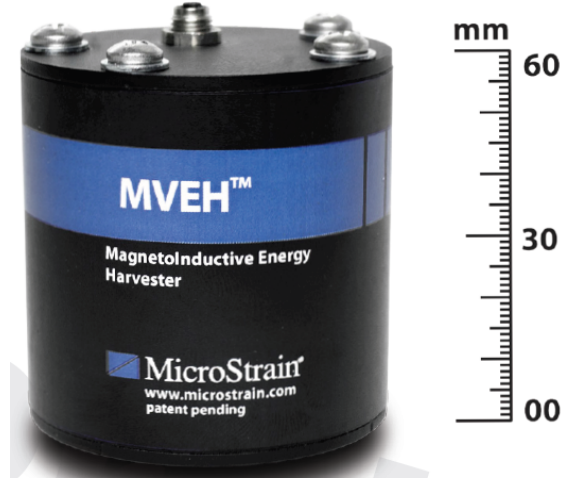


Figure 1.4: LORD-MicroStrain Magnetoinductive Vibration Energy Harvester (MVEH) [8]

1.2 Piezoelectric harvesters

Piezoelectric materials exhibit coupling of their mechanical and electrical behavior, thus making them very useful for sensing, energy harvesting, and actuation. When operated as a sensor or harvester, a proportional voltage output is generated via the direct piezoelectric effect when the material is subject to a mechanical strain. The inverse effect, whereby the material undergoes a mechanical deformation in response to an applied voltage, is observed when the piezoelectric material is operated as an actuator [11, 12].

The 1 and 2 axes of a piezoelectric sheet are defined to be in the plane of the sheet, with the 3 axis normal to the surface of the sheet in the poling direction. Two operating modes are commonly employed for piezoelectric harvesting: in the 31 mode, stress is applied axially while the voltage is measured perpendicular to the sheet; in the 33 mode, the applied stress and measured voltage are both in the perpendicular direction. The material axes definitions and operating modes are illustrated in Figure 1.5. The poling direction is defined the axis along which the material is permanently polarized, or the direction of charge flow through the piezoelectric sheet.

A common method for piezoelectric energy harvesting is to incorporate a piezoelectric sheet or stack into a cantilever beam design with a proof mass on the free end for tuning, as illustrated in Figure 1.6. Considerations for development of an electromechanical model to describe the dynamics

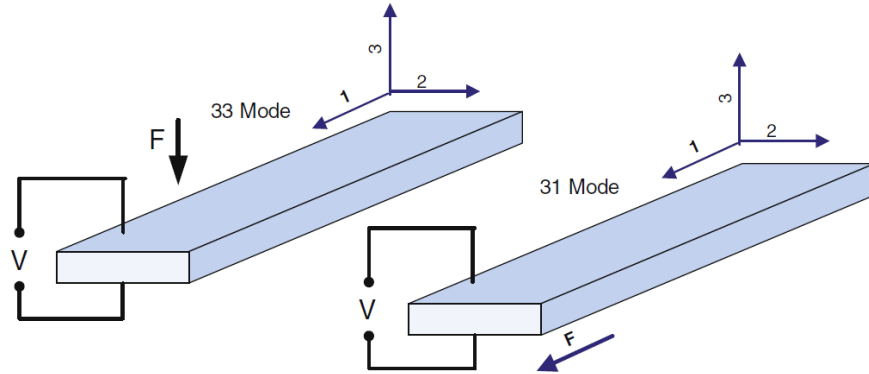


Figure 1.5: Material axis definitions for a thin piezoelectric sheet [5]

of the integrated cantilever piezoelectric structure are described in [13]. For harvesting applications where it is necessary to power a sensor or other device, the output from the piezoelectric element is AC voltage that must be converted to DC by means of a voltage rectifier [5, 14].

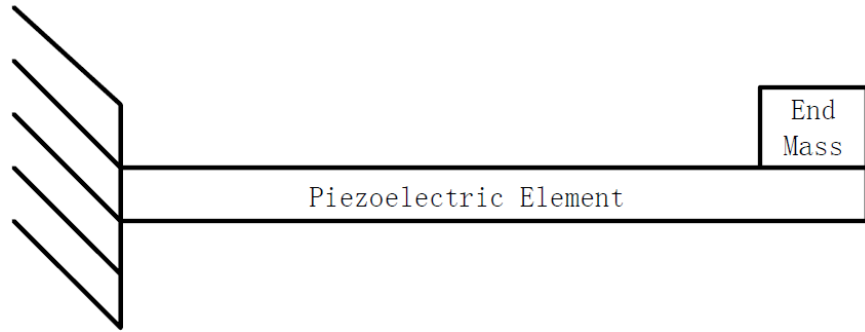


Figure 1.6: Piezoelectric material integrated into cantilever beam with tip mass [14]

1.2.1 The piezoelectric effect

For small displacements, the mechanical strain tensor S can be approximated in terms of the spatial gradient of the displacement field u with respect to axis x .

$$S_{ij} = \frac{1}{2} \left(\frac{\partial u_i}{\partial x_j} + \frac{\partial u_j}{\partial x_i} \right) \quad (1.4)$$

The electric displacement D in a linear medium [6] can be defined in terms of the electric field E and polarization P , where ϵ_0 is the permittivity of free space.

$$D_i = \epsilon_0 E_i + P_i \quad (1.5)$$

From conservation of energy and consideration of the boundary conditions of the system, the fundamental behavior described by Eq. (1.4) and Eq. (1.5) can be used to derive the constitutive equations for a linear piezoelectric material [11]. The form shown in Eq. (1.6) states that a stress T_1 applied along axis 1 will result in strain S_1 also along axis 1, with an electric displacement D_3 along axis 3. Conversely, application of an electric field E_3 will result in electric displacement along the same axis as well as mechanical strain along axis 1.

$$\begin{Bmatrix} S_1 \\ D_3 \end{Bmatrix} = \begin{pmatrix} s_{11}^E & d_{31} \\ d'_{31} & \epsilon_{33}^T \end{pmatrix} \begin{Bmatrix} T_1 \\ E_3 \end{Bmatrix} \quad (1.6)$$

The transformation matrix in Eq. (1.6) contains information about the material properties of the piezoelectric material: s_{ij}^E is the compliance tensor (strain per unit stress) under a constant electric field; d_{ij} is a tensor containing the piezoelectric charge coefficients, which describe the relationship between electric charge and mechanical stress; and ϵ_{ij}^T is the permittivity (electric displacement per unit electric field) under constant stress.

Inverting Eq. (1.6) gives an alternative form for the constitutive equation, describing the response of the material to polarization along axis 3 and strain applied along axis 1.

$$\begin{Bmatrix} T_1 \\ E_3 \end{Bmatrix} = \frac{1}{1 - k_{31}^2} \begin{pmatrix} 1/s_{11}^E & -k_{31}^2/d_{31} \\ -k_{31}^2/d_{31} & 1/\epsilon_{33}^T \end{pmatrix} \begin{Bmatrix} S_1 \\ D_3 \end{Bmatrix} \quad (1.7)$$

The coupling factor k_{31} in Eq. (1.7) provides a measure of the effectiveness of energy transduction in a piezoelectric material and is defined in Eq. (1.8).

$$k_{31}^2 = \frac{d_{31}^2}{\epsilon_{33}^T s_{11}^E} \quad (1.8)$$

1.2.2 Piezoelectric vibration energy harvesters

In most cases, it is beneficial to select a material with a high coupling factor for an application employing piezoelectric materials. One of the most readily available and commonly used piezoelectric material is lead zirconate titanate (PZT), which typically has a coupling coefficient of 0.3–0.7 [15, 16].

Piezoelectric energy harvesters are well-suited for use in high frequency harvesting applications such as on rotorcraft. One commercially available piezoelectric energy harvester device is the LORD-MicroStrain PVEH, pictured in Figure 1.7, which is capable of generating 30 mW of power at 3.2 VDC when operated at 1 kHz at up to 1.5 g's [8]. Another small piezoelectric harvester produced by KCF Technologies for rotorcraft structural health monitoring was able to generate over 1 mW when excited at 700 Hz at a base vibration level of 0.1 g's [17]. A microelectronic harvester described in [5] was constructed using multiple cantilever beams to achieve a wider frequency bandwidth, and it was able to output about 0.1 μ W when operated at 870 Hz.

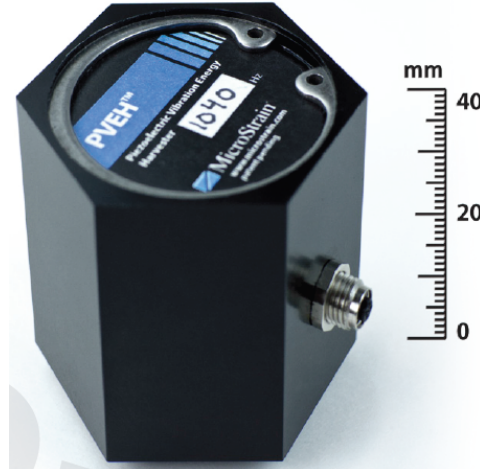


Figure 1.7: LORD-MicroStrain Piezoelectric Vibration Energy Harvester (PVEH) [8]

A recent study by [16] demonstrated that single crystal piezoelectric materials such as PMN-PT show promise for future energy harvesting applications due to higher energy density and reliability. The single crystal device shown in Figure 1.8 was able to produce about 3 mW of power when installed on a structure vibrating at 1 g around 700 Hz. However, research into the field of single crystal materials is relatively recent and additional characterization of the behavior of single crystal materials is required before they can be adopted for commercial use.

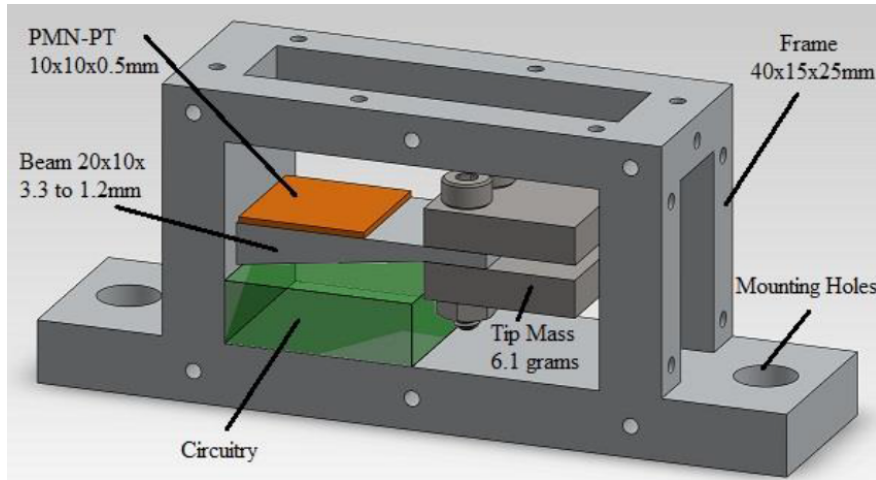


Figure 1.8: Cantilever beam piezoelectric vibration energy harvester using single crystal material [16]

1.2.3 Multi-modal and composite devices

A multi-modal energy harvesting device simultaneously harvests energy from multiple sources or implements multiple mechanisms for energy harvesting. Many such devices have been described in recent research as a means to increase the power output of energy harvesters. In particular, the combination of piezoelectricity with other mechanisms for power generation such as electromagnetism is of particular interest to vibration energy harvesting. One such device is illustrated in Figure 1.9.

Magnetostrictive materials exhibit mechanical strain as a result of an applied magnetic field. The strain is due to rotation of magnetic domains within the material that align with the direction of the applied field [18]. Magnetolectric composites contain both magnetostrictive and piezoelectric

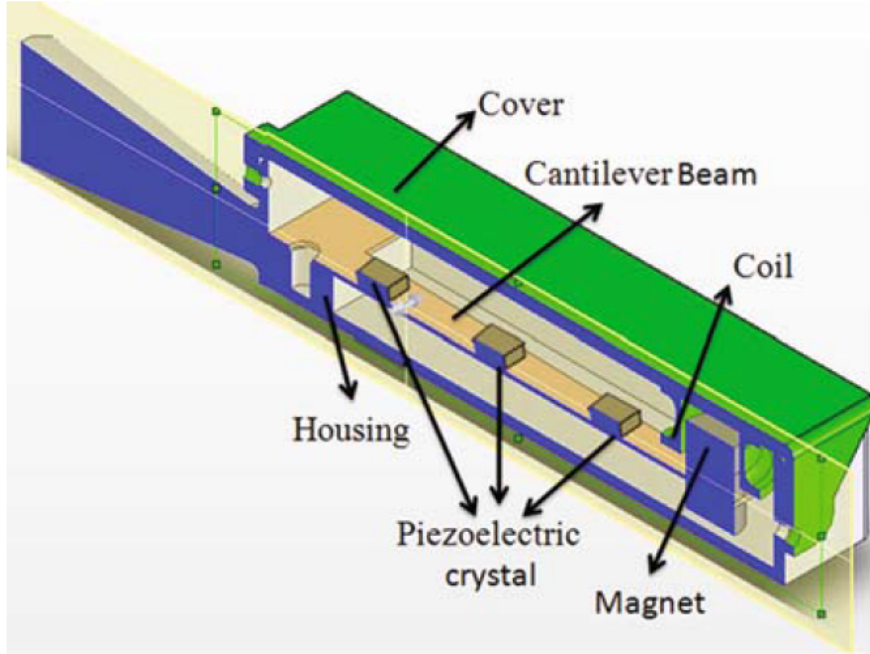


Figure 1.9: Integrated piezoelectric and electromagnetic vibration energy harvester [5]

layers, and they can be used to create vibration energy harvesters with higher power density than their piezoelectric counterparts [5].

Other harvester designs implement more creative means of generating strain within a piezoelectric sheet. In the configuration shown in Figure 1.10, a steel ball moves freely between two piezoelectric sheets and strikes the sheets as the device vibrates, deforming the piezoelectric sheets to generate power [4]. A harvester design developed in [13] and reproduced in Figure 1.11 uses chaotic motions from interaction by a ferromagnetic beam with a pair of permanent magnets to deform the piezoelectric layers. Both of these devices were designed to be implemented in low-frequency harvesting applications (< 10 Hz).

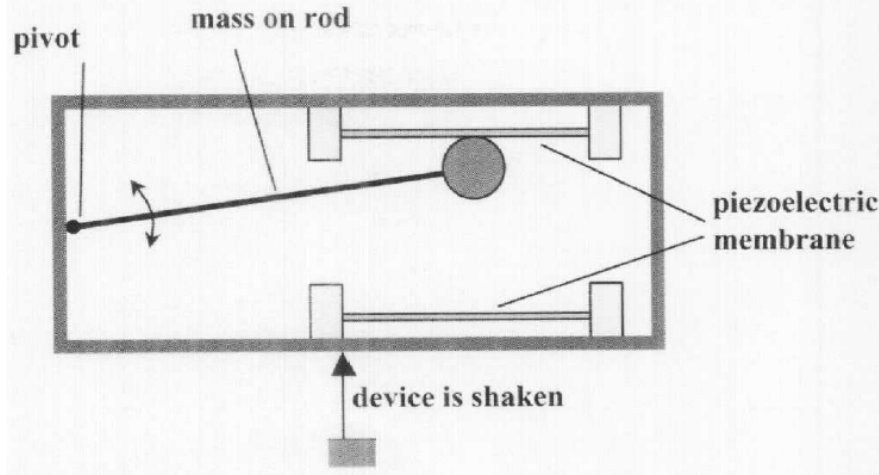


Figure 1.10: Non-linear piezoelectric vibration energy harvester) [4]

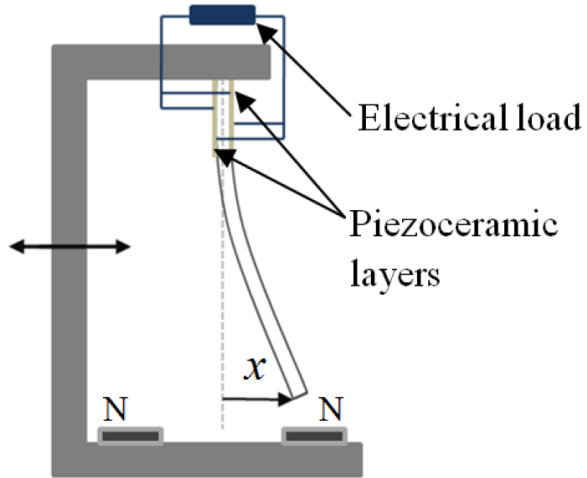


Figure 1.11: Piezo-magneto-elastic harvester design [13]

1.3 Heat generation and harvesting

This section introduces viscoelastic materials and electromagnetic induction in the context of heat generation from mechanical vibrations, which is relevant to the analyses presented in this thesis. A damped oscillator will dissipate heat when excited at resonance. The heat lost manifests as a temperature increase of the damper element of the oscillator. The thermoelectric generator (TEG) is also introduced in this section as a means of converting thermal energy into electrical energy for harvesting applications.

1.3.1 Viscoelastic materials

Viscoelastic materials, or elastomers, exhibit properties of both elastic and viscous materials. As a result, an elastomer can usually act as both a spring and a damper in a mechanical oscillator. In general, when an elastomer is loaded cyclically, it will heat up until an equilibrium temperature distribution is reached. This heating effect can be described in terms of the stress-strain hysteresis. When the stress σ applied to an elastomer is plotted against the resulting strain ϵ over one load cycle, as shown in Figure 1.12a, the enclosed area D is the heat dissipated per cycle by the elastomer [19, 20].

As the heat input increases due to increasing strain amplitude, changes in ambient temperature, or other factors, the heat dissipated to the environment may become less than the self-heating generated by the hysteresis effect. This can result in a thermal runaway condition where the elastomer temperature continues to increase until a failure occurs [21]. Thermal equilibrium and runaway conditions are depicted in Figure 1.12a.

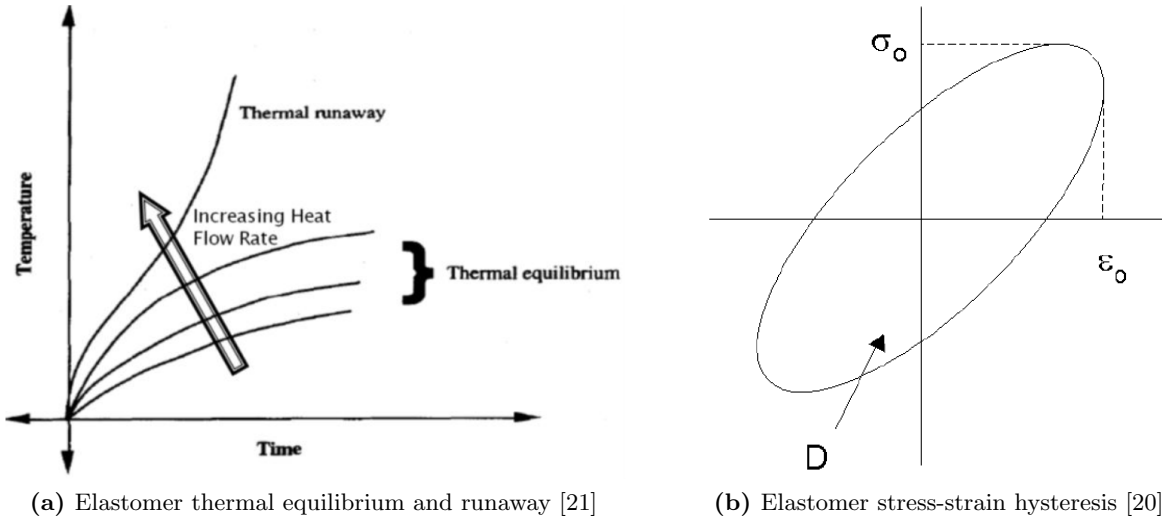


Figure 1.12: Dynamic heating of cyclically loaded elastomer

Methods for modeling the self-heating of elastomers has been studied at length [22, 23], and in particular for application to elastomeric dampers on rotorcraft [24]. Harvesting thermal energy

from main rotor lead-lag dampers that dissipate heat during normal operation may be an area of interest for application to damage detection and health monitoring on the rotor hub.

1.3.1.1 Dynamic material properties

For small deformations, the dynamic behavior of an elastomer can be approximated as linear. The complex modulus of elasticity G^* of a viscoelastic material subjected to harmonic forcing can be represented as a single complex quantity whose real part is the storage modulus G' , which describes the stiffness of the material, and whose imaginary part is the loss modulus G'' , which describes the damping properties of the material.

$$G^* = G' + iG'' \quad (1.9)$$

The loss factor η is defined as the ratio of the loss modulus to the storage modulus, and it provides a measure of the energy dissipated by the material during elastic deformation.

$$\eta = \frac{G''}{G'} \quad (1.10)$$

The complex stiffness k^* of an oscillator using a viscoelastic material is directly proportional to the modulus, and the constant of proportionality depends on the geometry of the component. For example, an elastomer sheet with cross-sectional area a and thickness L loaded in shear along its cross section has stiffness given by Eq. (1.11).

$$k^* = \frac{a}{L} G^* \quad (1.11)$$

The stiffness can therefore also be expressed as the sum of real and complex parts. From Eq. (1.10), loss factor η can also be expressed as the ratio of the complex part to the real part of the stiffness. Definition of the dynamic properties of a particular elastomer requires specification of the elastic modulus G' , from which the elastic stiffness k' can be calculated, and the loss factor

η . These properties are generally provided by the material manufacturer for some range of nominal operating conditions.

$$k^* = k' + ik'' = k'(1 - i\eta) \quad (1.12)$$

Also note that, for low damping, η is related to the modal damping ratio ζ by a factor of 2 [21, 25].

$$\zeta = \eta/2 \quad (1.13)$$

Nonlinear behavior of the elastomer under cyclic deformations can be modeled by assuming that the material is thermorheologically simple, or that the amplitude dependence of the modulus G (1.14) is separable from the frequency and temperature dependence [26]. The amplitude response function g and frequency-temperature response function h are determined by curve fitting experimental data. The loss factor η (1.15) is also modeled as separable into an amplitude response g_η and frequency-temperature response h_η , both of which are also determined empirically. The separated functions g and h are normalized at some reference point, G^0 and η^0 , for the modulus and loss factor functions, respectively.

$$G'(x, \omega, T) = G_s^0 g'(x) h'(\omega, T) \quad (1.14)$$

$$\eta(x, \omega, T) = \eta^0 g_\eta(x) h_\eta(\omega, T) \quad (1.15)$$

1.3.1.2 Nonlinearity with frequency and temperature

The behavior of elastomers under harmonic loading with varying frequency, strain amplitude, and temperature has been studied in the past for lower-frequency applications such as rotorcraft bearings and dampers [27, 28]. The storage modulus, loss modulus, and loss factor vary nonlinearly with increasing temperature or frequency as illustrated in Figure 1.13.

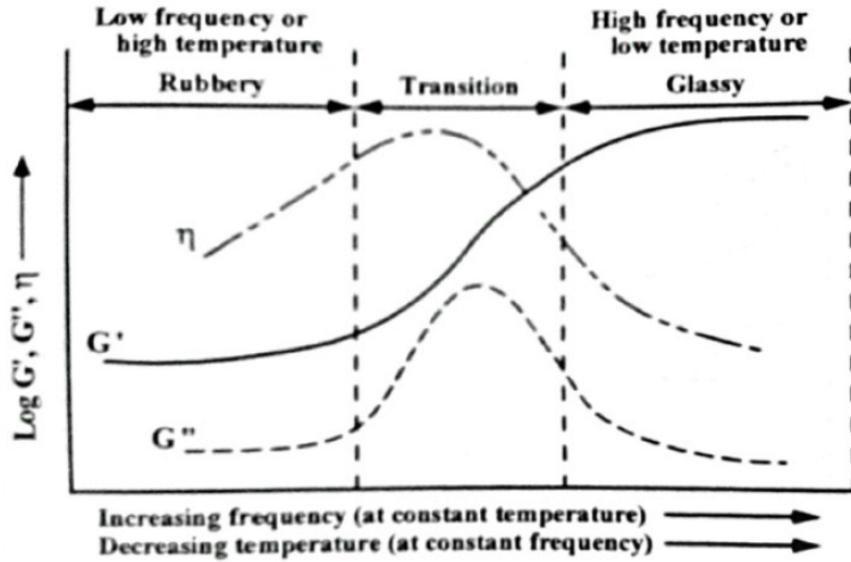


Figure 1.13: Variation in elastomer properties with temperature [27]

Behavior of elastomers during high-frequency operation has been studied for application to the design of elastomeric mounts for gearbox isolation. Elastomer material properties can be affected by amplitude, temperature, preload, and frequency [29].

The dependence of the shear modulus on frequency and temperature for a representative high-damping silicon elastomer manufactured by LORD Corporation is shown in Figure 1.14. The data show that the material becomes stiffer as the frequency is increased or the temperature is decreased, which is a typical result for elastomers [26]. Methods for nonlinear modeling of elastomer properties with frequency and temperature are discussed in [28], but many such models tend to become inaccurate at high frequencies or low temperatures.

1.3.2 Eddy currents and induction

If a conducting metal is exposed to a time-varying magnetic field, then free charges within the conductor will be forced to move resulting in induced eddy currents in the conductor. [3, 6]. The resistance to these currents within the material results in heat generation and dissipation.

Much of the research on eddy current damping is focused on magnetic braking and vibration suppression [30]. Several models for the braking force due to eddy currents for several brake

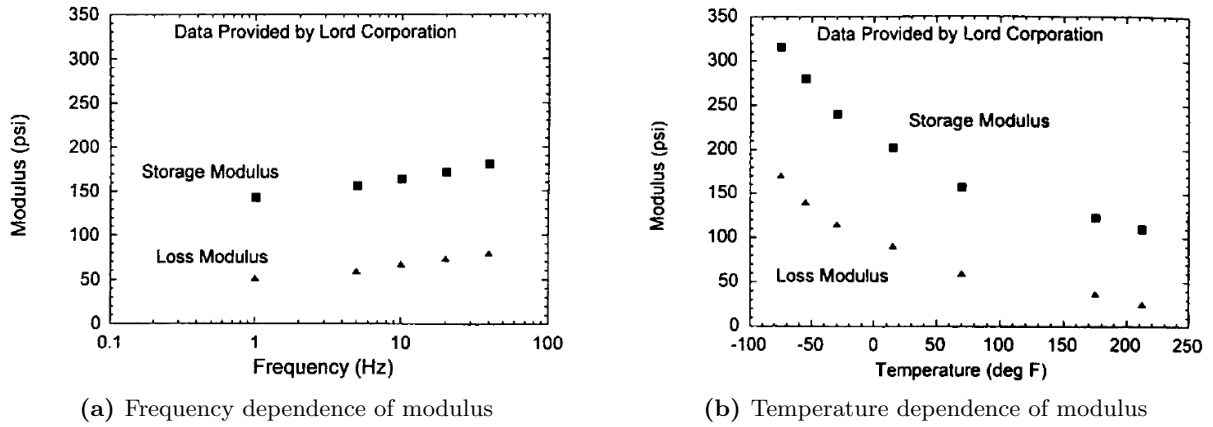


Figure 1.14: Non-linearity in complex modulus of an elastomer [28]

configurations have been developed and validated by experiment [31, 32, 33]. Other studies have provided models for the dynamic behavior of oscillators or beams subjected to electromagnetic forces [34, 35].

1.3.2.1 Material electrical properties

The electrical resistivity ρ of a material describes its resistance to current, which is the flow of electric charge. A material with low resistivity (such as copper) is an electrical conductor, whereas a material with high resistivity (such as rubber) is an insulator. Electrical conductivity σ is defined as the inverse of resistivity ($\sigma = 1/\rho$).

The electrical resistance R of a piece of material with cross-sectional area a (perpendicular to the flow of charge) and length L (in the direction of charge flow) is proportional to its resistivity ρ .

$$R = \frac{\rho L}{a} \quad (1.16)$$

Suppose a potential difference V is applied across the length of a conductor with resistance R . The resulting current I flowing through the conductor is described by Ohm's law (1.17).

$$I = \frac{V}{R} \quad (1.17)$$

Resistance of a conductor to current flow results in energy dissipated as heat. This phenomenon is called Joule heating, and the dissipated power P is given by the Joule heating law (1.18).

$$P = I^2 R = \frac{V^2}{R} \quad (1.18)$$

The Joule heating phenomenon can be described as the result of a force acting on each charge in the direction opposite the flow of charge. The force \mathbf{F} on an individual electric charge q moving with velocity \mathbf{v} within an electric field \mathbf{E} and/or magnetic field \mathbf{B} is given by the Lorentz force law (1.19) [6].

$$\mathbf{F} = q(\mathbf{E} + \mathbf{v} \times \mathbf{B}) \quad (1.19)$$

1.3.2.2 Induction heating

The generation of heat by induction has been studied and used for many years for industrial applications such as forming and treating metals [36]. Induction heating has also been used in other applications such as induction stoves [37].

Eddy currents induced within a conductor in proximity to a varying magnetic field are most prevalent close to the surface. The skin depth δ of the conductor is the depth at which most (86%) of the heating occurs. From Eq. (1.16) it is evident that the skin effect results in increased Joule heating since the effective resistance through which the current is flowing is increased. As shown by Eq. (1.20), the skin depth decreases with increasing frequency ω of the applied field [38, 39].

$$\delta = \sqrt{\frac{2\rho}{\mu\omega}} \quad (1.20)$$

When a varying magnetic field is applied to a ferromagnetic material such as iron or steel, additional heat is generated due to magnetic hysteresis. As the field is varied, magnetic dipoles within the material oscillate as they attempt to align with the field. Resistance to this dipole oscillation in the material results in a small but measurable amount of heat dissipation relative to

eddy current losses [38]. As a result, iron and steel are generally better suited to induction heating applications than copper or aluminum.

1.3.3 Thermal energy harvesting

Harvesting energy from heat sources has gained increasing popularity for biomedical applications, where developers are interested in powering devices from body heat [40]. Other applications include powering sensors for structural health monitoring on bridges or buildings, automotive engine health monitoring, and battlefield surveillance or reconnaissance [5].

A thermoelectric generator (TEG) generates electrical power when sandwiched between two surfaces of different temperatures, as illustrated in Figure 1.15.

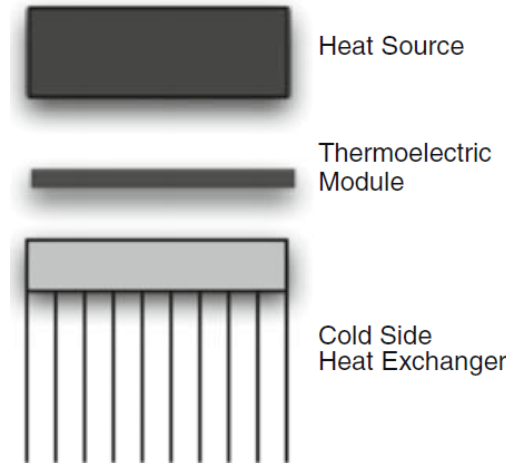


Figure 1.15: Thermoelectric generator implementation [5]

1.3.3.1 Thermoelectric generator operation

A thermoelectric generator (TEG) consists of p-type and n-type semiconductor materials connected electrically in series and thermally in parallel, as illustrated in Figure 1.16. The mechanism by which a difference in surface temperatures produces a voltage output from a thermoelectric material placed between the two surfaces is known as the Seebeck effect.

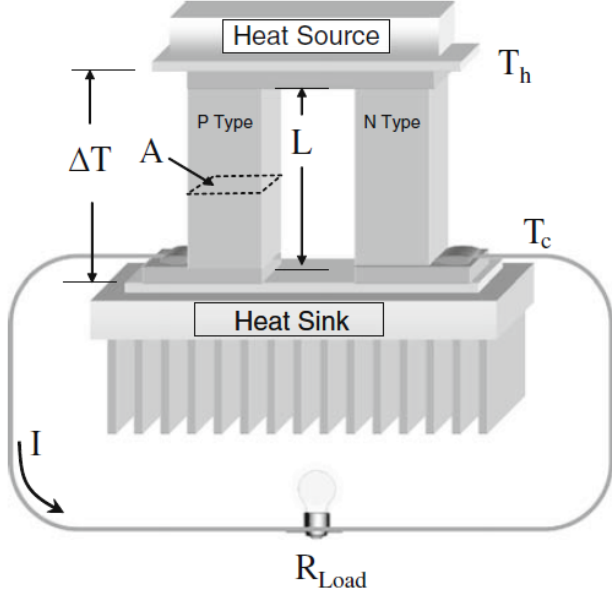


Figure 1.16: Thermoelectric generator architecture [5]

The voltage V is directly proportional to the temperature difference ΔT between the source and sink, and the proportionality constant α is defined as the Seebeck coefficient. The power P generated is specified by the device manufacturer at an optimal load resistance R_{Load} . In general, the efficiency of a thermoelectric generator increases linearly with temperature difference and is maximized by matching the internal resistance to the load resistance [5].

$$V = \alpha \Delta T \quad (1.21)$$

1.4 Objectives

In this thesis, a multi-modal method for harvesting vibration energy is proposed for application to vibrating aerospace structures. Vibration of a damped mechanical oscillator is used to generate heat, and the generated heat is converted to electrical energy which can be used to power sensors or other electronics. Mechanisms for the flow and conversion of energy are summarized in Figure 1.17.



Figure 1.17: Energy flow for conceptual vibration energy harvester

The vibration energy harvesting concept is implemented in two separate ways for this study, dubbed *magneto-thermoelectric* (MTE) and *visco-thermoelectric* (VTE). The VTE method features an oscillator whose stiffness and damping properties are provided by a viscoelastic material that is subject to harmonic loading at resonance. Energy dissipated by the elastomer is used to heat a metal element that serves as the heat source for the TEG. The MTE method features a conducting metal plate oscillating relative to a magnetic field generated by permanent magnets. Joule heating due to the induced eddy currents in the metal plate generates heat for thermoelectric conversion by the TEG.

1.4.1 Approach

A detailed description of the proposed harvesting method is provided in Chapter 2, and one-dimensional engineering analysis models are developed for both the MTE and VTE realizations of the method. The resulting analytical models are used to predict the behavior of test articles constructed for validation of the engineering models.

The equipment and methods used for experimental concept validation testing are described in Chapter 3. A description of software developed for hardware control, measurement, and data analysis is also provided. Associated test hardware and methods used for analysis are introduced.

The predictions generated from the engineering models as well as the results of laboratory testing are provided in Chapter 4. The responses of the test articles are compared to the model predictions.

Possible sources of error in the analysis and experiment are discussed in Chapter 5. Finally, the feasibility of the proposed harvester concept based on the test results is addressed, along with recommendations for future work.

Chapter 2

Analysis Methods

The harvesting method considered in this study converts heat dissipated by a damped linear oscillator into electrical energy. A simple model for linear oscillator motion is first developed as a basis for the energy harvesting method. A review of relevant viscoelasticity and electromagnetism concepts is then presented since viscoelastic self-heating and magnetic induction heating are the methods used for dynamic heat generation. The heat equation and methods for analysis of heat flow are then introduced. Finally, conceptual test articles for validation of the analytical model are described.

2.1 Harvester description

The proposed harvester features a damped mechanical oscillator installed on a structure that vibrates at a particular frequency, which is the same as the natural frequency of the oscillator. Mechanical energy absorbed by the installed device is dissipated by the damping element of the oscillator as thermal energy, which is then conducted to a metal plate. Heat flow between the surface of the heated metal plate and an ambient-temperature heat sink is used to generate electrical power by use of a thermoelectric generator (TEG) placed between the two surfaces. This concept for energy harvesting is illustrated in Figure 2.1.

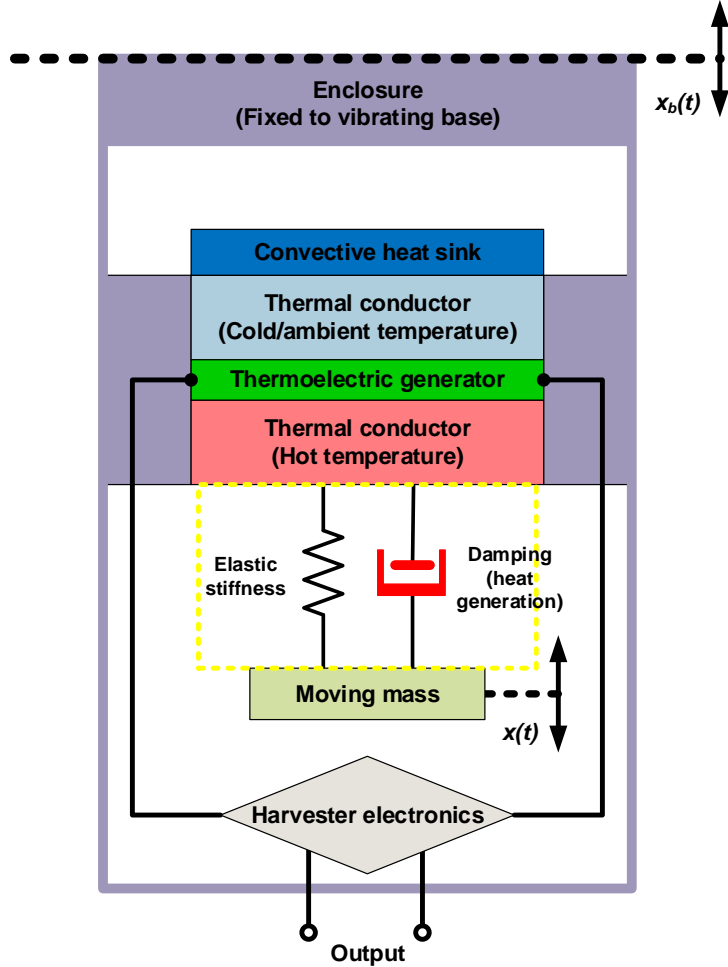


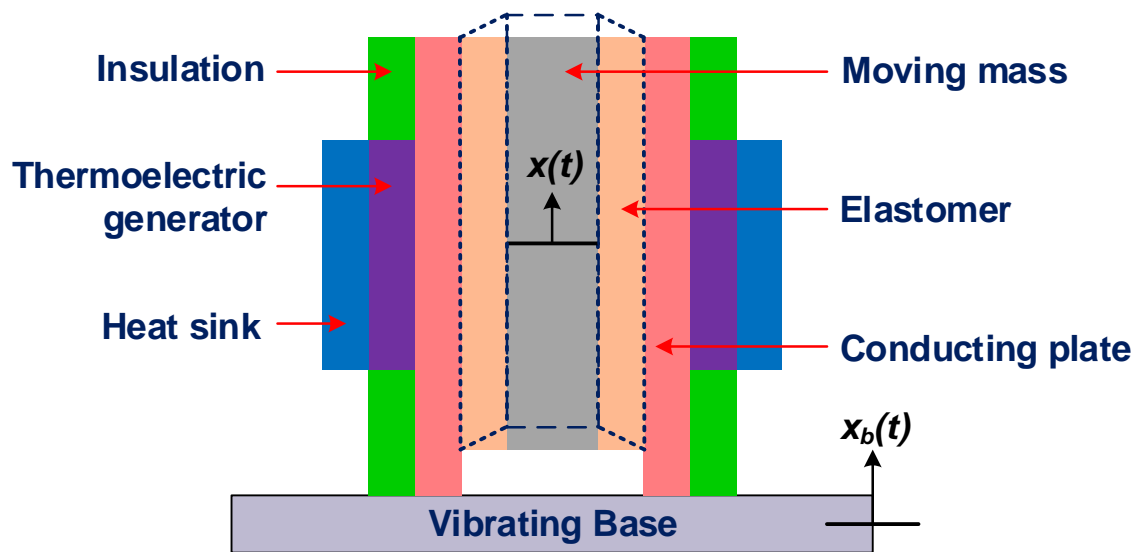
Figure 2.1: Vibration energy harvesting concept

A realization of the visco-thermoelectric (VTE) harvester is shown in Figure 2.2a. The conceptual device is symmetric with two heat-generating elastomer sheets operating in shear attached to either side of the moving mass. Conducting metal end plates heat up in response to heating of the elastomer sheets, and a TEG on each of the end plates generates electrical power. The mass of the central moving element and elastic properties of the elastomer are selected such that the natural frequency of the oscillator matches the desired operating frequency. The deformed shape of the elastomer and position of the moving mass at peak oscillator displacement are shown (exaggerated)

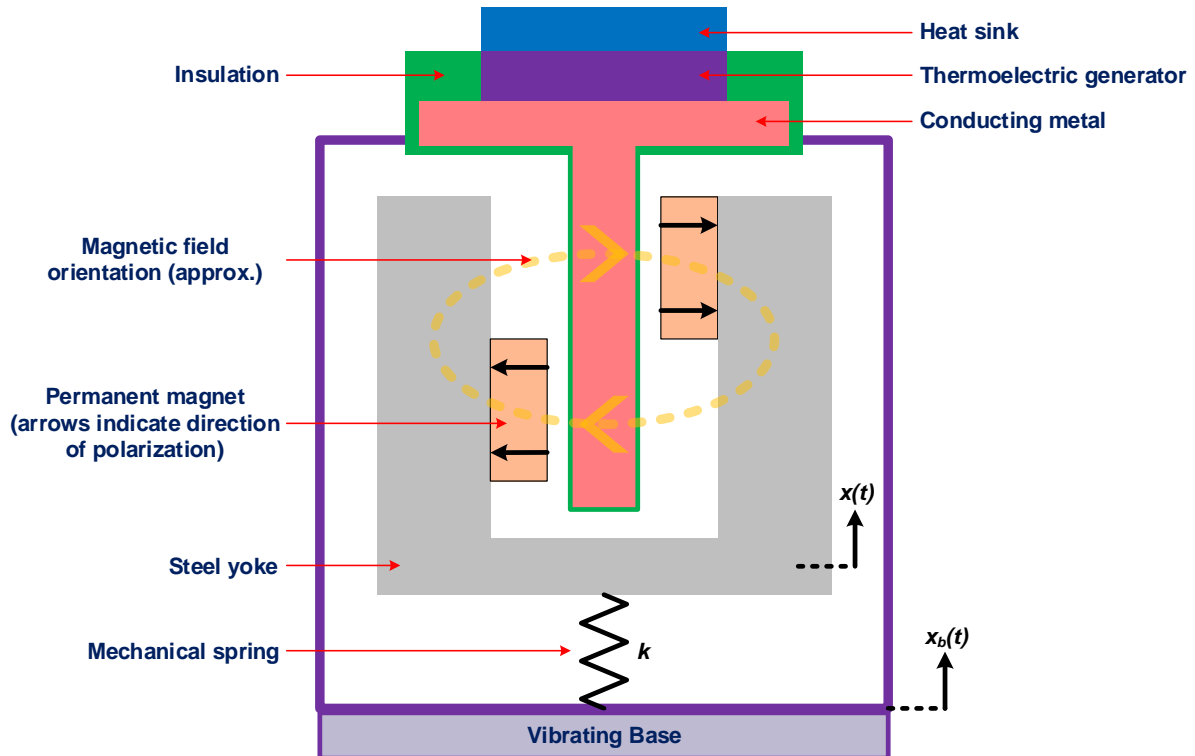
as dotted blue lines. This geometry was selected due to its simplicity and symmetry, and future realizations of the VTE harvester may use a different configuration.

A conceptual MTE harvester is illustrated in Figure 2.2b. In the configuration shown, permanent magnets on either side of a conducting metal plate generate a magnetic field through the plate. A steel yoke to which the magnets are fixed serves to direct the magnetic flux around the circuit while maximizing the field intensity to which the plate is exposed and minimizing flux leakage. The yoke and magnets constitute the moving mass for the oscillator and a spring provides the necessary mechanical compliance. The spring stiffness is selected such that the natural frequency of the oscillator matches the desired operating frequency. The relative motion of the magnets with respect to the plate results in generation of eddy currents in the plate, which damps the motion of the oscillator and heats up the plate. The heat is conducted outward from the plate through the TEG which consequently generates electrical energy.

Whereas the concept drawing for the MTE harvester indicates a single spring as the mechanical compliance element for the oscillator, multiple springs whose effective stiffness equals the desired stiffness could also used. Another conceivable configurations might use a tuned beam or elastomer to achieve the necessary stiffness.



(a) Symmetric realization of VTE harvester



(b) Alternating magnet realization of MTE harvester

Figure 2.2: Conceptual drawings of vibration energy harvesting devices (not to scale)

2.2 Forced linear motion

The vibration energy harvester is modeled as a damped linear single degree of freedom oscillator installed on a vibrating base, as illustrated in Figure 2.1. Assume that the displacement $x(t)$ of the moving mass and displacement $x_b(t)$ of the base are harmonic with angular frequency ω and complex amplitudes A and S , respectively.

$$x(t) = Ae^{i\omega t} \quad (2.1)$$

$$x_b(t) = Se^{i\omega t} \quad (2.2)$$

The equation of motion for this linear system describes the displacement of the moving mass in terms of the assumed harmonic displacements. In rewriting the equation of motion (2.3), the damping ratio is defined to be $\zeta = c/\sqrt{mk}$, and the undamped natural frequency of the oscillator is defined to be $\omega_n = \sqrt{k/m}$. The notation $\dot{x} = dx/dt$ is adopted for convenience.

$$\begin{aligned} m \frac{d^2x}{dt^2} + c \frac{d}{dt}(x - x_b) + k(x - x_b) &= 0 \\ \ddot{x} + 2\zeta\omega_n\dot{x} + \omega_n^2 x &= 2\zeta\omega_n\dot{x}_b + \omega_n^2 x_b \\ (-\omega^2 + 2i\zeta\omega_n\omega + \omega_n^2)Ae^{i\omega t} &= (2i\zeta\omega_n^2)Se^{i\omega t} \end{aligned} \quad (2.3)$$

The ratio of the output (amplitude of mass motion) to input (amplitude of base motion) is defined as the transmissibility M .

$$M(\omega) = \frac{A}{S} = \frac{2i\zeta\omega_n\omega + \omega_n^2}{-\omega^2 + 2i\zeta\omega_n\omega + \omega_n^2} \quad (2.4)$$

If the oscillator is excited at resonance, then the substitution $\omega = \omega_n$ into Eq. (2.4) can be used to obtain the transmissibility at resonance.

$$M(\omega_n) = \frac{1}{2i\zeta} \quad (2.5)$$

2.3 Heat generation

From the first law of thermodynamics, the work done by the damping force $F_d(t)$ per cycle to resist the motion of the oscillator is equal to the heat dissipated per cycle Q_{cyc} , assuming no other energy losses [3]. If the damping force $F_d(t)$ is known, the instantaneous power is the product of $F_d(t)$ and the relative velocity $v_{rel}(t) = \dot{x}(t) - \dot{x}_b(t)$ between the motion of the mass and the base. The energy dissipated by the dashpot element per cycle is the power integrated over a single cycle.

$$Q_{cyc} = \int_0^{2\pi/\omega} \operatorname{Re}\{F_d(t)v_{rel}(t)\} dt \quad (2.6)$$

Note that since the displacement amplitudes of the oscillator mass and base were defined to be complex in Eq. (2.1) and Eq. (2.2), we only need to consider the real part of $F_d \cdot v_{rel}$ when expressing the power.

2.3.1 Viscoelastic heating

From Eq. (2.3) and Eq. (1.12), we can write an expression for the relative motion ($A - S$) of the moving mass with respect to the base at resonance.

$$(A - S) \Big|_{\omega=\omega_n} = \frac{B}{i\eta} \quad (2.7)$$

This system can be modeled as a linear mass-spring-dashpot system with effective elastic stiffness k' and loss factor η . The damping force for the oscillator can be expressed in terms of the elastic stiffness, loss factor, and relative displacement x_{rel} . The force is negative because it acts in the opposite direction of x_{rel} .

$$F_d(t) = -k'(1 + i\eta)x_{rel}(t) \quad (2.8)$$

This expression for the damping force can be input to Eq. (2.6) to determine the energy dissipated per cycle Q_{cyc} within the elastomer. The shear strain, and therefore the distribution of

generated heat, is assumed to be uniform throughout the elastomer. The resulting minus sign in Eq. (2.9) indicates that energy is released from the system.

$$\begin{aligned}
Q_{cyc} &= \oint F_d(t) dx_{rel} = \int_0^{2\pi/\omega} F_d(t) \frac{d}{dt}(x_{rel}(t)) dt \\
&= \int_0^{2\pi/\omega} \operatorname{Re} \left\{ -k'(1+i\eta)(x(t) - x_b(t)) \frac{d}{dt}(x(t) - x_b(t)) \right\} dt \\
&= -k'\omega|A - S|^2 \int_0^{2\pi/\omega} \sin(\omega t)(\eta \sin(\omega t) - \cos(\omega t)) dt \\
&= -\pi\eta k' |A - S|^2
\end{aligned} \tag{2.9}$$

Plugging in Eq. (2.7) for the relative displacement at resonance gives an expression for the dissipated heat per cycle at resonance.

$$Q_{cyc} \Big|_{\omega=\omega_n} = -\frac{\pi k'}{\eta} S^2 \tag{2.10}$$

For the calculation of Eq. (2.10), we rewrote the relative displacement term $A - S$ in terms of the transmissibility M , which was defined in Section 2.2.

$$A - S = \frac{S}{S}(A - S) = S \left(\frac{A}{S} - 1 \right) = S(M - 1) \tag{2.11}$$

The rate of heat generation \dot{Q}_{cyc} at resonance can be calculated from Eq. (2.10).

$$\dot{Q}_{cyc} = \frac{Q_{cyc}}{2\pi/\omega_n} = -\frac{k'\omega_n}{2\eta} S^2 \tag{2.12}$$

2.3.2 Magnetic induction heating

Eddy currents are expected to be induced near the surface of the conducting plate as a result of exposure to the time-varying magnetic field. The electrical resistance of the conducting plate causes heat dissipation by means of Joule heating. The interaction of the induced currents with the magnetic field effectively results in a force damping the motion of the conducting plate. Conservation

of energy requires that the work done by the damping force to resist the oscillator motion equals the amount of heat dissipated [3].

2.3.2.1 Electrical resistance and Joule heating

For a differential charge dq moving in the direction of $\hat{\mathbf{y}}$ with velocity $\mathbf{v} = d\mathbf{y}/dt$ through a differential volume $d\Gamma = da dy$, the current density J in the material can be expressed using the relationship in Eq. (2.13).

$$dq \mathbf{v} = dq \frac{d\mathbf{y}}{dt} = \frac{dq}{dt} d\mathbf{y} = I d\mathbf{y} = \mathbf{J} da dy = \mathbf{J} d\Gamma \quad (2.13)$$

The Lorentz force law (1.19) can then be rewritten in differential form to describe the force acting on the (volume element of) material through which there is continuous current flow.

$$d\mathbf{F} = dq \mathbf{E} + (\mathbf{J} \times \mathbf{B}) d\Gamma \quad (2.14)$$

The $dq \mathbf{E}$ term in Eq. (2.14) arises from end effects and surface charge migration due to motion of the current-carrying material, and it can be ignored for simplicity [41]. Setting the electric field to zero gives an adjusted expression for the differential force on the material.

$$d\mathbf{F} = (\mathbf{J} \times \mathbf{B}) d\Gamma \quad (2.15)$$

The general form of Ohm's law states that the current density J is the product of the material conductivity σ and the electric field \mathbf{E} , which is the force per unit charge.

$$\mathbf{J} = \sigma \mathbf{E} = \sigma \frac{\mathbf{F}}{q} \quad (2.16)$$

The expression for Lorentz force (1.19) allows the current density to be expressed in terms of the field strengths, material conductivity, and relative velocity.

$$\mathbf{J} = \sigma(\mathbf{E} + \mathbf{v} \times \mathbf{B}) \quad (2.17)$$

If the field strengths are known, the expression for \mathbf{J} from Eq. (2.17) can be plugged into Eq. (2.15) in order to write an expression for the force on the current-carrying material in terms of the known field strengths and material physical properties.

2.3.2.2 Heating in a uniform magnetic field

In order to induce eddy currents in a conducting plate exposed to a uniform magnetic field, the area of the conductor should be greater than that of the magnetic field [42]. As the conductor moves relative to the field, the edges of the exposed plate area experience changes in magnetic flux, which results in the generation of eddy currents.

If the induced electric surface field is ignored, the differential damping force acting on the plate is given by Eq. (2.15), where J is the induced current density within volume $d\Gamma$ and B is the magnetic flux density. The current density is given by Eq. (2.17), which can be simplified to reflect the simple geometry of this particular problem.

$$\begin{aligned} \mathbf{J} &= \sigma(\mathbf{v} \times \mathbf{B}) \\ &= \sigma v_y B_z \hat{\mathbf{x}} \end{aligned} \quad (2.18)$$

This expression for current density can be plugged into Eq. (2.15) to calculate the differential damping force dF_y on the plate. Note that the v_y term in the expression for current density is taken to be negative since the damping force is acting against the direction of motion.

$$\begin{aligned} dF_y &= J_x B_z d\Gamma = (-\sigma v_y B_z) B_z d\Gamma \\ &= -\sigma v_y B_z^2 d\Gamma \end{aligned} \quad (2.19)$$

If the magnetic field B_z is assumed to be constant, the integration is simple.

$$F_y = -\sigma v_y B_z^2 \Gamma \quad (2.20)$$

The energy dissipated per cycle Q_{cyc} can be determined from Eq. (2.6) using this expression for damping force.

$$\begin{aligned} Q_{cyc} &= \oint F_y(t) dx_{rel} = \int_0^{2\pi/\omega} F_y(t) \frac{d}{dt}(x_{rel}(t)) dt \\ &= \int_0^{2\pi/\omega} \operatorname{Re} \left\{ -\sigma B_z^2 \Gamma \left(\frac{d}{dt}(x(t) - x_b(t)) \right)^2 \right\} dt \\ &= -\sigma B_z^2 \Gamma \omega^2 |A - S|^2 \int_0^{2\pi/\omega} \sin^2(\omega t) dt \\ &= -\pi \sigma B_z^2 \Gamma \omega |A - S|^2 \end{aligned} \quad (2.21)$$

Since the oscillator (onto which the conducting plate is incorporated) would be designed such that the damping ratio ζ and natural frequency ω_n are known, Eq. (2.5) can be used with Eq. (2.21) to calculate the heat dissipation per cycle at resonance. This expression is analogous to Eq. (2.10) for viscoelastic heating; note that the damping term is again in the denominator.

$$Q_{cyc} \Big|_{\omega=\omega_n} = -\frac{\sigma B_z^2 \Gamma \omega_n}{4\zeta^2} S^2 \quad (2.22)$$

An expression for the overall rate of heat generation \dot{Q}_{cyc} at resonance for the magnetically damped oscillator can be written using the relationships in Eq. (2.11) and Eq. (2.4).

$$\dot{Q}_{cyc} = -\frac{\sigma \Gamma B_z^2 \omega_n^2}{8\zeta^2} S^2 \quad (2.23)$$

2.3.2.3 Heating in a varying magnetic field

In general, motion of a conducting plate within an alternating magnetic field, such as that produced by a pair (or array) of alternating permanent magnets, will result in more damping than the uniform field case since there will be greater variation in the magnetic flux density over the exposed plate

area [42, 43]. For an magnet configuration with two opposing alternating magnets, as shown in Figure 2.2b, the field distribution can be approximated by Eq. (2.24), where X and Y are the width and length of the plate area exposed to the field [41].

$$B(x, y) = B_z \sin\left(\frac{\pi x}{X}\right) \sin\left(\frac{\pi y}{Y}\right) \quad (2.24)$$

Integration of Eq. (2.19) can now be used to obtain the damping force for the alternating field case. The plate is assumed to have constant thickness Z , so the volume of the plate exposed to the field is $\Gamma = XYZ$.

$$\begin{aligned} F_d(t) &= \sigma v_{rel}(t) \int_0^\Gamma B(x, y)^2 d\Gamma' \\ &= B_z^2 \sigma v_{rel}(t) Z \int_0^X \int_0^Y \sin^2\left(\frac{\pi x}{X}\right) \sin^2\left(\frac{\pi y}{Y}\right) dx dy \\ &= \frac{1}{4} \sigma v_{rel}(t) B_z^2 \Gamma \end{aligned} \quad (2.25)$$

This expression for the damping force due to induction is identical to Eq. (2.20) except for a factor of 1/4. The rate of energy dissipation per cycle is then just 1/4 of that calculated for the constant field case. However, the magnetic field variation over the plate area is greater for the alternating magnet case, so more heat is generated.

$$\dot{Q}_{cyc} = -\frac{\sigma \Gamma B_z^2 \omega_n^2}{32 \zeta^2} S^2 \quad (2.26)$$

2.4 Linear heat flow model

Consider a closed thermodynamic system through which heat is conducted in a single direction through some material. Fourier's law of heat conduction relates the heat flow rate \dot{Q}_y to the thermal conductivity κ , cross-sectional area a , and the gradient of the temperature T along the direction y of heat flow [44].

$$\dot{Q}_y = -\kappa a \frac{dT}{dy} \quad (2.27)$$

The specific heat capacity c_p of a material having mass density ρ_m and volume Γ relates the stored heat dQ_s in a system to a corresponding increase in temperature dT .

$$dQ_s = \rho_m \Gamma c_p dT \quad (2.28)$$

Dividing both sides of Eq. (2.28) by time element dt gives us an expression for the rate of change of the heat stored within the material.

$$\dot{Q}_s = \rho_m \Gamma c_p \dot{T} \quad (2.29)$$

The rate of heat conducted through the material \dot{Q}_y is the difference between the rate at which heat is generated \dot{Q}_{gen} and the rate at which heat is stored \dot{Q}_s .

$$d\dot{Q}_y = d\dot{Q}_{gen} - d\dot{Q}_s \quad (2.30)$$

This relationship can be used to write the heat equation for the system, where the heat flux \dot{q} is defined as the heat flow rate per unit area ($\dot{q} = \dot{Q}/a$).

$$\begin{aligned} d\left(-\kappa a \frac{dT}{dy}\right) &= \dot{q}_{gen} a dy - \rho_m c_p \dot{T} a dy \\ \kappa \frac{d^2 T}{dy^2} + \dot{q}_{gen} &= \rho_m c_p \dot{T} \end{aligned} \quad (2.31)$$

2.4.1 Steady-state heat conduction

In steady state, the temperature rate of change \dot{T} becomes zero, and the steady-state heat equation Eq. (2.32) can be written for the system, assuming that the surface areas are equal for the conducted heat flow and generated heat flow.

$$\kappa \frac{d^2T}{dy^2} + \dot{q}_{gen} = 0 \quad (2.32)$$

For the present application, a constant heat flux \dot{q}_{in} is flowing into the system from one end ($y = 0$) while a constant temperature T_0 is maintained on the other end ($y = L$).

$$-\kappa \frac{dT}{dy} \Big|_{y=0} = \dot{q}_{in} \quad T \Big|_{y=L} = T_0 \quad (2.33)$$

If heat is only flowing into the system and no heat is generated within the system, then $\dot{q}_{gen} = 0$ and Eq. (2.32) becomes the simple second-order homogeneous equation $y''(t) = 0$ whose solution is a linear function of y .

$$T(y) = C_1 y + C_2 \quad (2.34)$$

By imposing the boundary conditions (2.33), values for the constants C_1 and C_2 can be calculated, along with the steady-state temperature distribution $T(y)$. Note that the temperature varies linearly from a maximum value T_h at $y = 0$ to the imposed value of T_0 at $y = L$.

$$T(y) = \frac{\dot{q}_{in}}{\kappa} (L - y) + T_0 \quad (2.35)$$

Recalling that the heat flow rate and heat flux are related by $\dot{q} = \dot{Q}/a$, where a is the surface area, the maximum temperature T_h can be written in terms of the thermal resistance R_T , which is defined in Eq. (2.37).

$$\begin{aligned} T_h &= T(0) = T_0 + \frac{L}{\kappa} \dot{q}_{in} \\ &= T_0 + \frac{L}{\kappa a} \dot{Q}_{in} \\ &= T_0 + R_T \dot{Q}_{in} \end{aligned} \quad (2.36)$$

For the harvester application, a dedicated conducting plate ideally stores all the heat dissipated from the damped oscillator. So \dot{Q}_{in} in Eq. (2.36), which is the rate of heat flow into the plate, is equal to $-\dot{Q}_{cyc}$, which is the rate of heat generated per cycle by (and flowing out of) the oscillator, integrated over the total number of cycles.

2.4.2 Transient heat flow

An equivalent circuit model is used to analyze transient heat flow through the system. This method is introduced in this section.

The obvious parallel between Eq. (2.36) and Ohm's law (1.17) leads to an analogy between electrical and heat flow systems. The source of heat generation in the thermal system analogous to a current source with value \dot{Q}_{gen} . The temperature relative to a reference (ambient) temperature at a particular point in the thermal system is analogous to a voltage relative to ground.

Resistance to heat flow through a material is modeled as thermal resistance R_T , which is defined in terms of the material thermal conductivity κ , thickness L in the direction of heat flow, and area a perpendicular to the direction of heat flow. As demonstrated above, specifying only the thermal resistance and the heat flow rate is sufficient to determine the steady-state temperature.

$$R_T = \frac{L}{\kappa a} \quad (2.37)$$

Determination of the transient temperature response requires a description of how a material stores heat. Heat stored is modeled as thermal capacitance C_T , which is defined as the product of the mass and specific heat capacity c_p .

$$C_T = \rho_m a L c_p \quad (2.38)$$

The thermal time constant τ is defined as the product of the thermal resistance and thermal capacitance. The time constant is the amount of time required for the system to reach 63% of the steady-state temperature [45].

$$\tau = R_T C_T \quad (2.39)$$

2.4.2.1 Heat conduction from elastomer

The method presented in Section 2.4 can be used to determine the increase in temperature due to energy dissipation within the elastomer.

Since the heat generated is assumed to be uniform throughout the material, the steady-state temperature increase can be estimated from Eq. (2.36) using the expression developed for \dot{Q}_{gen} . Note that while $\dot{Q}_{cyc} < 0$, indicating that generated heat is flowing *out* of the elastomer, $\dot{Q} > 0$ in Eq. (2.40), indicating that heat is flowing (from the elastomer) *into* the conducting plate in contact with the elastomer.

$$\begin{aligned} T_h &= T_0 + R_T \dot{Q} \\ &= T_0 + \frac{k' \omega_n}{2\eta} R_T S^2 \end{aligned} \quad (2.40)$$

An analogous circuit model can be used to estimate the transient temperature increase for the test article geometry shown in Figure 2.5. The heat flow model shown in Figure 2.3 represents half of the symmetric test article. The current source represents heat generation within the elastomer, and heat then flows to the centrally-located compliant mass and to the conducting aluminum plate fixed to the vibrating base. In this case, heat flows from the conducting plate through an insulator which is exposed (grounded) to ambient temperature T_0 . The heat source temperature T_h measured on the aluminum plate on the test article provides a measure of the heat that will be available to harvest using a TEG.

2.4.2.2 Heat conduction from magnetic induction heater

Combining Eq. (2.26) and Eq. (2.36) produces an expression for the steady-state temperature increase due to induction heating of a conducting metal plate from an alternating magnet oscillator.

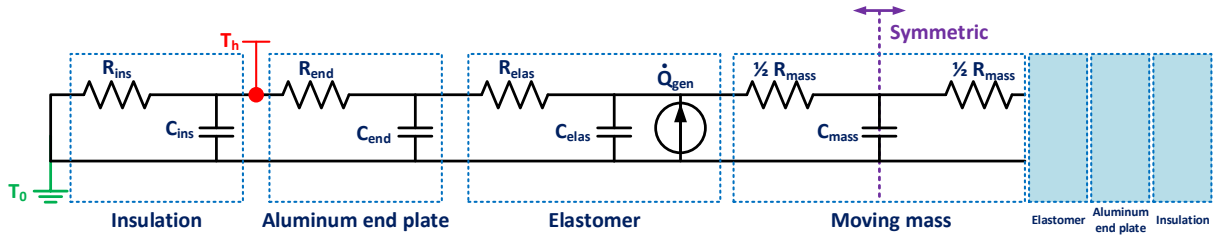


Figure 2.3: Transient heat flow circuit model for elastomer test article

$$T_h = T_0 + \frac{\sigma \Gamma B_z^2 \omega_n^2}{32 \zeta^2} R_T S^2 \quad (2.41)$$

For the ideal harvester configuration described in Figure 2.2b, the metal conductor being heated by eddy currents would be completely insulated and all of the heat would be conducted out through the TEG. The transient temperature profile would depend only on the insulator properties and the geometry of the conducting plate.

For the test fixture shown in Figure 2.6, a metal test coupon exposed to a time-varying magnetic field is heated by induction. The flow of eddy currents and subsequent heating due to the Joule effect are assumed to take place very close to both surfaces of the plate. Heat is conducted through the plate, which is exposed to air. The analogous thermal circuit for this system is shown in Figure 2.4.

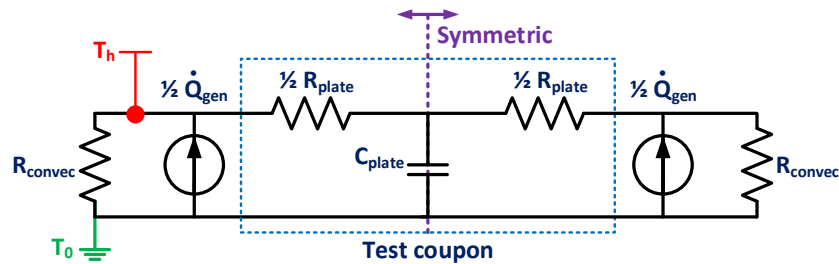


Figure 2.4: Heat flow model for metal plate heated by induction

Heat loss due to convection is modeled as a thermal resistance in Figure 2.4. The value of the convective thermal resistance R_{convec} is calculated from the convection heat transfer coefficient h_0 and area a_e of the exposed surface using the relationship in Eq. (2.42) [44, 45].

$$R_{convec} = \frac{1}{h_0 a_e} \quad (2.42)$$

2.5 Test articles

Two test setups were constructed for validation of the heat generation models, and to aid in development of the experimental and data analysis methods for use with future research. The analytical models were used to select the physical configuration, dimensions, and materials for the test articles and to predict their temperature response.

2.5.1 Visco-thermoelectric test article

From Eq. (2.40), maximizing the steady-state temperature of the VTE harvester requires an elastomer with a low loss factor and high stiffness. The concept for an elastomer test article is shown in Figure 2.5 and features a steel block bonded between two thin elastomer sheets which are fixed to the vibrating base. The elastomer sheets are designed to shear in the direction of base input in response to motion of the central steel block.

The purpose of the VTE test article was to assist in the development of an experimental method for characterizing the elastomer, and to perform the characterization test to determine the actual material properties of the elastomer. The heating model developed in this chapter is used to predict the temperature response of the test article. Upon determining the natural frequency of the oscillator, excitation of the test article at resonance and measurement of the resulting temperature increase is used to validate the heat generation model.

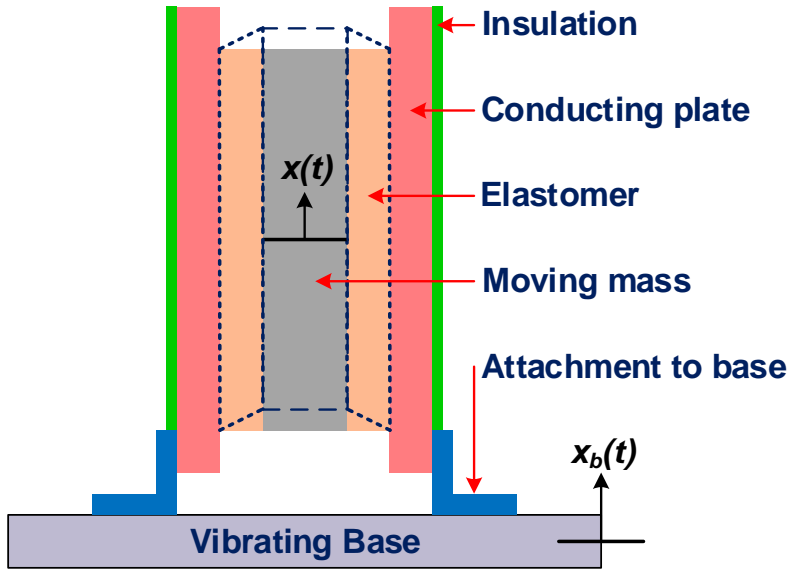


Figure 2.5: Concept for elastomer test article showing deformed oscillator shape (exaggerated)

2.5.2 Magneto-thermoelectric test article

A test setup was designed to measure the temperature increase of a fixed plate exposed to an oscillating magnetic field. Two fixtures were fabricated for the test: a magnetic fixture to be attached to the moving table of an electrodynamic shaker, and a static fixture attached to the unmoving shaker base. The moving magnetic fixture contains two NdFeB permanent magnets attached to a steel yoke in a parallel configuration to achieve a constant magnetic field, or in an alternating magnet configuration. The yoke consists of three steel blocks whose position can be adjusted to achieve the desired gap between the magnets. The test article concept is illustrated in Figure 2.6.

Originally, the magnetic fixture was designed such that the two magnets were polarized in the same direction so as to produce a constant magnetic field between them and through the test coupon. However, an alternating field configuration was found to be better for heat generation in the test coupon. As a result, the magnet placement was revised to the alternating configuration such that they were staggered and polarized in opposite directions.

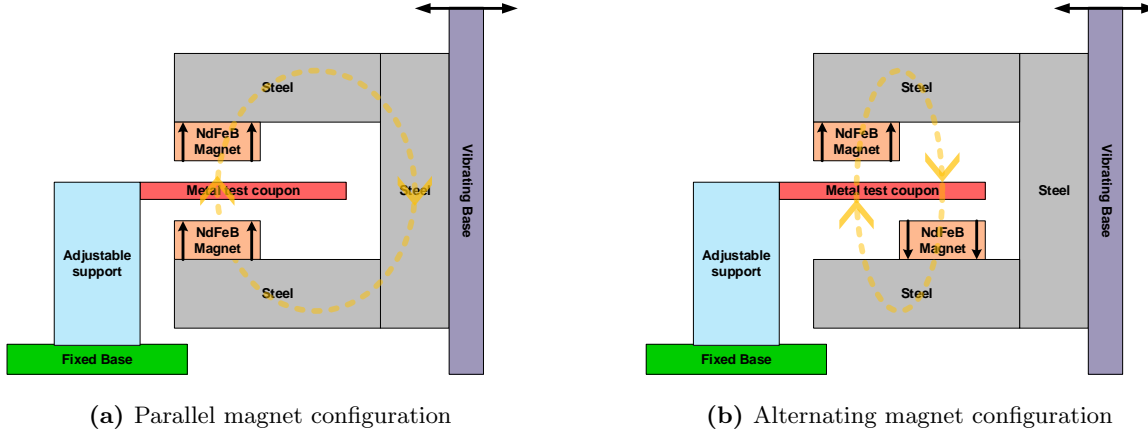


Figure 2.6: Induction heating test article conceptual configurations and flux path (not to scale)

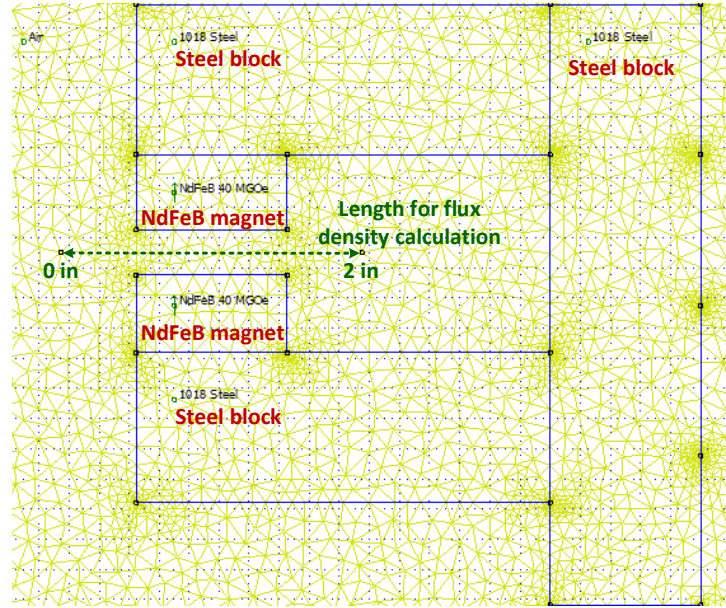
The static fixture was designed to allow for the metal test coupons to be easily installed or removed, and to allow the position of the fixture to be adjusted as necessary for desired placement of the coupon relative to the magnetic fixture.

2.5.2.1 Magnetic field estimation

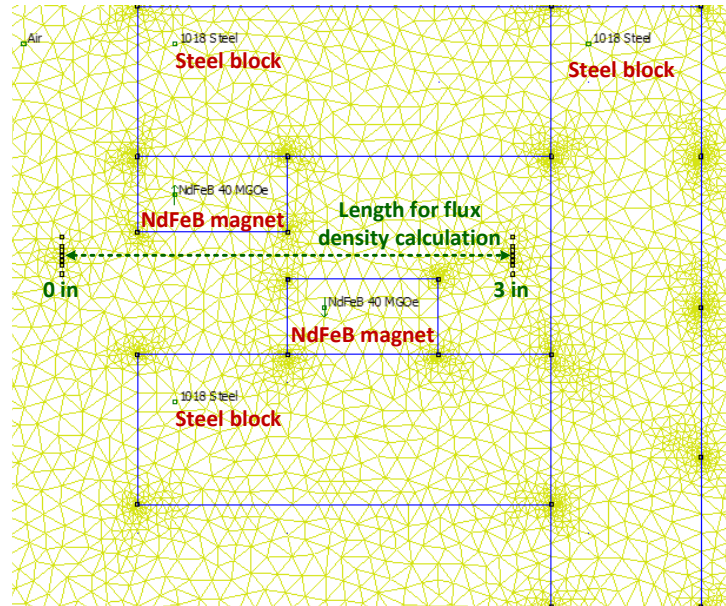
A 2D finite-element method magnetics (FEMM) analysis [46] aided in the design of the magnetic circuit for the induction test bed. The analysis showed that the parallel magnet design resulted in a fairly constant magnetic field through the air gap between the magnets. The yoke design and dimensions were selected to minimize flux leakage and maximize the flux directed through the air gap. The magnitude of the magnetic field for both the parallel and alternating magnet cases was calculated from the FEMM analysis for the purpose of predicting the temperature increase due to induction heating of the test coupon exposed to the magnetic field.

A scale cross section drawing was generated in FEMM using the dimensions of the actual test fixture. Materials were then matched to areas of the drawing corresponding to each part. A magnet field strength of 40 MGoe was the closest available strength for use in the FEMM software and was used instead of 42 MGoe, which was the strength of the actual magnets used on the fixture. The material surrounding the fixture was taken to be air for the analysis. Drawings for the parallel and

alternating magnet configuration, along with the mesh automatically generated by the software, are shown in Figure 2.7. The added points adjacent to the air gap between the magnets are reference points used to define a line across which the magnetic field was calculated based on the FEMM analysis. The results of the analysis are provided in Chapter 4.



(a) Parallel magnet configuration



(b) Alternating magnet configuration

Figure 2.7: Induction heating permanent magnet fixture drawing and mesh for finite element magnetics analysis

Chapter 3

Experimental Facilities and Methods

The hardware, test equipment, and methods used to validate the analytical models describing the behavior of the proposed harvester concept are identified in this chapter. Descriptions of the test fixtures used to generate heat by the two damping methods, laboratory equipment and software used for control and measurement, and experimental procedures are provided.

3.1 Concept validation hardware

The test articles and supporting hardware for validation of the heating models for the VTE and MTE harvester concepts are described in this section. The constructed test articles are based on the notional designs described in Section 2.5.

3.1.1 Visco-thermoelectric test fixture

A fixture was fabricated to allow for attachment of multiple elastomer test articles to the base of the shaker. For each test article, the shaker base was excited over a broad range of frequencies around the expected natural frequency of the device. An accelerometer on the base measured the input acceleration, and the velocity response of the oscillator mass in the direction of input was measured using the LDV.

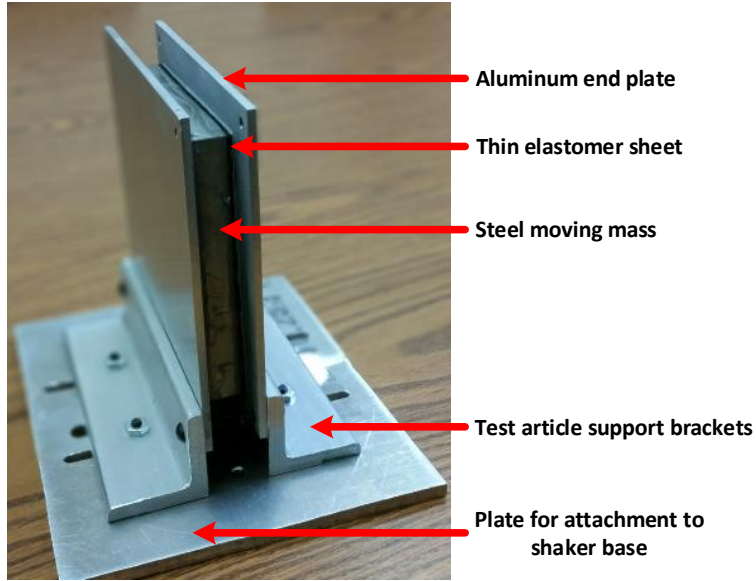


Figure 3.1: Test fixture for elastomer characterization and heating

Dimensions of the elastomer test article that was used are shown in Table 3.1. The test article components were sized for an oscillator natural frequency of 1 kHz. A low damping, high stiffness black rubber produced by LORD Corporation was selected for this application. The rubber has a specified shear modulus (G') of 460 psi (3.17 MPa) and loss factor (η) of 0.08. Two 4×4 inch sheets with thickness $1/16"$ were used. The rubber sheets were bonded to the plates using LORD 320/322 two-part epoxy adhesive [47].

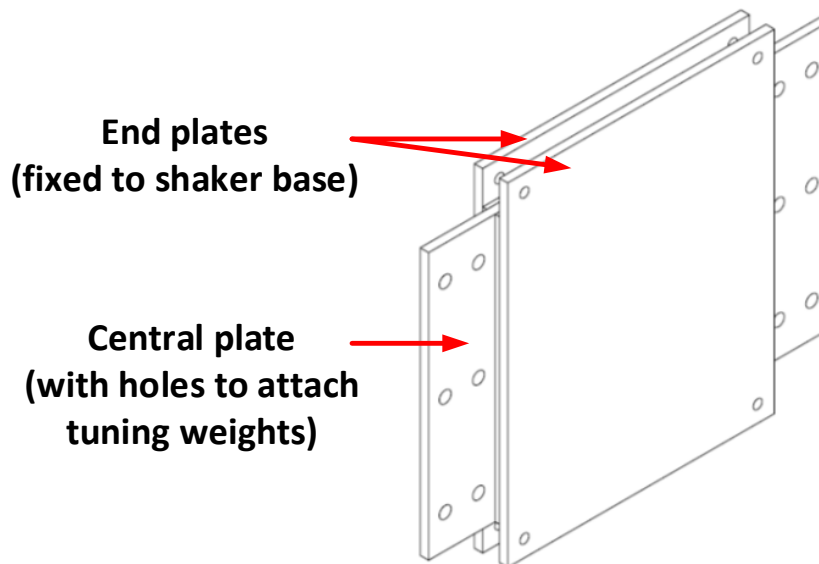
The elastic stiffness k' of the oscillator is given by Eq. (1.11). Note that since two elastomer sheets are used in the test article, the effective stiffness is $k'_{\text{eff}} = 2k'$. For the initial test article, the calculated stiffness was 41.2 MN/m based on the indicated elastomer properties, and the moving mass was required to be 1.04 kg to achieve a natural frequency of 1 kHz.

Additional test articles were also designed to have a configurable moving mass for characterization of elastomer structural properties with frequency. These new tunable units contain a thin aluminum plate sandwiched between the two parallel elastomer sheets, as illustrated in Figure 3.2.

Table 3.1: Elastomer test article properties

Parameter	Value
Moving mass	1.045 kg
Elastomer area	4 × 4 in.
Elastomer thickness	1/16 in.

The end plates are wider than the elastomer and contain holes for mounting steel masses. Four such test articles, each with a different elastomer thickness, were constructed for future testing.

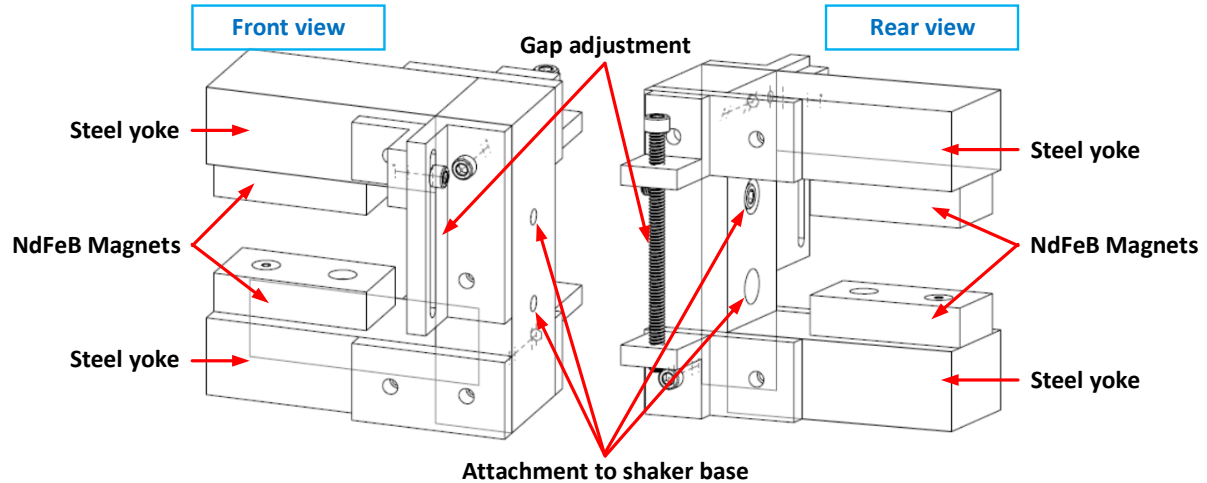
**Figure 3.2:** Proposed test fixture for variable frequency elastomer characterization

3.1.2 Magneto-thermoelectric test fixture

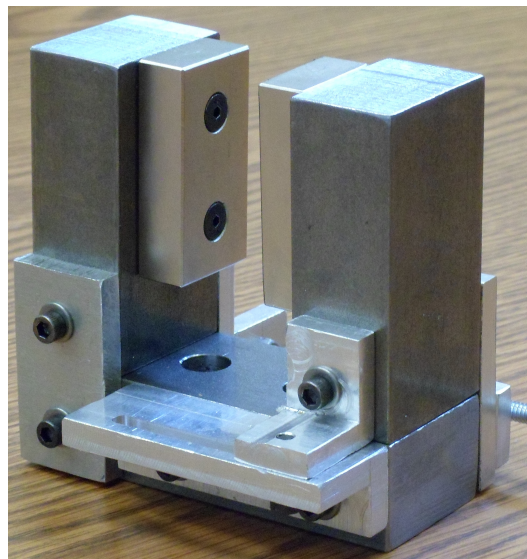
The test bed for validation of the MTE harvester concept consists of a moving magnetic fixture installed on the base of the shaker and a static support fixture to hold a thin metal test coupon in place relative to the moving magnetic fixture. The static fixture is adjustable to allow the position of the test coupon to be configured as necessary for a particular test.

The magnetic fixture is shown in Figure 3.3 and features two two neodymium iron boron (NdFeB) nickel-plated permanent magnets attached to a steel yoke. The magnets each have two countersunk holes to allow attachment to the yoke, which consists of three steel blocks fixed together by support plates. The purpose of the yoke is to maximize the flux through the air gap between the magnets, and the yoke is designed to allow the air gap to be adjusted to different widths.

The aluminum support plates used to hold together the three constituent blocks of the yoke ensure maximum contact between the two interfaces between the blocks. Features on either side of the fixture allow for adjustment of the gap between the two blocks containing the magnets, and holes are included for easy attachment of the fixture to a base for mounting onto the shaker. Appropriate safety precautions were taken when performing the gap adjustment to avoid contact of the two (very strong) magnets.



(a) Scale drawing indicating component parts



(b) Photograph of completed fixture

Figure 3.3: Magnetic fixture for induction heating test, shown in parallel magnet configuration

3.2 Test equipment configuration

An overview of control and measurement equipment used for evaluation of the test articles is provided in this section. The LabVIEW Run-Time Engine and National Instruments (NI) device drivers were installed onto a laptop computer, along with the control and monitoring software

application, which was used to interface with a NI CompactDAQ chassis containing analog input and output modules. The input module received data from a laser Doppler vibrometer (LDV), accelerometer, and thermistors as needed for a particular test. The output module provided the necessary excitation voltage for the thermistor measurements along with the desired voltage command to a power amplifier used to drive an electrodynamic shaker. The complete test setup is summarized in Figure 3.4.

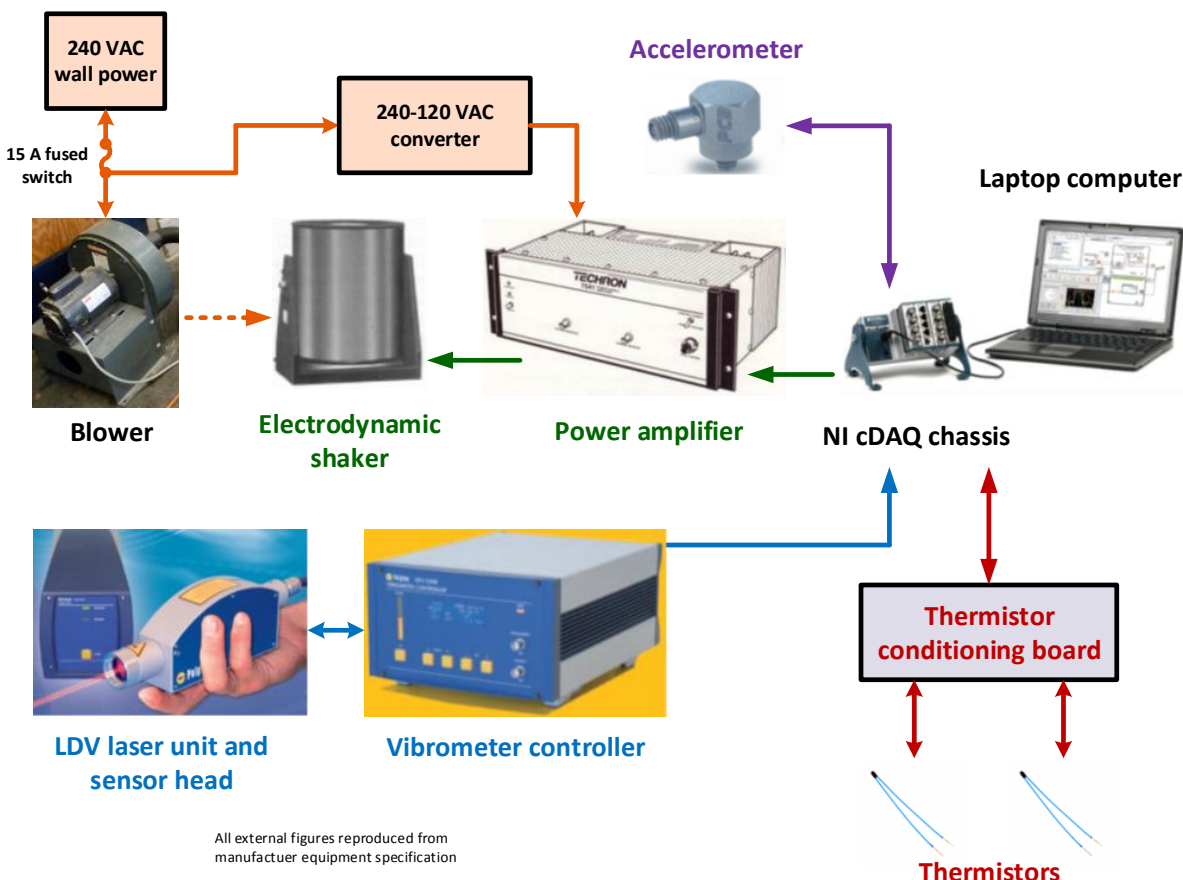


Figure 3.4: Lab test equipment interconnectivity

3.2.1 Control and data acquisition

An NI cDAQ-9174 chassis containing an NI 9263 analog output (AO) module and an NI 9234 analog input (AI) module was used for control and data acquisition. The AO module has 4 output channels, each with a maximum output range of ± 10 V. The AI module has 4 input channels, each with a maximum range of ± 10 V. The AI module was also selected for its ability to provide IEPE (integrated electronic piezoelectric) signal conditioning necessary for use of a voltage-mode accelerometer.

A single virtual instrument (VI) was developed in LabVIEW to interface with the cDAQ chassis and provide the necessary control, monitoring, and acquisition capabilities for all laboratory tests. Tabbed containers on the front panel, which is shown in Figure 3.5, contain controls for various settings or charts for monitoring data in real-time. Certain functions can be activated using the assigned keyboard shortcut as indicated on the front panel. The top-level block diagram for the VI is included in Appendix B.

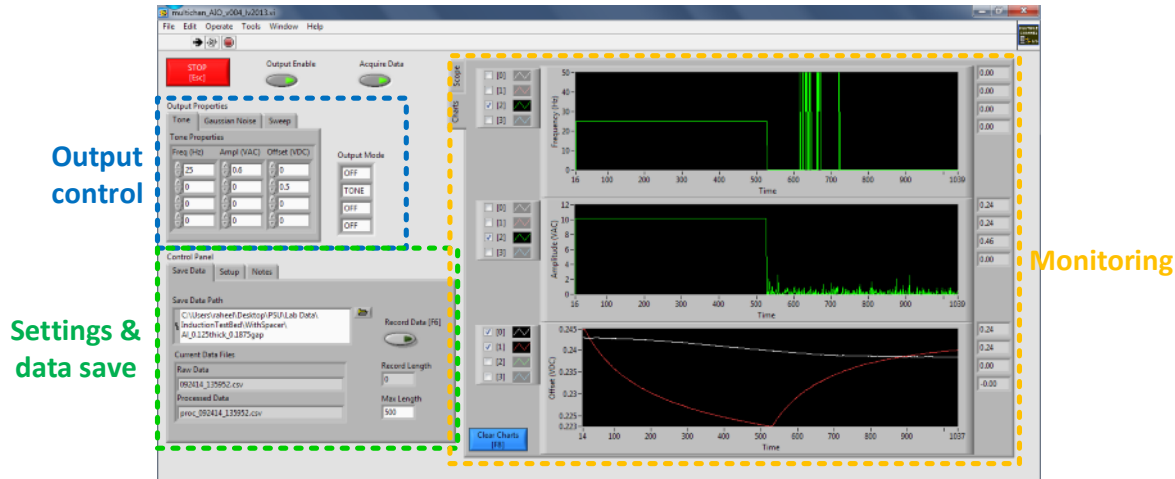


Figure 3.5: Control and measurement VI front panel

3.2.1.1 Software settings

Input and output settings are available to the user on the Setup page which has 4 tabs, as shown in Figure 3.6. The appropriate AO and AI channels should be selected or entered in the appropriate fields, along with the desired sampling rate and number of samples. The actual AO and AI sampling rates reported by the software are displayed for verification upon enabling output or input. If an accelerometer is used, specify the channel on which it is connected and ensure that the Enable ICP switch is green. The AI voltage range may also be modified if a different input module is used. AC or DC coupling can also be specified for each channel: use AC coupling for periodic measurements such as acceleration, and DC coupling for non-periodic measurements such as temperature.

The Scaling tab allows the user to specify scaling factors for each channel, which are used for calculating the amplitude of periodic signals displayed on the monitoring charts. For example, if an accelerometer with sensitivity 100 mV/g is connected to Channel 2, enter a scaling factor of 10 (in units of g/V) to monitor the acceleration amplitude in g's. The user can also specify cutoff frequencies for a bandpass filter applied to the raw signal before the frequency is calculated for a periodic signal.

3.2.1.2 Output and monitoring

Once all the settings have been specified on the Setup page, the Run arrow on the toolbar should be clicked to activate the program. The Output Enable button enables the specified output signals on all channels and also enables data acquisition. The red button or Esc key ends the data acquisition and disables the output on the next loop iteration.

The available output signals that can be generated by the VI are a sinusoidal tone, Gaussian white noise, or a sinusoidal chirp. The Output Properties page allows the user to specify properties for the desired output signal. For a tone output, specify the desired frequency, amplitude, and DC offset. For filtered noise, specify the standard deviation and filter frequencies. For a chirp, specify the amplitude, starting frequency, and ending frequency. The frequency of the generated chirp

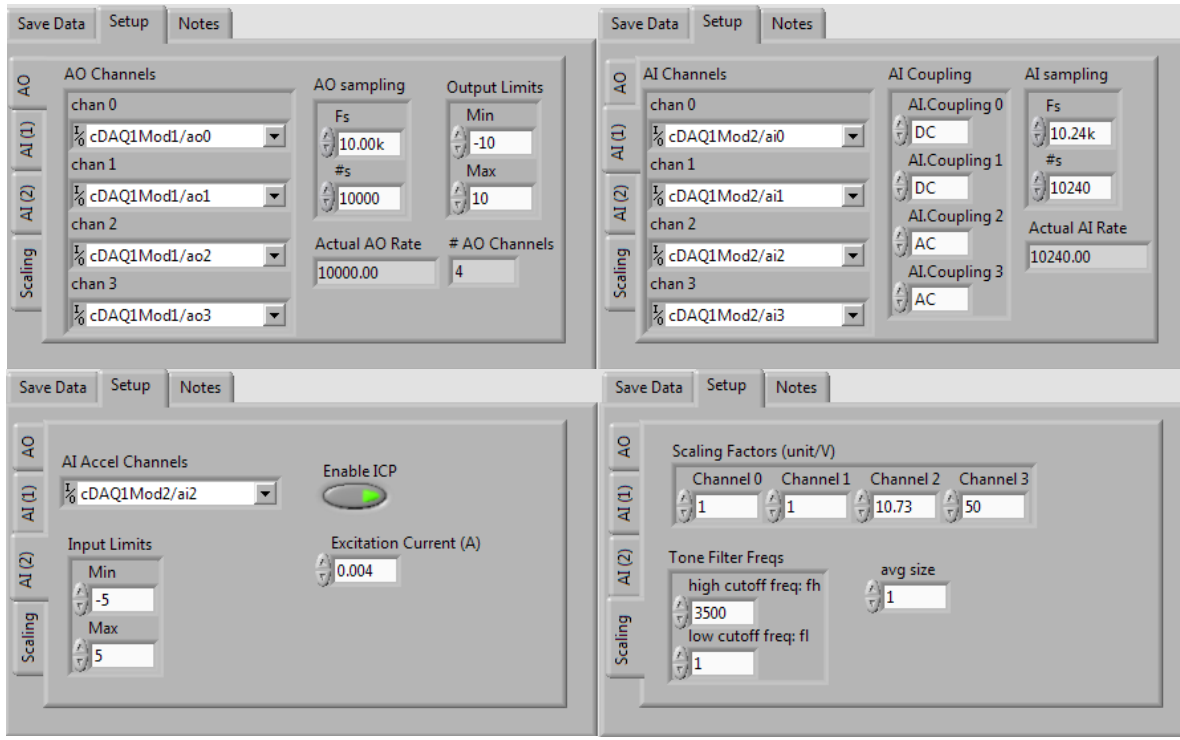


Figure 3.6: Available settings on VI Setup page

signal increases linearly over the specified frequency range over each sample period. The Output Mode selectors allow the user to specify the desired output signal on each channel.

The Scope page on the right side of the VI contains graphs that display the raw input and output voltages as measured or commanded by the cDAQ modules. These graphs reset each sample period are useful for verifying the correct output signal is being generated and that the input signals are not clipping. The three charts on the Charts page display the calculated frequency, scaled amplitude, and DC offset, respectively, of all four AI channels. The scaled amplitude is the peak-to-peak amplitude multiplied by the scaling factor specified on the Setup page. All chart values are recalculated and plotted each sample period. The chart is cleared when data acquisition is enabled, or it can be manually cleared by clicking the blue button or the F8 key.

3.2.1.3 Recording data

Pressing F6 or clicking the Record Data button on the Save Data page enables data collection. Data recording is automatically stopped after the number of sample periods specified in the Max Length field, or it can be manually stopped using the same button. The Current Data Files field displays the name of the files to which the data are saved, which are automatically generated from the current system date and time. The files are saved to the specified directory and updated with new data on each loop iteration (to minimize the risk of data loss in case of a PC crash).

Raw time-history voltage data for each of the four AI channels are saved to a CSV file, and the calculated tonal properties are saved to a second CSV file of the same name but prefixed with “proc_”. The raw data CSV file has four columns containing the measured voltage data for each of the AI channels, and each row of data corresponds to one loop iteration. The first column of the processed CSV file contains the time in milliseconds, and the following columns contain the frequency, scaled amplitude, and DC offset calculated by the VI for each channel (for a total of 10 columns).

3.2.2 Vibration measurement

A VTS-300 electrodynamic shaker was used to generate a specified mechanical vibration profile for dynamic testing. The shaker was powered by a Techron 7541 amplifier and connected to an appropriately sized blower. For all testing, the amplifier was operated at full gain for consistency, and only open-loop voltage control was provided.

A PCB-352C65 ICP® single-axis accelerometer was used to measure the actual acceleration achieved at the shaker base. Calibration data for the particular accelerometer used is shown in Table 3.2. The sensor was fixed to the shaker or base plate by gluing it to tape on a flat surface, which ensured a quickly removable but robust attachment.

A Polytec laser Doppler vibrometer (LDV) system, including a OFV-534 compact sensor head and OFV-2500 vibrometer controller, was used to measure the response of a test article subjected to base vibration input. The LDV was used to avoid the need to attach an accelerometer to the test

Table 3.2: PCB accelerometer calibration data

Model #	322C65
Serial #	28875
Sensitivity	93.2 mV/g
Frequency range	0.5–10000 Hz
Calibration date	03/02/2001

article which could possibly alter the dynamic response. The velocity output of the LDV controller was connected to the AI module. The sensitivity of the LDV was set to 50 mm/s/V, the low pass filter cutoff frequency was set to 20 kHz, and the high pass filter was turned off. The sensor head was fixed to a tripod and positioned directly above the test article such that the laser was incident upon and normal to the surface of the part. The lens was adjusted to focus the laser on a small piece of reflective tape placed on the part.

3.2.3 Thermal characterization and temperature measurement

A Corning 6795-400D PC-400D digital hot plate was used to characterize the response of TEG's to increasing surface temperature. The hot plate surface temperature was controlled using the built-in temperature dial, and the actual surface temperature was measured using a thermistor. A thin aluminum plate was placed on the ceramic surface of the hot plate to enforce a more uniform surface temperature distribution.

The thermistor conditioning board depicted in Figure 3.7 was built and used to interface the data acquisition system with two EPCOS B57861S202F40 NTC thermistors used for temperature measurement. An excitation voltage V_{ex} of 0.5 VDC was provided to the board from the AO module, and two 2.32Ω reference resistors R_0 were used on the board. The thermistors RT_1 and RT_2 were fixed to the flat test surfaces with tape. The DC voltages V_{T1} and V_{T2} across the two thermistors were read by two separate channels on the AI module.

The resistance R_T of each thermistor can be determined from the voltage V_T measured across it using Eq. (3.1), where R_0 and V_{ex} are the known values of the reference resistance and ex-

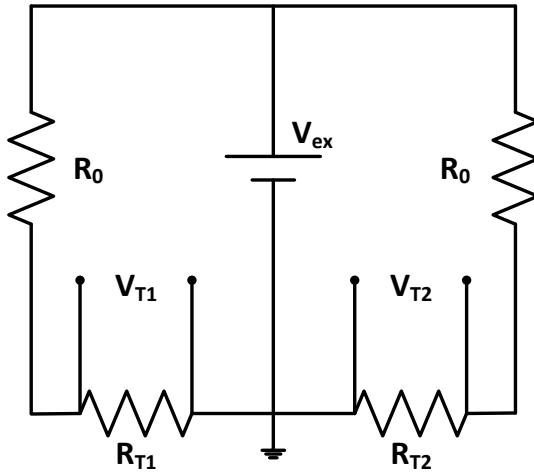


Figure 3.7: Dual thermistor conditioning circuit layout

citation voltage, respectively. The calculated thermistor resistance was matched to an absolute temperature in post-processing using data provided by the thermistor manufacturer. Note that *decreasing* thermistor voltage indicates *increasing* temperature. The temperature measured using both thermistors was verified prior to execution of the test procedures using a calibrated infrared laser thermometer on a reference surface.

$$R_T = \frac{R_0 V_T}{V_{ex} - V_T} \quad (3.1)$$

For all temperature measurements, both the test article and a reference surface were instrumented by thermistors. Any measured changes in the reference temperature (for example, due to a change in room temperature) were taken into account when calculating the temperature increase of the test article during a particular test condition, as illustrated for the representative data sample shown in Figure 3.8.

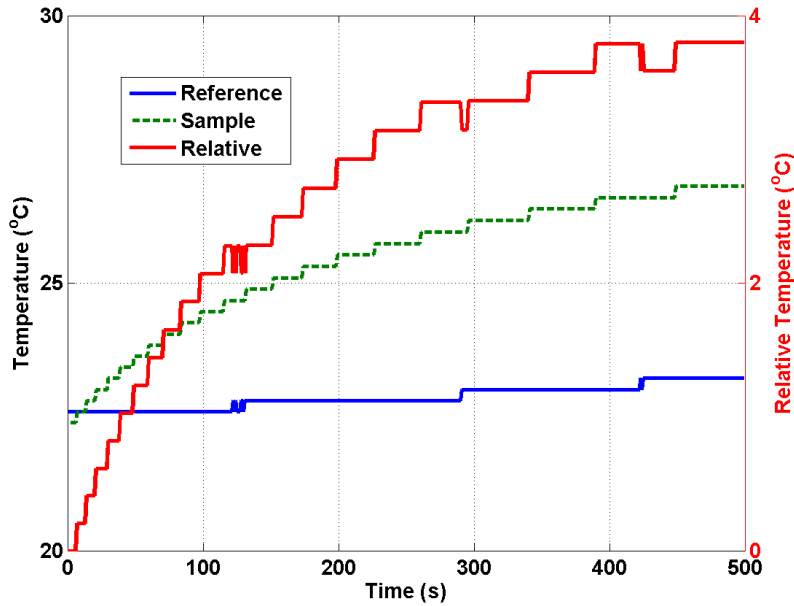


Figure 3.8: Relative temperature calculation from thermistor data

3.3 Test description

This section provides a description of the experimental methods employed to characterize the elastomer used in the VTE test article, to measure heat generation in the test articles, and to measure the power output of TEG's with increasing surface temperature.

3.3.1 Elastomer characterization

For structural characterization of the elastomer, the VTE test article was fixed to the base of the shaker and subjected to either white Gaussian noise or sinusoidal chirps. The base response of the shaker was measured with the accelerometer and the motion of the moving mass on the test article was measured using the LDV. The test setup is pictured in Figure 3.9.

3.3.1.1 Data preparation

The frequency-domain transfer function between the motion of the base and motion of the moving mass of the resonant test article was calculated in MATLAB from time-history data recorded from

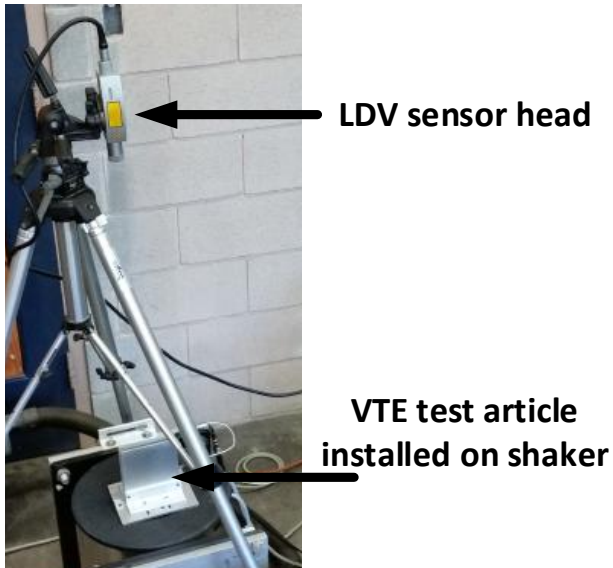


Figure 3.9: Test setup for elastomer characterization

the accelerometer and LDV. The time-history data for acceleration input to the base and velocity response of the oscillator that were recorded with the acquisition system were imported from the CSV file into MATLAB. The data were decimated from the original sampling rate of 10.24 kHz to 5.12 kHz to reduce processing time.

A 4th order zero-phase IIR Butterworth bandpass filter was applied to both the acceleration and velocity signals around the frequency range of interest (200–2000 Hz). The time-series data were transformed into the frequency domain via fast Fourier transform (FFT), and the frequency-domain velocity (output) data were scaled by the angular frequency to convert them to the same units as the input (acceleration).

The frequency spectra of the input (base acceleration) and the output (moving mass acceleration) for a representative test case (white Gaussian noise input) are shown in Figure 3.10. The magnitude-squared coherence between the output and input is also shown as a function of frequency, and the response data show good (approximately unity) coherence in the vicinity of 1 kHz, which is the expected natural frequency of the oscillator. Since the data were filtered prior to processing,

roll-off in the coherence is expected at high and low frequencies. The troughs in the input data and resulting loss of coherence around 800 Hz is most likely due to dynamics of the shaker system and sensor installation.

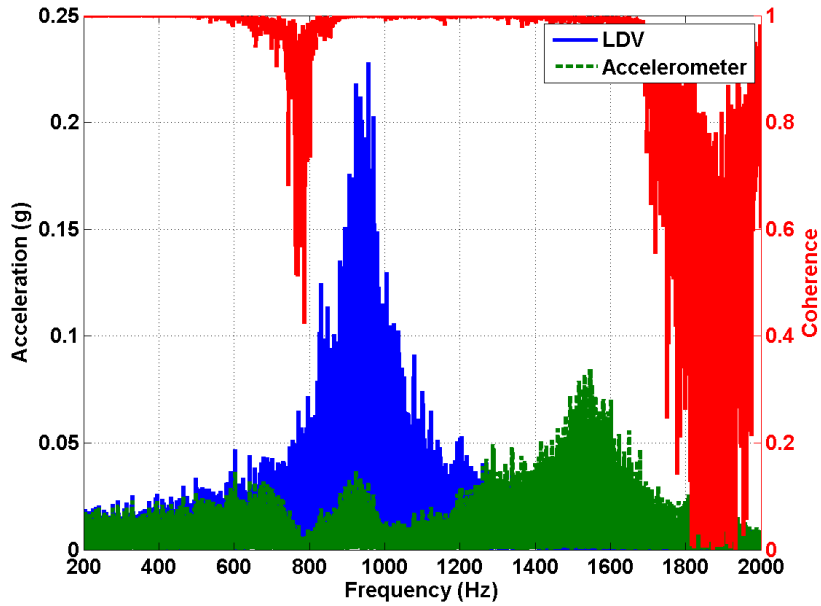


Figure 3.10: Sample data frequency spectra and coherence

3.3.1.2 Transfer function estimation and parameter identification

An estimate for the transfer function between input and output was calculated in MATLAB by taking the ratio of the cross power spectral density between the input and output, and the power spectral density of the input. The Bode plot of the calculated transfer function for a representative data set is shown in Figure 3.11, which also illustrates how the natural frequency, half-power bandwidth, and phase slope are calculated (not to scale). The smaller peak observed on the Bode plot is most likely due to the dynamics of the shaker system or sensor installation, and it was ignored for analysis purposes.

The natural frequency of the oscillator is simply the frequency at which the magnitude of the transfer function reaches its peak value. The damping ratio ζ of the oscillator was calculated from

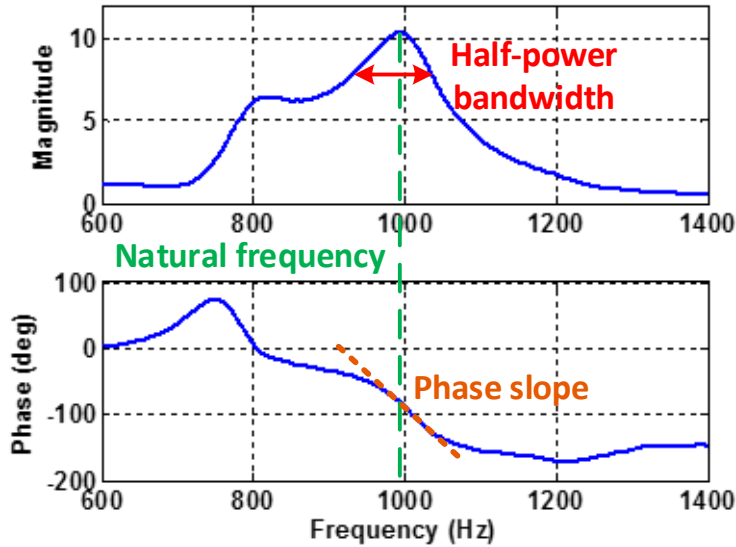


Figure 3.11: Illustration of parameter identification from transfer function Bode plot (not to scale)

Eq. (3.2) using either the half-power bandwidth $\Delta\omega_{1/2}$ or, equivalently, the slope Φ of the phase at the natural frequency [48].

$$\zeta = \frac{\Delta\omega_{1/2}}{2\omega_n} = -\frac{1}{\Phi\omega_n} \quad (3.2)$$

3.3.2 Elastomer heating

Once the natural frequency of the VTE test article was identified from the characterization test, the unit was subjected to sinusoidal base excitation at its natural frequency to generate heat within the elastomer. Thermally insulating foam tape was applied on the end plates and center steel mass of the VTE test article prior to the temperature response test. The insulating tape placed on the center steel mass did not contact the shearing elastomer, and it was not expected to have a significant effect on oscillator dynamics since the weight of insulating material was much less than that of the steel. Temperature increase of the test article was measured on the surface of one end plate, as pictured in Figure 3.12.

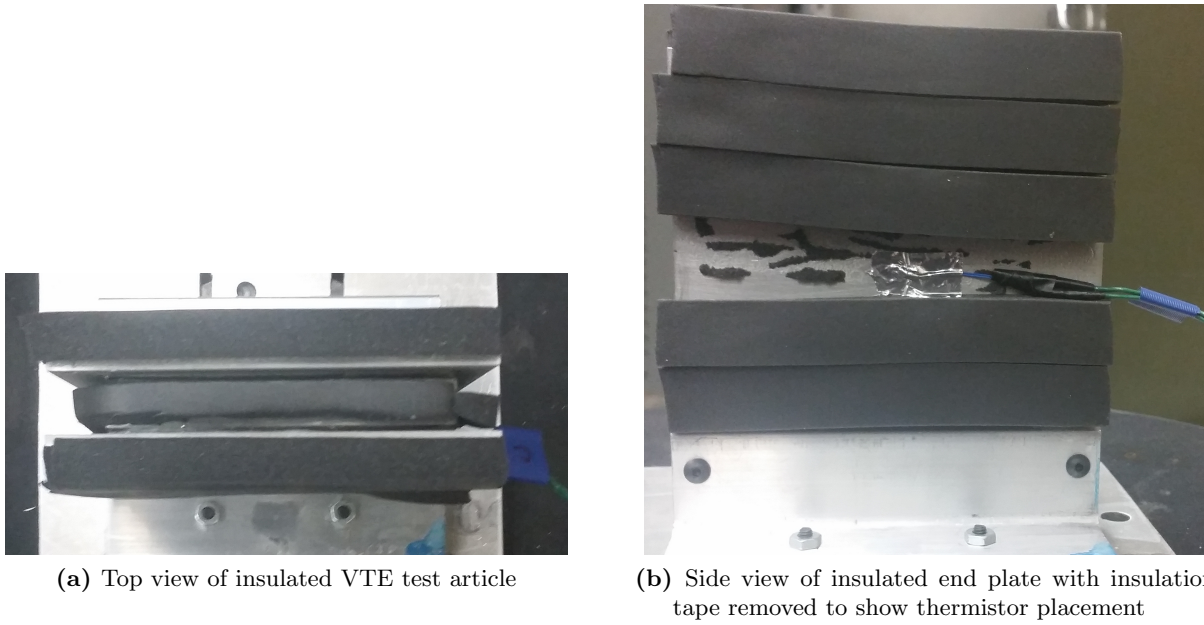


Figure 3.12: Thermal insulation and temperature measurement of VTE test article

3.3.3 Induction heating

Induction heating of an uninsulated metal test coupon was achieved by attaching the coupon to the static fixture and positioning it between the permanent magnets of the moving fixture. The base of the shaker onto which the permanent magnet fixture was attached was then subjected to sinusoidal excitation at a particular frequency. One face of the metal test coupon was instrumented with a thermistor to measure its surface temperature. This test setup is pictured in Figure 3.13.

Three aluminum test coupons with various thicknesses were used for this test. The magnetic fixture was configured to the alternating configuration after preliminary testing using the parallel configuration resulted in no measurable temperature increase of the test coupons at the levels achievable by the shaker system. Preliminary tests also revealed that the use of steel test coupons was not feasible due to the inability of the static support fixture to maintain the necessary air gap when subjected to high attractive force between the coupon and magnets.

For each test case, a sinusoidal voltage command was output to the shaker. The shaker base acceleration and test coupon surface temperature were determined from the measurement system

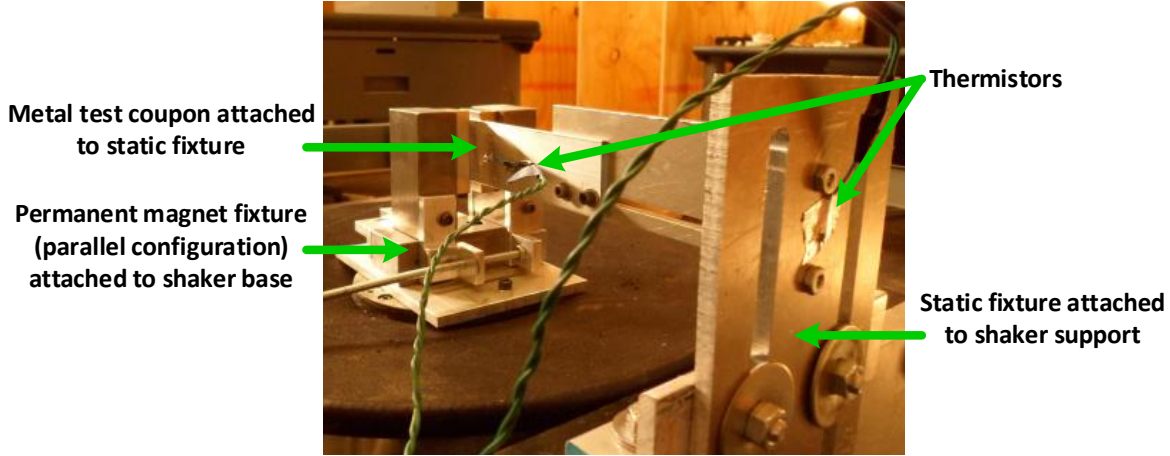


Figure 3.13: Test setup for magnetic induction heating

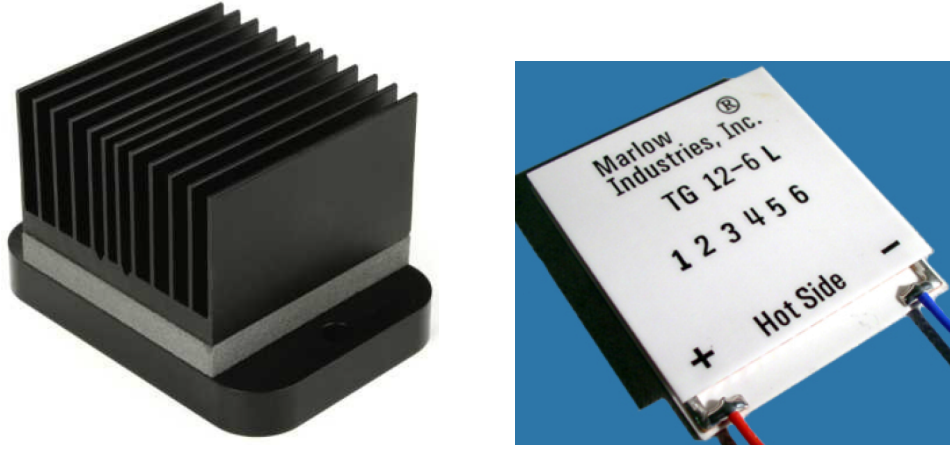
as described in Section 3.2. The surface temperature of the test coupon was allowed to stabilize to ambient temperature prior to the subsequent measurement.

3.3.4 Power output

A LORD-MicroStrain EH-Link wireless sensor node was selected as a representative device that would be powered by a vibration energy harvester. This sensor node is able to accommodate various types of input power sources and sensors, and it adjusts the data sampling and transmission rate based on the available power from the energy harvester. The input impedance of the device for test purposes was taken to be 6Ω based on information provided by the device manufacturer [49].

Two thermoelectric generators were characterized to determine the available power output with increasing temperature. A thermal harvester with an integrated base and heat sink from LORD-MicroStrain, and a Marlow TG12-6L thermoelectric generator were subjected to the power output test. These units are pictured in Figure 3.14.

For the Marlow TEG, an aluminum heat sink was placed on the “cold” side of the unit with Arctic Silver 5 thermal compound spread thinly and evenly between the TEG and heat sink. For both units, the output of the TEG was connected to a 6Ω resistor and the voltage across the load



(a) MicroStrain TEG with integrated heat sink

(b) Marlow TG12-6L TEG

Figure 3.14: Thermoelectric generators used for characterization tests

resistor was measured by the data acquisition system. The TEG was placed on the hot plate, and both the surface of the hot plate in contact with the TEG and heat sink exposed to the ambient air were instrumented with thermistors. The temperature of the hot plate was increased incrementally and the temperatures of the hot and cold surfaces were recorded using the data acquisition system. The test setup is pictured in Figure 3.15.

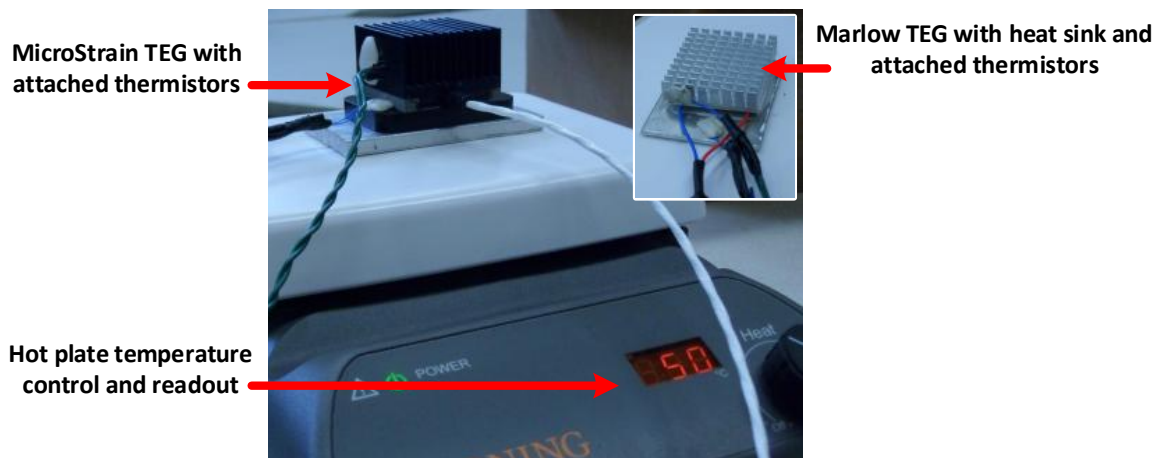


Figure 3.15: Test setup for TEG characterization

Chapter 4

Results

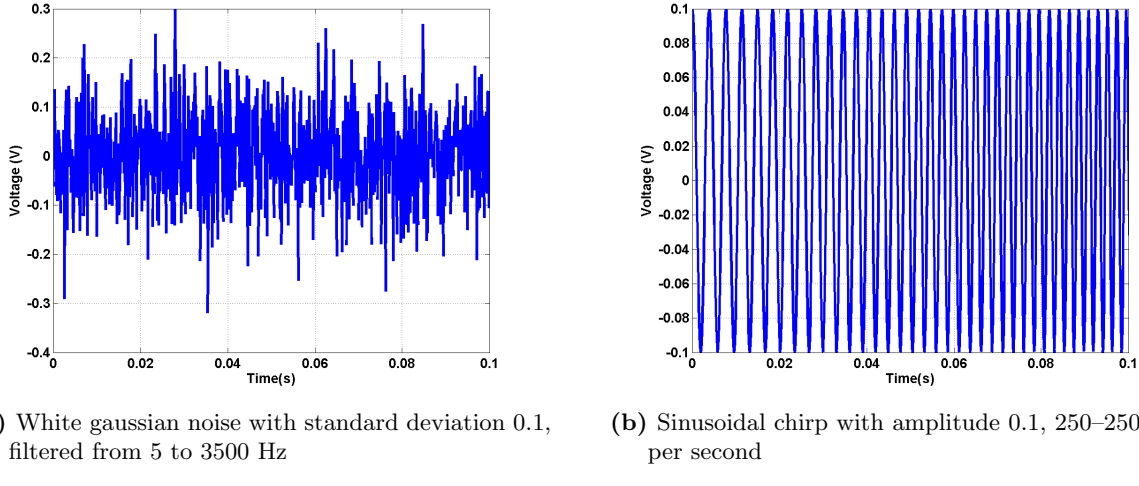
This chapter details the results of the engineering analysis and laboratory testing. Structural characterization testing of the VTE test article is first described, and the experimentally determined structural properties are input into the viscoelastic heating model to predict the heat output of the test article. The VTE test article is then driven at the measured natural frequency, and the measured temperature response is compared to the prediction.

The induction heating test fixture is used to induce surface heating of several aluminum test coupons, and the temperature increase of the coupons is measured and compared to model predictions.

4.1 Experimental characterization of elastomer

Structural characterization testing of the elastomer test article was performed using the experimental setup and method described in Section 3.3.1. The test article was fixed to the shaker base and excited with either a random Gaussian or sinusoidal chirp voltage input; examples of these two excitation profiles (shown only over 100 ms for clarity) are depicted in Figure 4.1.

An estimate for the transfer function between the applied base excitation, measured using an accelerometer at the base, and the response of the moving mass, measured using a laser Doppler vibrometer (LDV), was generated for each test case using the method described in Section 3.3. From



(a) White gaussian noise with standard deviation 0.1, filtered from 5 to 3500 Hz (b) Sinusoidal chirp with amplitude 0.1, 250–2500 Hz per second

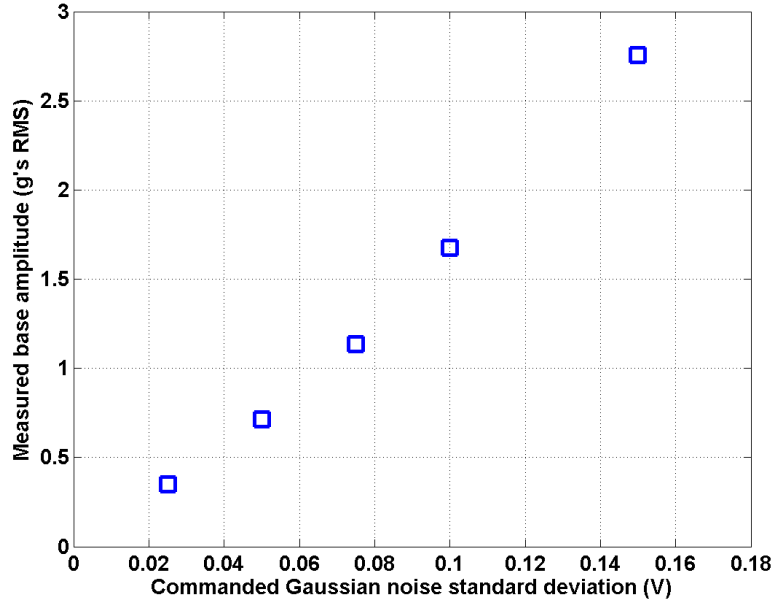
Figure 4.1: Commanded base excitation input voltage profiles

each transfer function, an estimate for the natural frequency and damping ratio were calculated from the frequency response. These calculated structural properties were then plotted against the measured amplitude of the base input to show their dependence on base excitation. The average amplitude of the input signal was calculated by integrating the power spectral density (PSD) of the acceleration over the frequency range of interest (in this case, 500–1500 Hz). The measured vibration response of the shaker base to input commands is depicted in Figure 4.2.

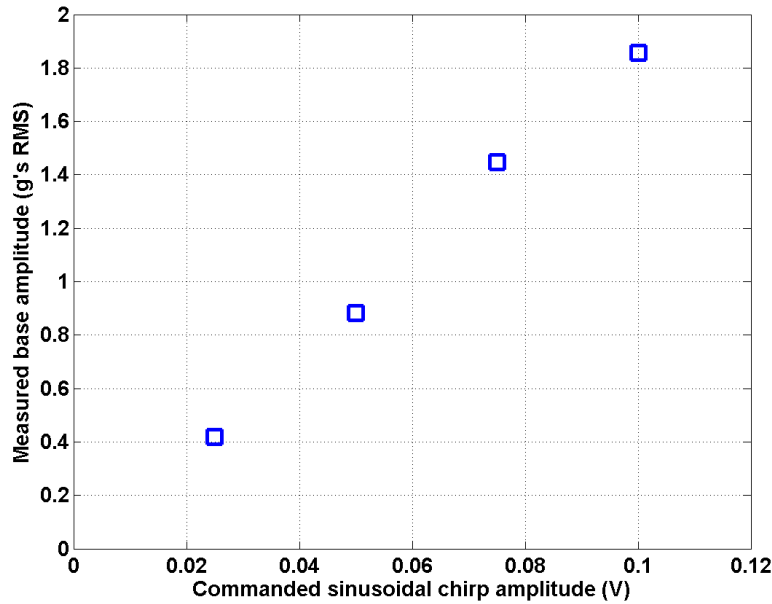
The measured natural frequency ω_n is plotted against the input amplitude in Figure 4.3. The mean value and specification value are also shown for each excitation case. The data show a slight downward trend in natural frequency with increasing input amplitude.

The measured elastomer loss factor η is plotted against the input acceleration in Figure 4.4. These data show that the loss factor also decreases as the input amplitude increases.

The measured values of natural frequency and loss factor were averaged over all test cases, and the shear modulus G of the elastomer was calculated using the average value of the natural frequency along with the test article dimensions. These results are shown in Table 4.1, along with values specified by the manufacturer for this material.

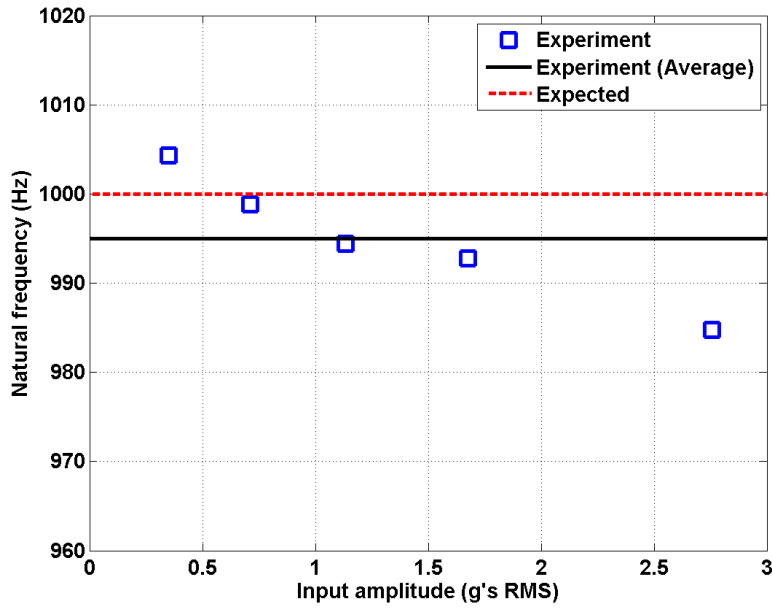


(a) Measured response to white noise command

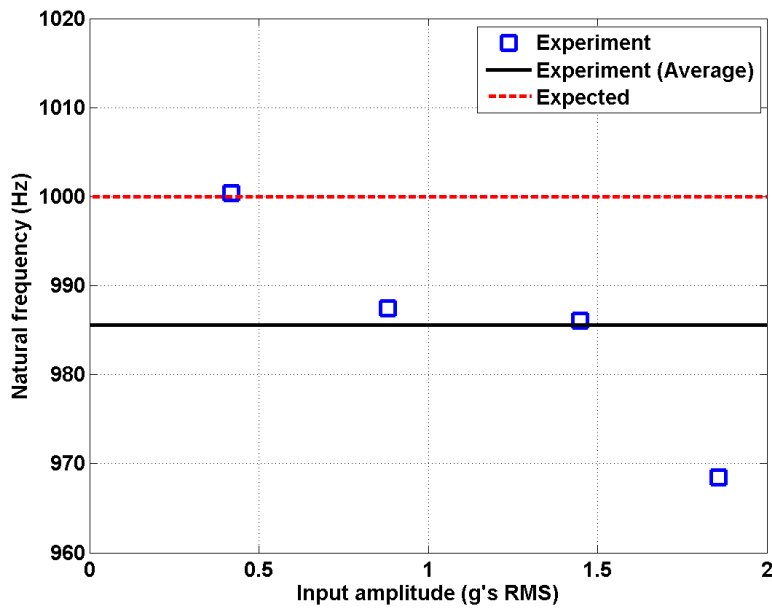


(b) Measured response to sinusoidal chirp command

Figure 4.2: Measured RMS acceleration response of electrodynamic shaker base (over 500–1500 Hz) with test article installed

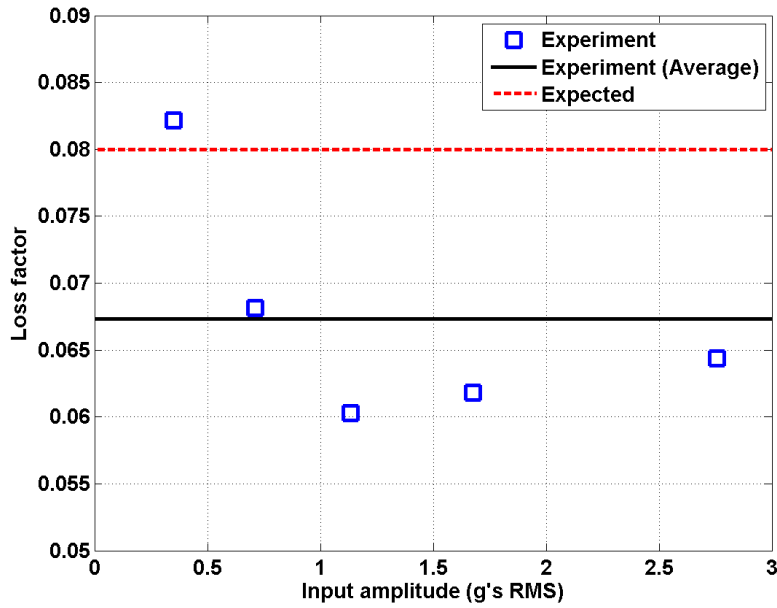


(a) Random excitation

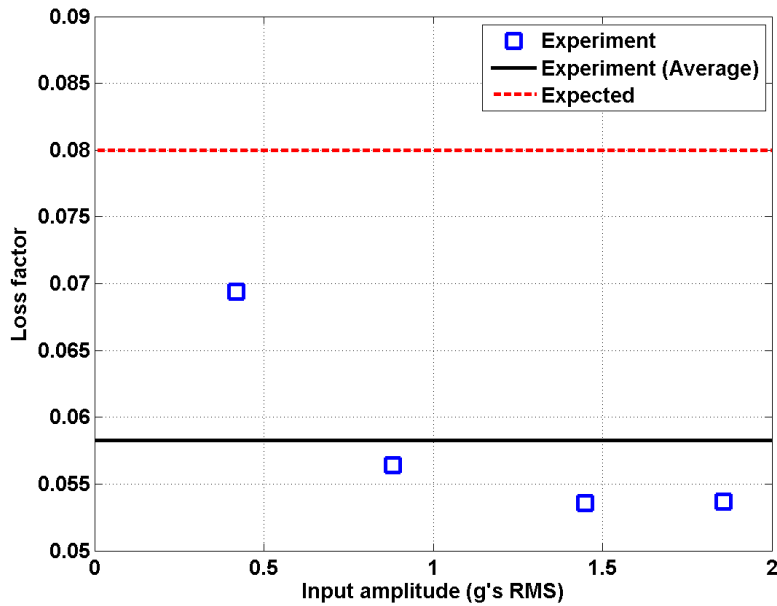


(b) Chirp excitation

Figure 4.3: Measured elastomer natural frequency vs. input amplitude



(a) Random excitation



(b) Chirp excitation

Figure 4.4: Measured elastomer loss factor vs. input amplitude

The data show that the test article has a slightly lower loss factor, natural frequency, and stiffness on average than indicated from the specification data. At low input amplitude, the loss factor matches the specification value much more closely.

Table 4.1: Measured and specified elastomer material properties

Parameter	Spec value	Avg experimental value	Deviation from spec
Natural frequency	1000 Hz	990.8 Hz	<1%
Loss factor	0.08	0.063	21%
Shear modulus	3.17 MPa (460 psi)	3.11 MPa (451.7 psi)	2%

4.2 Elastomer heating simulation

The measured elastomer material properties were used to predict the temperature response of the VTE test article when excited at resonance. The actual temperature response to resonant excitation was then measured experimentally. For the initial simulation, the dynamic and temperature response of the test article was modeled for two notional high stiffness cases. The results of the elastomer characterization test are then used to simulate the response of the test article.

4.2.1 Notional test article

The analytical result in Eq. (2.40) indicates that the steady-state temperature increase of the test article at resonance increases with increasing stiffness and decreasing loss factor. An early study of the VTE harvesting concept [50] analyzed elastomer heat generation from very stiff, low loss factor elastomers. Two sets of elastomer properties are identified in Table 4.2 which have high shear moduli and a loss factor of 0.01.

The oscillator stiffness is calculated using the known shear modulus and dimensions of the notional elastomer. The required moving mass is determined from the calculated elastomer stiffness and by imposing the desired natural frequency of 1 kHz. These values along with the heat generation rate and predicted steady-state temperature increase are shown in Table 4.3. These steady-state

Table 4.2: Elastomer properties for initial conceptual test cases

Parameter	Value (Case A)	Value (Case B)
Cross-section area	$70 \times 70 \text{ mm}^2$	$70 \times 70 \text{ mm}^2$
Thickness	10 mm	10 mm
Loss factor (η)	0.01	0.01
Shear modulus (G)	40 MPa	170 MPa

temperature results are calculated for a base input of 4 g's using Eq. (2.40), which states that the increase in temperature is the product of the heat generation rate and the thermal resistance R_T .

Table 4.3: Predicted oscillator properties and response for notional cases

Parameter	Value (Case A)	Value (Case B)
Moving mass	0.5 kg	2.1 kg
Elastomer stiffness	19.6 MN/m	83.3 MN/m
Total device mass	1.3 kg	4.5 kg
Heat generation rate	1.52 W	4.56 W
Steady-state temperature increase ($R_T = 3$)	4.6 °C	19.4 °C

The results in Table 4.3 shown are for a thermal resistance of $R_T = 3$, but insulating the conductor in contact with the heated elastomer (as illustrated in Figure 2.5) will increase R_T (and therefore the resulting steady-state temperature increase) depending on the quality of the insulating material (a good insulator has low thermal conductivity) and on the geometry of the insulating layer (a thicker insulator will also have lower conductivity). This value for R_T was calculated using the material thermal properties shown in Table 4.4 for an insulator with thickness 5 cm and surface area equal to that of the elastomer.

Note also that while the insulating layer provides most of the thermal resistance between the heated elastomer and the surrounding environment, a small contribution is also made by the conducting layer as well as by the elastomer itself. To clarify this point, consider a complete one-dimensional transient heat-flow model for this system, as shown in Figure 2.3, which is used to predict the transient temperature response.

Table 4.4: Component material thermal properties

Material	Specific Heat Capacity	Thermal Conductivity	Mass Density
Carbon steel	486 J/kg°C	51.9 W/m°C	7870 kg/m ³
Rubber	2000 J/kg°C	1.2 W/m°C	1500 kg/m ³
Aluminum	900 J/kg°C	210 W/m°C	2700 kg/m ³
Foam insulation	1250 J/kg°C	0.03 W/m°C	480 kg/m ³

The component thermal circuit parameters for the notional test article are listed in Table 4.5, and the response for both cases are shown in Figure 4.5. Whereas a substantial temperature increase is indicated for both cases, the time constants are too high to consider these notional test articles to be practical.

Table 4.5: Elastomer test article thermal circuit parameters, notional cases

Component	Resistance	Capacitance	Time constant (s)
Steel moving mass (Case A)	38.4×10^{-3}	240	9.3
Steel moving mass (Case B)	0.163	1.0×10^3	167
Elastomer	1.48	169	250
Al end plate	0.8×10^{-3}	137×10^3	116
Insulation	2.96	16.9×10^3	50×10^3

The transient temperature response is very sensitive to the thermal resistance of the insulation layer because of its low thermal conductivity. Reducing the thickness of the insulating layer can significantly reduce the time required to reach the steady-state temperature, but also reduces the steady-state temperature that can be achieved. Using the higher stiffness (170 MPa) elastomer with a thinner insulating layer (0.5 cm instead of 5 cm) and increasing the base excitation amplitude to 6 g's results in the response shown in Figure 4.6. The simulation shows both the time constant and steady-state temperature decreased for this case.

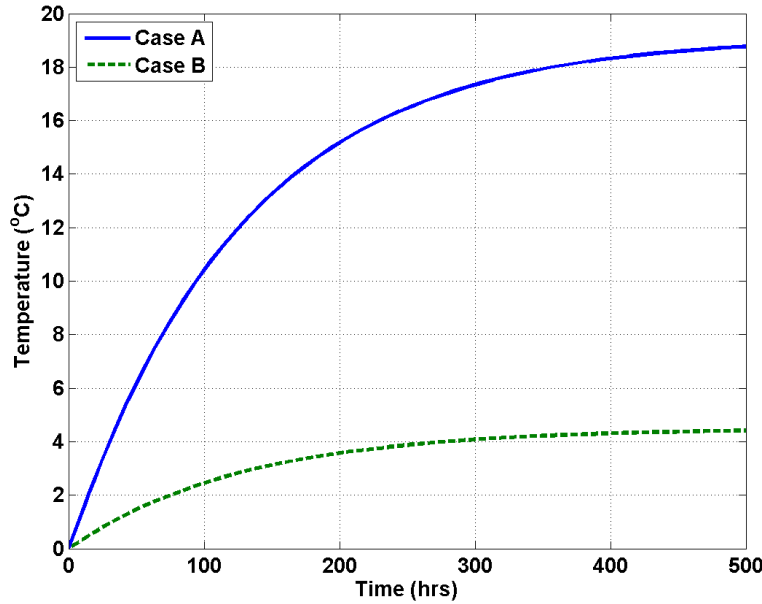


Figure 4.5: Predicted transient temperature response for notional simulation cases

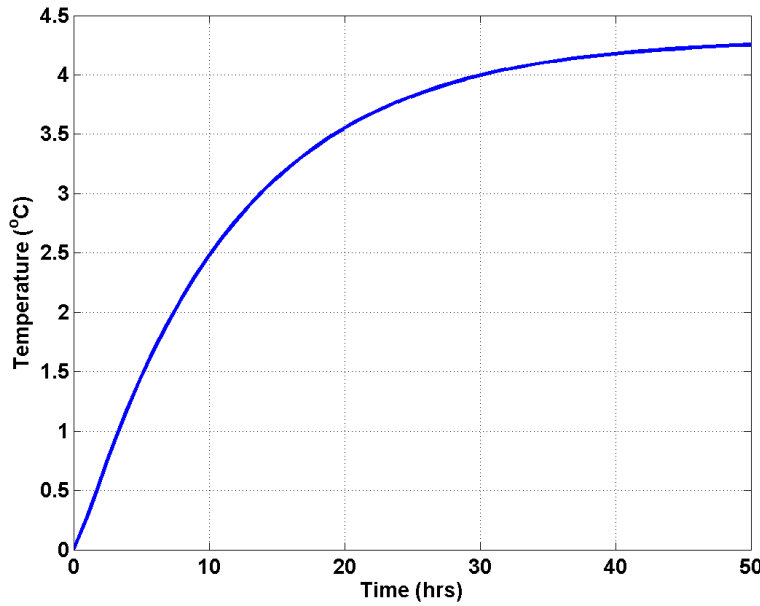


Figure 4.6: Predicted transient temperature response for notional simulation Case B with reduced insulation thickness

4.2.2 Actual test article

The experimentally-determined properties of the available elastomer used in construction of the VTE test article were used to simulate its temperature response. The dimensions of the test article are listed in Figure 4.6.

Table 4.6: Elastomer dimensions for experimental VTE test article

Parameter	Value
Cross-section area	$4 \times 4 \text{ in}^2$
Thickness	1/16 in

The material properties listed on the elastomer specification were used to design the test article. The material properties obtained from experimental characterization of the elastomer (Section 4.1) are then used to generate a second set of predictions for comparison to experimental data. The steady-state temperature predictions are listed in Table 4.7. The thermal circuit parameters for the transient model are listed in Table 4.8.

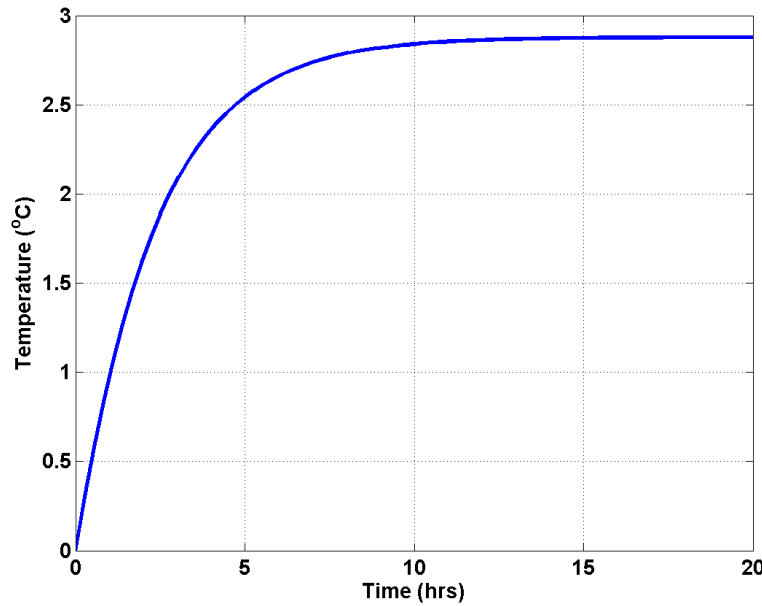
Table 4.7: Predicted test article response for VTE test article

Parameter	Spec elastomer	Actual elastomer
Heat generation rate	320.4 mW	406.2 mW
Steady-state temperature increase	6.3 °C	8.0 °C

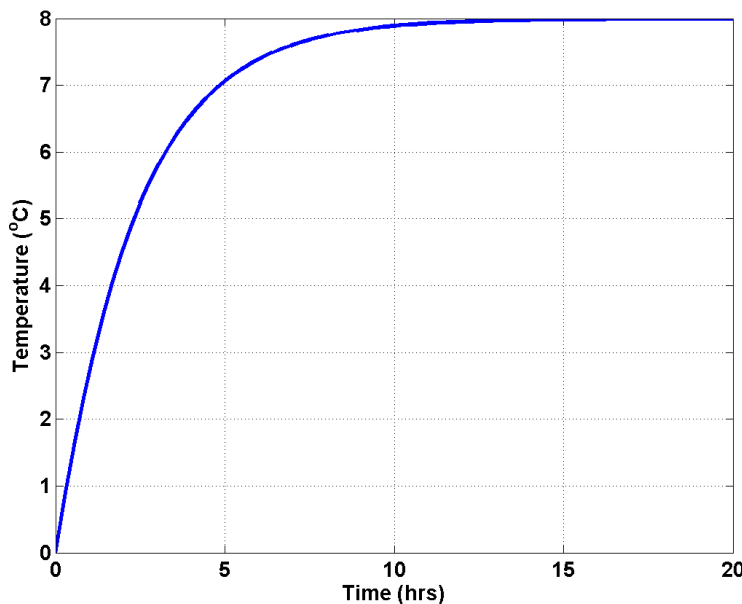
Table 4.8: Elastomer thermal circuit parameters for VTE test article

Component	Resistance	Capacitance	Time constant (s)
Steel moving mass	12×10^{-3}	253.7	3.0
Elastomer	128×10^{-3}	49.2	6.3
Al end plate	0.9×10^{-3}	124.4	0.1
Insulation	19.7	122.9	2.4×10^3

The results of the transient thermal simulation are shown in Figure 4.7 for base acceleration levels of 3 g's and 5 g's. The model uses the average values for the elastomer material properties listed in Table 4.1. The predicted time constant is much less for this case compared to the notional high stiffness elastomer cases.



(a) Base excitation of 3 g's



(b) Base excitation of 5 g's

Figure 4.7: Predicted transient temperature response for actual VTE test article

4.3 Induction heating simulation

Results of the magnetic field analysis performed using FEMM are described in this section. The results of the magnetic field analysis are used along with the heat generation model to predict the temperature response due to induction heating.

4.3.1 Magnetic field analysis

The finite element analysis method described in Section 2.5 was used to generate an estimate for the magnetic flux density for this test article configuration using the FEMM software package. A two-dimensional layout of the magnetic circuit with appropriate dimensions for the test article cross section was drawn in FEMM, and the appropriate material properties were defined for the corresponding regions on the diagram. The input to the FEMM solver is shown in Figure 2.7, and the calculated magnetic flux density over the cross section is shown in Figure 4.8.

Using the test points corresponding to the center and three coupon thicknesses, the surface flux density was extracted from the solver for each case. The flux density results for the alternating magnet case are shown in Figure 4.9b. Because the test line associated with the largest coupon thickness ($1/4"$) was so close to a corner node, the solver result for the flux density associated with this thickness is not be as reliable as the others. With the exception of the $1/4"$ coupon, a small variation of about 0.5 T is observed in the peak flux density for the different thicknesses. Based on these results, a flux density magnitude of 0.45 T was used for the heat generation model for all test coupon thicknesses.

The flux density for the parallel magnet case at the center of the air gap along the indicated length is shown in Figure 4.9a. The magnitude in this case is fairly constant within about 0.5 inches of center and the peak magnitude is much higher than the alternating magnet case.

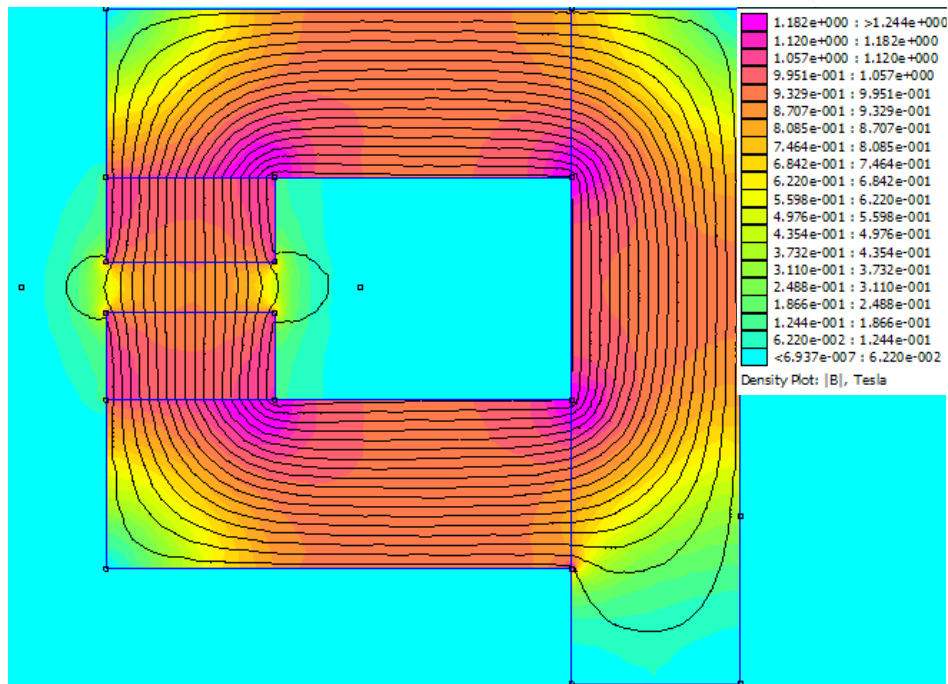
4.3.2 Temperature model

The thermal system model described in Section 2.4 for heat flow due to induction heating was used to predict the steady-state temperature increase of the aluminum test coupons exposed to a

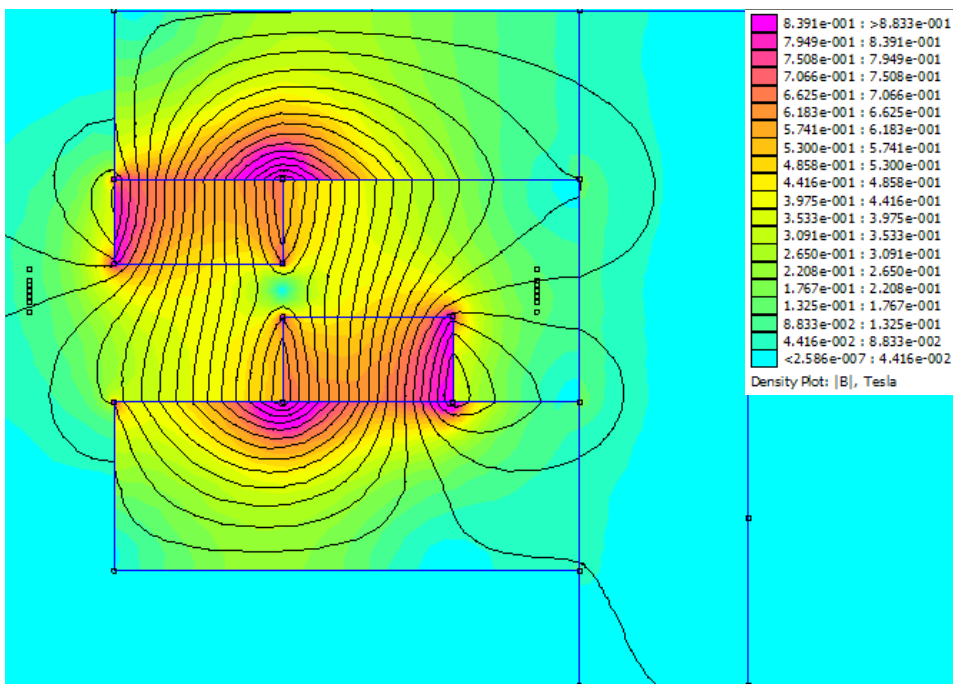
changing magnetic field. The predictions were performed for the alternating magnet configuration and for aluminum test coupons of three different thicknesses. Based on the geometry of the test fixture, the plate area exposed to the magnetic field was taken to be 1 in \times 3 in, and the convection heat transfer coefficient was estimated to be 1000 W/m²°C.

For each coupon thickness, the heating model was used to predict the steady-state temperature increase for relative velocities up to 0.7 m/s. This range of velocities matches that used for the experimental induction heating measurement described in Section 4.4. The data show a quadratic increase in temperature over the velocity range, and an increase in temperature as the plate thickness is increased.

Since increasing the thickness of the test coupon increases the thermal resistance term in the heat flow model, a higher steady-state temperature is achieved for a thicker coupon. However, an increase in thickness also increases the thermal time constant since both the thermal resistance and capacitance are increased. Also note that the calculated temperatures are very sensitive to the value of the convection heat transfer coefficient, which would need to be determined experimentally for the particular experimental setup and environment. The estimated value of the convection coefficient used for this model is used to predict the expected trend in the temperature response.

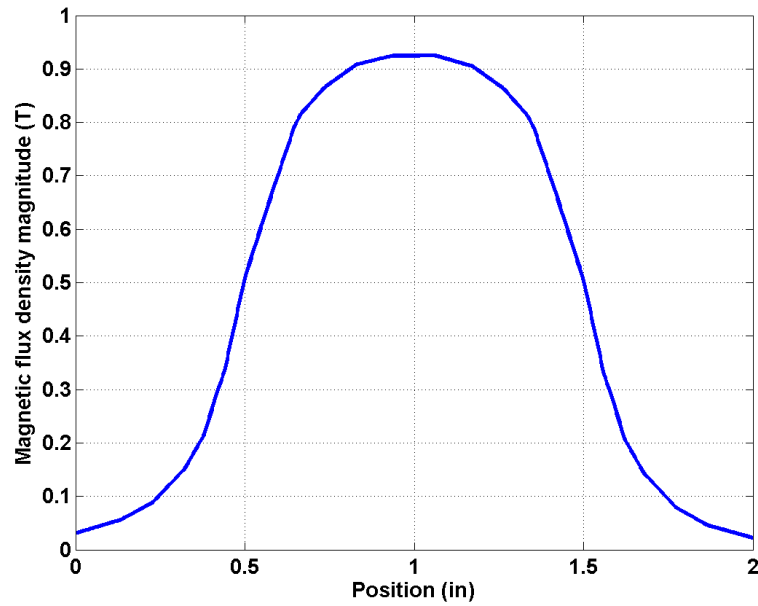


(a) Parallel magnet configuration

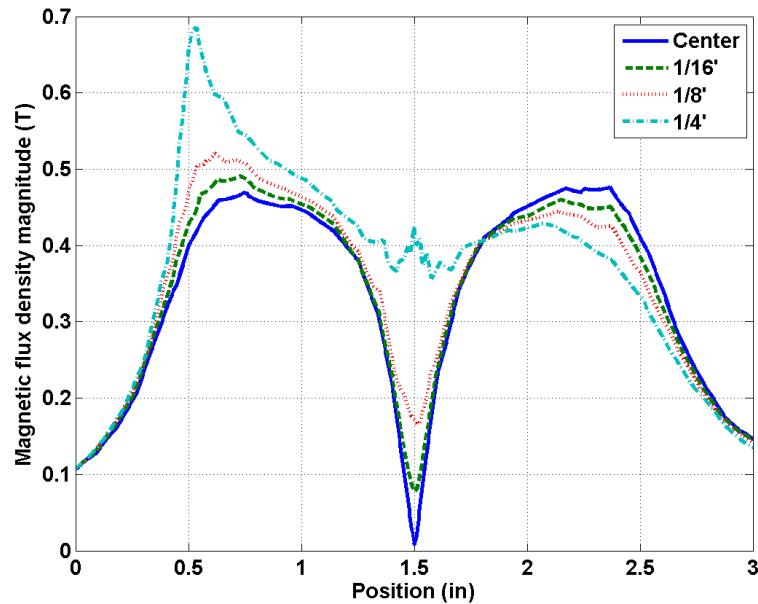


(b) Alternating magnet configuration

Figure 4.8: Magnetic flux density plot for permanent magnet fixture from finite element magnetics analysis



(a) Parallel magnet configuration, center of air gap



(b) Alternating magnet configuration, various plate thicknesses

Figure 4.9: Magnetic flux density along length within air gap of permanent magnet fixture

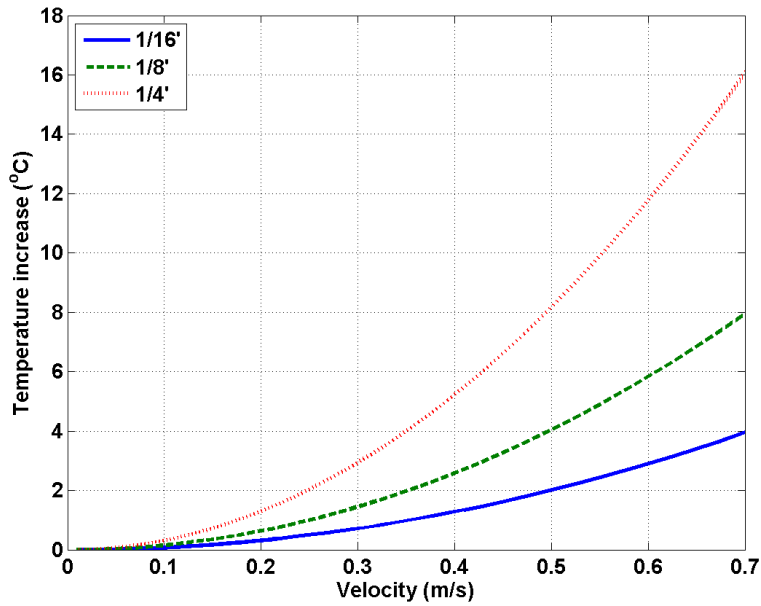


Figure 4.10: Simulated steady-state temperature increase due to induction heating of aluminum plates

4.4 Heat generation measurements

Heat generation from viscoelastic heating and magnetic induction heating were measured using the experimental techniques described in Chapter 3. Results of these measurements are presented in this section.

4.4.1 Viscoelastic heating

A sinusoidal excitation profile was input to the base of the shaker onto which the test article was installed at the experimentally determined natural frequency of 991 Hz. The temperature of the end plate was measured over about 1 hour for two experimental cases. The amplitude of the input acceleration was 3.1 g's for Case 1 and 3.6 g's for Case 2. The measured response for both cases is shown in Figure 4.11 alongside the predicted temperature.

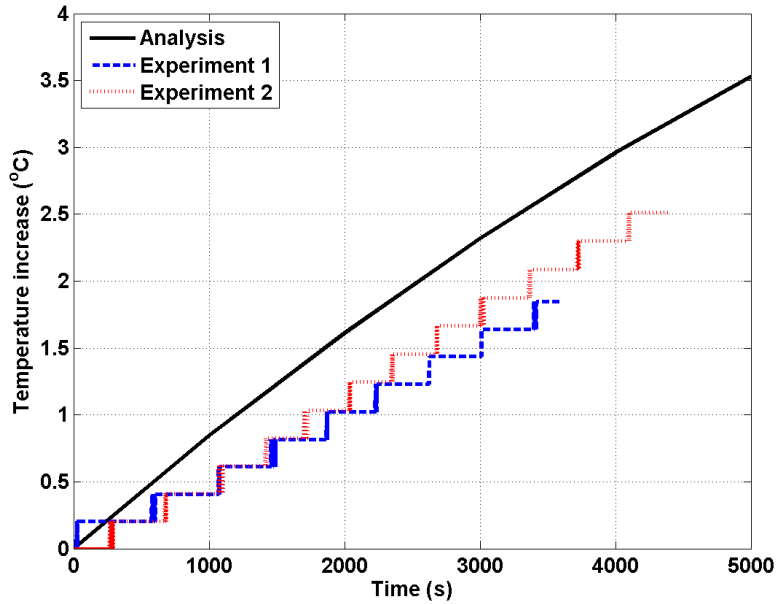


Figure 4.11: Measured VTE test article temperature response to base excitation

As expected, the rate of increase of the measured temperature is slightly less than predicted for the experimental case due in part to more exposed surface area on the test article than assumed for the idealized prediction.

4.4.2 Induction heating

The temperature at the surface of the metal coupon exposed to the vibrating magnetic field was measured and compared to a reference temperature measured on the static fixture. The relative temperature increase between the test coupon and reference temperatures were calculated using the method described in Section 3.2. No temperature increase was measured for the magnet fixture in the parallel configuration on any test coupons.

The base excitation was turned off to allow the metal coupon to cool and stabilize to ambient temperature prior to each measurement. Once a stable temperature was confirmed on the control and monitoring application, the sinusoidal command voltage at the selected frequency and amplitude was output to the amplifier. When the expected frequency and amplitude (as measured by the accelerometer on the shaker base) were observed on the VI, data recording was started. The length of the data record was set to 500 points (approximately 500 s). After completion of data recording, output to the amplifier was discontinued and the heated coupon was allowed to stabilize to ambient temperature in preparation for the next data point.

For each test run, the commanded frequency and amplitude of the base acceleration was constant, and only temperature changes were measured. The magnitude v of the base velocity (measured in m/s) was calculated from the magnitude S_g of the base acceleration (measured in g's) and frequency f (in Hz) using Eq. (4.1). Note that as the frequency is increased, a higher acceleration amplitude is required to achieve the same velocity.

$$v = \frac{S_g \times 9.81}{2\pi f} \quad (4.1)$$

Three different aluminum coupons with thicknesses of 1/16", 1/8", and 1/4" were exposed to the magnetic field and heated by induction. The magnetic fixture was excited at frequencies from 10

Hz to 100 Hz at various amplitudes to achieve a range of base velocities for each configuration. The air gap between the two magnets was set to 5/16" for all runs. The test conditions are summarized in Table 4.9.

Table 4.9: Induction heating test parameters

Parameter	Values
Total air gap	5/16 in.
Coupon thickness	1/16, 1/8, and 1/4 in.
Base frequency	10 - 100 Hz
Base velocity	0.2 - 0.7 m/s
Data record length	500 s

The increase in temperature after 500 s is plotted against base velocity for the three different aluminum coupons in Figure 4.12, from which it was observed that the amount of heat generated increases with increasing velocity and increasing thickness. A second order polynomial (quadratic) function was fit to the temperature vs. velocity data for each thickness, and the fitted curves are also shown in the figure. The point (0 m/s, 0 °C) was added manually to the data set prior to curve fitting.

Representative data for the increase in temperature of a test coupon over time is shown in Figure 3.8, which indicates the temperature increase in the test coupon after 500 s as being close to the final steady-state temperature. The base excitation velocities shown for each test case were repeated with multiple combinations of base acceleration and frequency, and the temperature response was observed to be reproducible for a particular velocity value. The results shown in Figure 4.12 are consistent with the predicted response shown in Figure 4.10.

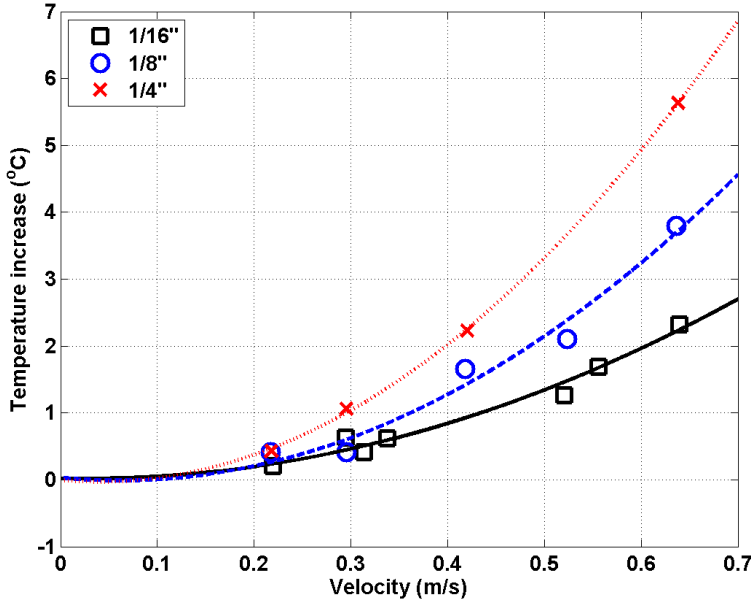


Figure 4.12: Al coupon temperature increase vs. peak base velocity for different coupon thicknesses

4.5 Thermoelectric generator characterization

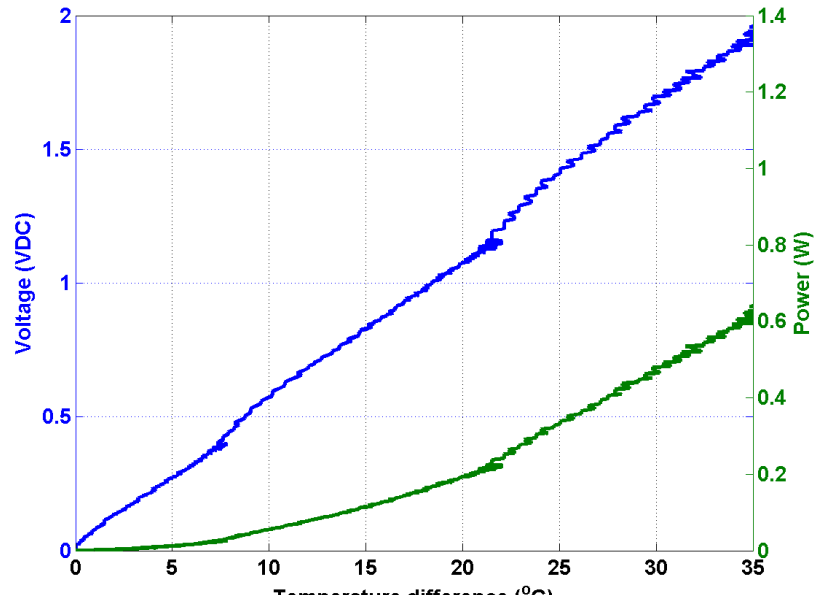
The electrical power output of two TEG's was measured with increasing temperature difference between the hot and cold surfaces of the TEG. For each unit tested, the hot surface temperature was increased incrementally using the hot plate from the starting ambient temperature. The temperature was allowed to settle to an intermediate value then increased to the next incremental level. The voltage output of each TEG was measured across a $6\ \Omega$ resistor as described in Section 3.3.

In the first unit tested, the TEG was integrated into a black-anodized aluminum enclosure with a convective heat sink in contact with the cold surface of the TEG. The measured electrical power output in response to increasing temperature differential is shown in Figure 4.13a. The data show a fairly linear increase in output voltage with temperature; a linear fit to the data resulted in a Seebeck coefficient of $55.8\text{ mV/}^{\circ}\text{C}$ for the insulated TEG. The power output is quadratic with increasing temperature, and about 200 mW of power is generated at $20\text{ }^{\circ}\text{C}$.

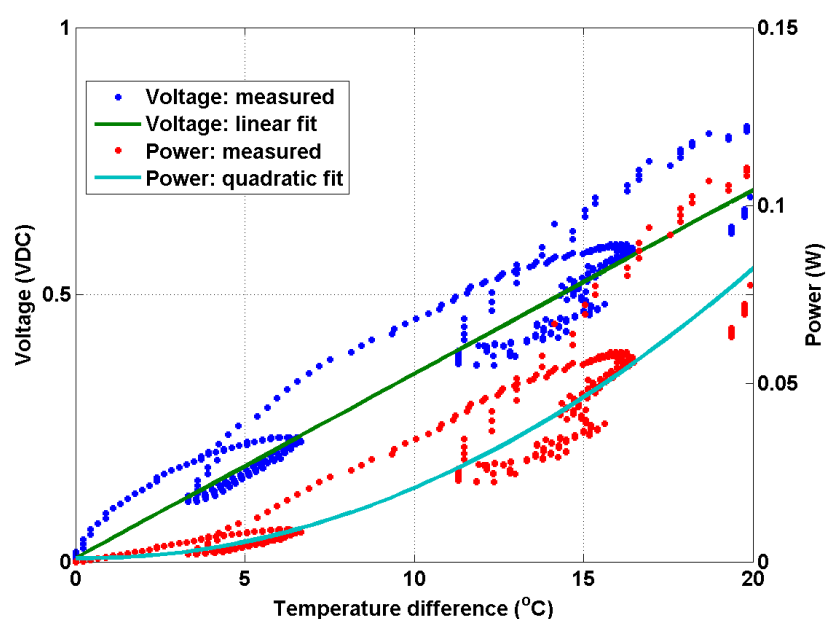
The second unit test was not contained within an insulated enclosure, but a convective aluminum heat sink was placed on the cold TEG surface atop a layer of thermal compound. As a result of heat

loss from the heat sink, the voltage output by the TEG was observed to decrease when the unit was held at a particular temperature. The measured output of this TEG with increasing temperature is shown in Figure 4.13b. A quadratic fit to the power data and linear fit to the voltage data were calculated and are also shown on the plot. The Seebeck coefficient was calculated to be $34.5 \text{ mV}/\text{°C}$ and about 80 mW of power are generated by the unit at a 20 °C temperature differential.

The apparent nonlinearity observed in the temperature response data for the uninsulated TEG results in different Seebeck coefficients for increasing and decreasing temperature differentials. This behavior was also observed in the insulated TEG by decreasing the hot surface temperature and allowing the device to cool. The Seebeck coefficient calculated for the downward temperature test on the insulated unit was $45.4 \text{ mV}/\text{°C}$.



(a) Insulated and enclosed TEG



(b) Uninsulated Marlow TEG

Figure 4.13: Voltage and power response of TEG to increasing surface temperature differential

Chapter 5

Conclusions

A method for harvesting energy from high frequency rotorcraft drive system vibrations is described in this work. The proposed harvesting mechanism converts mechanical energy from harmonic structural vibrations to thermal energy via damping in a tuned linear oscillator. The thermal energy is used to heat a conducting plate, and a thermoelectric generator placed between the heated plate and a heat sink generates electrical energy that can be used to power a wireless sensor node or other device.

A one-dimensional model was developed to describe and model the generation and conduction of heat from an oscillator damped by electromagnetic or viscoelastic forces. Test articles to validate these heating methods were designed and subjected to laboratory tests. Results from the engineering analyses as well as from testing performed on the test articles are summarized in this chapter, and implications of the results and recommendations for future work are discussed.

5.1 Summary of results

For the visco-thermoelectric (VTE) harvester concept, heat generation is achieved by exciting at resonance a linear oscillator whose stiffness and damping are provided by a thin sheet of viscoelastic material. The spring element is independent for the magneto-thermoelectric (MTE) harvester concept and the motion of the oscillator is damped due to eddy currents generated from motion

of a metal plate relative to a permanent magnetic field. Using one-dimensional linear models, expressions were developed for the heat dissipated by linear oscillators damped using both heating methods. An analogous circuit model for transient heat conduction was implemented to model the temperature increase of test articles designed to validate the proposed harvesting method.

5.1.1 Elastomer characterization and heating

Analysis of the viscoelastic heating method showed that decreasing the loss factor and increasing the shear modulus of the elastomer results in increased heat generation and a higher steady-state temperature. While an elastomer with a higher loss factor would generate a greater damping force on the moving mass of the oscillator, the additional damping would also impede the motion of the oscillator thereby reducing the strain energy available to be converted to heat. In addition, the half-power bandwidth at resonance decreases as the loss factor is lowered, and low bandwidth can be undesirable if the base excitation frequency is not exactly matched to the natural frequency of the oscillator, or if the oscillator becomes detuned during operation. For high-frequency operation, an oscillator using a high-stiffness elastomer may also be required to be more massive depending on the geometry of the system.

An elastomer with low loss factor and high stiffness was incorporated into a test article for experimental validation. Characterization of the elastomer revealed an average shear modulus slightly lower than expected based on specified parameters, and the measured shear modulus decreased with increasing base acceleration amplitude. The measured loss factor was also slightly lower than expected from the elastomer specification, and the loss factor was non-linear with increasing base acceleration amplitude. The loss factor was observed to match the specification value for low base acceleration amplitudes.

Driving the VTE test article at resonance resulted in a measurable increase in temperature, with the rate of temperature increase slightly lower than predicted. Partial lack of insulation on areas of the test article is one likely contributer to the lower temperature measured. Detuning of the test article with temperature increase may have also reduced heat generation.

When the shaker system was driven with a sinusoidal signal at a constant commanded amplitude and frequency, some small variations in the base acceleration amplitude were observed. Closed-loop control of the amplifier output and shaker base motion would improve the robustness of the test system. Some increase in the temperature of the shaker system during operation was also observed.

5.1.2 Magnetic induction heating

Predictions of heat generation from the induction heating test fixture were generated using a finite element model of the unit's magnetic circuit. The experimental setup was designed to measure surface heating of an aluminum test coupon fixed relative to the permanent magnetic circuit vibrating on a shaker base. A surface temperature increase was measured for three aluminum coupons of different thicknesses. Steel test coupons were obtained but could not be accommodated by the test fixture due to high attractive magnetic forces.

Results of the induction heating test showed a quadratic increase in the rate of temperature increase of the test coupon with respect to the velocity of the base motion. At a particular velocity, the rate of increase of the surface temperature was observed to increase with increasing test coupon thickness. Higher temperatures of the test coupons could conceivably be achieved by insulating the test coupons, which was not done for this study.

5.1.3 Power generation

Experimental characterization of two TEG's showed quadratically increasing power output with increasing temperature. The output was measured for each unit tested using a 6Ω load resistance, representative of a MicroStrain wireless sensor node. The Seebeck coefficients of both TEG's were observed to be nonlinear and higher for increasing temperature than for decreasing temperature. The power output delivered to a 6Ω load was on the order of 100 mW for a temperature differential of 20 °C between the hot and cold TEG surfaces. However, the power output will vary depending on the actual load, and further characterization of the TEG's at different load resistances is necessary to determine the optimal power output of the units.

5.2 Feasibility

Excitation of the lightly insulated VTE test article at about 3.5 g's at 1 kHz resulted in a linear temperature increase about 2 °C over the first hour. Characterization of two TEG's resulted in Seebeck coefficients of about 35–55 mV/°C with a load resistance of 6 Ω. If two TEG's, each having a Seebeck coefficient of 50 mV/°C, are applied to either end plate on the VTE test article, the measured power output after one hour would be 6.7 mW.

Based on the experimental results, the same temperature increase (2 °C) can also be achieved by the induction heating test fixture in less than 10 min using a plate thickness of 1/4 in and base velocity of 0.4 m/s. However to achieve this velocity at a frequency of 1 kHz, the relative acceleration of the plate relative to the magnetic field would have to be about 250 g's. With a base acceleration of 2.5 g's at 1 kHz, a resonant oscillator with a damping ratio of 0.5 % would be required to achieve this amplitude at resonance. This very lightly damped oscillator would subsequently have a very low operating frequency bandwidth.

These results highlight some serious limitations of the VTE and MTE harvester concepts; namely, slow thermal response and large size with low power output. The VTE design requires several hours to reach its steady-state temperature, and the MTE design requires very high resonant amplification to achieve the necessary relative velocity. However, the results provide an initial starting point on which to base future designs that might use superior materials and optimized device geometry to improve performance.

5.3 Future related research

For the materials and geometry considered for this study, the required time for the VTE harvester design to reach a steady-state temperature was found to be very high (multiple days). Several improvements could be made to the design to increase the heat generated and reduce the thermal time constant. The analytical model showed that an elastomer with a high stiffness and low loss factor is desirable for this application. One possibility for this application might be a flexible

matrix composite (FMC) material, which is an elastomer reinforced by carbon fibers to increase the stiffness of the material [51]. Furthermore, addition of carbon or metal fibers may help to increase the thermal conductivity of an elastomer, which is generally very low compared to that of metal [19].

For the harvester design considered in this study, heat losses due to uninsulated surfaces can significantly decrease the available power output of the device. Further study is required to identify insulating materials optimally suited to this application. In particular, the MTE design requires motion of a metal plate relative to a magnet separated from the plate by a small air gap, which can create a challenge for thermal insulation. One solution might be to apply a thermally insulating coating on the heated metal element.

Another possible modification to the induction heater design is use of a heating element containing some ferrous metal such as steel or iron. Whereas magnetic hysteresis in ferrous metals can result in additional heating from induction [38], steel and iron have lower thermal conductivity than aluminum. Furthermore, requiring motion of a ferrous metal plate in proximity to permanent magnets while maintaining a small air gap would result in some additional design complexity. A possible solution may be a layered material combining a highly conductive non-ferrous metal such as aluminum and a ferrous metal such as steel, as employed by some high-end cookware used with domestic induction heating stoves [37]. Additional study is required to identify the best material or combination of materials for optimization of the permanent magnet induction heater.

The use of a thermoelectric stage may allow for a reduction in complexity of the electrical circuitry associated with the vibration energy harvester, as the use of a rectifier is not required as with a piezoelectric or electromagnetic harvester. Further study regarding optimization of the power conditioning electronics associated with harvesting could lead to more efficient energy harvesting methods.

One potential application of this harvesting concept is to an environment where sources of both thermal and vibration energy are present. In this case, mechanical energy from vibration would be converted to heat using the same methods presented in this study, but the additional heat would

augment the heat generated by the damped oscillator. Other applications may include thermoelectric harvesting of heat generated by tuned vibration absorbers, damped aerospace structures, and motion dampers.

References

- [1] R. Badgley and R. Hartman, "Gearbox noise reduction: prediction and measurement of mesh-frequency vibrations within an operating helicopter rotor-drive gearbox," *Journal of Engineering for Industry*, vol. 96, pp. 567–577, 1974.
- [2] D. Lewicki and J. Coy, "Vibration characteristics of oh-58a helicopter main rotor transmission," NASA Lewis Research Center and Propulsion Directorate, Cleveland, OH, Tech. Rep., April 1987.
- [3] R. Serway, *Physics for Scientists and Engineers with Modern Physics*, 3rd ed. Philadelphia, PA: Saunders College Publishing, 1990.
- [4] P. Glynne-Jones and N. White, "Self-powered systems: A review of energy sources," *Sensor Review*, vol. 21, no. 2, pp. 91–97, 2001.
- [5] S. Priya and D. Inman, *Energy Harvesting Technologies*. New York, NY: Springer Science+Business Media, LLC., 2009.
- [6] D. Griffiths, *Introduction to Electromagnetism*. Upper Saddle River, NJ: Prentice-Hall, Inc., 1999.
- [7] P. Glynne-Jones, M. Tudor, S. Beeby, and N. White, "An electromagnetic, vibration-powered generator for intelligent sensor systems," *Sensors and Actuators A: Physical*, vol. 110, no. 1–3, pp. 344–349, 2004.
- [8] (January 2014) Microstrain energy harvesters. LORD MicroStrain Sensing Systems. Williston, VT. [Online]. Available: <http://www.microstrain.com/energy-harvesting/harvesters>
- [9] D. Santarelli, "An energy harvesting device for powering rotor load monitoring sensors," M.S. thesis, Department of Mechanical Engineering, The Pennsylvania State University, May 2010.
- [10] M. Quintangeli, "An energy harvesting device for powering rotor load monitoring sensors," M.S. thesis, Department of Mechanical Engineering, The Pennsylvania State University, August 2011.
- [11] *IEEE Standard on Piezoelectricity*, IEEE/ANSI Std. 176-1987, 1987.
- [12] J. Sirohi and I. Chopra, "Fundamental understanding of piezoelectric strain sensors," *Journal of Intelligent Material Systems and Structures*, vol. 11, pp. 246–257, 2000.

- [13] A. Erturk, "Electromechanical modeling of piezoelectric energy harvesters," Ph.D. dissertation, Department of Engineering Mechanics, Virginia Polytechnic Institute and State University, November 2009.
- [14] C. Luo, "Active energy harvesting for piezoelectric dynamic systems," Ph.D. dissertation, Department of Electrical Engineering, The Pennsylvania State University, May 2010.
- [15] J. Kauffman, "Low-order modeling of a piezoelectric energy harvesting device," M.S. thesis, Department of Aerospace Engineering, The Pennsylvania State University, December 2007.
- [16] M. Wozniak, "Design, analysis, and characterization of lead magnesium niobate – lead titanate (pmn-pt) single crystal energy harvesters for rotorcraft wireless sensor applications," M.S. thesis, Department of Aerospace Engineering, The Pennsylvania State University, August 2013.
- [17] J. Loverich, S. Wenner, J. Frank, M. Grissom, and E. Smith, "Energy harvester powered wireless accelerometers," in *Proceedings of the American Helicopter Society 67th Annual Forum*, Virginia Beach, VA, May 3–5, 2011.
- [18] W. Zhang, "Modeling and control of magnetostrictive actuators," M.S. thesis, College of Engineering, University of Kentucky, 2005.
- [19] A. Gent, *Engineering with Rubber: How to Design Rubber Components*. New York, NY: Oxford University Press, 2003.
- [20] P. Macioce, "Viscoelastic damping 101," *Sound and Vibration*, vol. 1, pp. 10–12, 2003.
- [21] G. Lesieutre and K. Govindswamy, "Finite element modeling of frequency-dependent and temperature-dependent dynamic behavior of viscoelastic materials in simple shear," *International Journal of Solids and Structures*, vol. 33, no. 3, pp. 419–432, 1995.
- [22] V. Karnaukhov, G. Yakovlev, and L. Goncharov, "Self-heating of viscoelastic materials under cyclic loads," *Strength of Materials*, vol. 7, pp. 164–168, 1975.
- [23] J. deCazenove, D.A.Rade, A.M.G.deLima, and C.A.Araujo, "A numerical and experimental investigation on self-heating effects in viscoelastic dampers," *Mechanical Systems and Signal Processing*, vol. 27, pp. 433–445, 2011.
- [24] V. Madhavan, N. Wereley, and T. Sieg, "Steady state sinusoidal behavior of elastomeric dampers," in *Proceedings of the SPIE Conference on Passive Damping and Isolation*, vol. 3672, Newport Beach, CA, March 1999, pp. 264–274.
- [25] M. Carfagni, E. Lenzi, and M. Pierini, "The loss factor as a measure of mechanical damping," in *Proceedings of the 16th International Modal Analysis Conference*, vol. 1, 1998, pp. 580–584.
- [26] G. Hausmann and P. Gergely, "Approximate methods for thermoviscoelastic characterization and analysis of elastomeric lead-lag dampers," in *Proceedings of the 18th European Rotorcraft Forum*, Avignon, France, September 15–18, 1992.

- [27] L. Byers, "Experimental and analytical investigation of the thermomechanical behavior of elastomeric materials," M.S. thesis, Department of Aerospace Engineering, The Pennsylvania State University, May 1997.
- [28] C. Brackbill, G. Lesieutre, E. Smith, and K. Govindswamy, "Thermomechanical modeling of elastomeric materials," *Smart materials and structures*, vol. 5, pp. 529–539, 1996.
- [29] J. Szefi, "Helicopter gearbox isolation using periodic layered fluidic isolators," Ph.D. dissertation, Department of Mechanical Engineering, The Pennsylvania State University, August 2003.
- [30] H. Sodano and J. Bae, "Eddy current damping in structures," *The Shock and Vibration Digest*, vol. 36, no. 6, pp. 469–478, 2004.
- [31] H. Wiederick, N. Gauthier, D. Campbell, and P. Rochon, "Magnetic braking: Simple theory and experiment," *American Journal of Physics*, vol. 55, pp. 500–503, 1987.
- [32] J. Edwards, B. Jayawant, W. Dawson, and D. Wright, "Permanent-magnet linear eddy-current brake with a non-magnetic reaction plate," *IEE Proc.-Electr. Power Appl.*, vol. 146, no. 6, pp. 627–631, November 1999.
- [33] D. Liu, "Validation of eddy current loss models for permanent magnet machines with concentrated windings," Masters thesis, Electrical Power Processing, Delft University of Technology, August 2012.
- [34] L. McCarthy, "On the electromagnetically damped mechanical harmonic oscillator," *American Journal of Physics*, vol. 64, no. 7, pp. 885–891, 1996.
- [35] H. Sodano, J. Bae, D. Inman, and W. Belvin, "Concept and model of eddy current damper for vibration suppression of a beam," *Journal of Sound and Vibration*, vol. 288, pp. 1177–1196, 2005.
- [36] P. Simpson, *Induction Heating: Coil and System Design*. New York, NY: McGraw-Hill Book Company, Inc., 1960.
- [37] W. Moreland, "The induction range: Its performance and its development problems," *Transactions on Industry Applications*, vol. IA-9, no. 1, pp. 81–85, January/February 1973.
- [38] R. Haimbaugh, *Practical Induction Heat Treating*. Materials Park, OH: ASM International, 2001.
- [39] E. Davies, *Conduction and Induction Heating*. London, United Kingdom: The Institution of Engineering and Technology, 2007.
- [40] R. Bogue, "Energy harvesting and wireless sensors: a review of recent developments," *Sensor Review*, vol. 29, no. 3, pp. 194–199, 2009.
- [41] S. Brennan, A. Bronowicki, and S. Simonian, "Cryo magnetic damping: Material characterization and damping demonstration," in *Proceedings of the 48th AIAA/ASME/ASCE/AHS/ASC Structures, Structural Dynamics, and Materials Conference*, Honolulu, HI, April 23–26, 2007.

- [42] L. Zuo, X. Chen, and S. Nayfeh, “Design and analysis of a new type of electromagnetic damper with increased energy density,” *Journal of Vibration and Acoustics*, vol. 133, 2011.
- [43] M. Perry, “Eddy current damping due to a linear periodic array of magnetic poles,” *IEEE Transactions on Magnetics*, vol. 20, pp. 149–155, 1984.
- [44] Y. Cengel, *Heat Transfer: A Practical Approach*, 2nd ed. New York, NY: The McGraw-Hill Companies, Inc., 2003.
- [45] G. Rizzoni, *Principles and Applications of Electrical Engineering*, 5th ed. New York, NY: The McGraw-Hill Companies, Inc., 2007.
- [46] D. Meeker. (October 2013) Finite element method magnetics. Software package, version 4.2. [Online]. Available: <http://www.femm.info>
- [47] (November 2008) Lord 320/322 epoxy adhesive. Technical data. LORD Corporation. Cary, NC. [Online]. Available: http://www.chembar.com/content/lord_320-322_data.pdf
- [48] P. Torvik, “On estimating system damping from frequency response bandwidths,” *Journal of Sound and Vibration*, vol. 330, pp. 6088–6097, 2011.
- [49] (January 2014) Eh-link energy harvesting wireless node. LORD MicroStrain Sensing Systems. Williston, VT. [Online]. Available: <http://www.microstrain.com/energy-harvesting/eh-link>
- [50] R. Mahmood, E. Smith, and G. Lesieutre, “A visco-electric device for vibration energy harvesting on rotorcraft,” in *Proceedings of the 22nd AIAA/ASME/AHS Adaptive Structures Conference*, National Harbor, MD, January 13–17, 2014.
- [51] T. Henry, “Static and dynamic characterization of composite materials for future driveshaft systems,” M.S. thesis, Department of Aerospace Engineering, The Pennsylvania State University, May 2012.

Appendix A

MATLAB Code

A.1 Temperature prediction from heating model

A.1.1 VTE test article response

```
% Initial notional prediction cases
% Steady-state temperature response
clear,clc,close all
addpath RefFunctions

%% user spec params
% Base
accel.ampl= 6;
f0_hz= 1e3;

% Elastomer
for G= [40e6 170e6];
eta= 0.01;

w_elas= 70e-3;
t_elas= 10e-3;

% Conductor
t_cond= 10e-3;
K_A1= 210;

disp(['Modulus: ' num2str(G*1e-6) ' MPa'])
disp(['Loss factor: ' num2str(eta)])

%% derived
A_elas= w_elas^2;
w0= 2*pi*f0_hz;
S= accel.ampl*9.81/w0^2;
zeta= 2*eta/2; %oscillator has 2 dampers
k= A_elas*G/t_elas;
% RT.cond= t_cond/(K_A1*A_elas);

% RT.cond= 3;
RT.cond= 0.3;

disp(['Acceleration: ' num2str(accel.ampl) ' g''s at ' num2str(f0_hz) ' Hz'])
disp(['Displacement amplitude: ' num2str(S*1e6) ' um'])
disp(['Total elastomer stiffness: ' num2str(k*1e-6) ' MN/m'])

%% sizing
m= k/w0^2;
disp(['Moving mass: ' num2str(m) ' kg'])

%% define functions
```

```
% oscillator amplitude at res
A_wn= @(S,zeta) (S./(2i*zeta));

% energy dissipation per cycle at res (each elas)
Qcyc= @(A,S,k,eta) (pi*eta*k.*abs(A-S).^2);

%% Prediction
% amplitude at resonance
A_res= A_wn(S,zeta);
R_wn= abs(A_res)/S;
disp(['Amplification (A/S) = ' num2str(R_wn)]);

Qcyc_res= Qcyc(A_res,S,k,eta); % at resonance
disp(['Energy dissipation per cycle = ' num2str(Qcyc_res*1e3) ' mJ']);

Qd_gen= Qcyc_res*f0_hz;
disp(['Power dissipation per cycle = ' num2str(Qd_gen) ' W']);

%% steady-state temp
deltaT= RT.cond*Qd_gen;
disp(['Steady-state temp increase = ' num2str(deltaT) ' degC']);

disp('---')
end
```

```
% Initial notional prediction cases
% Thermal circuit parameters for transient temperature model
clear,clc,close all
addpath RefFunctions

%% test article geometry
elas.length= 75e-3;
elas.thickness= 10e-3;

endplate.length= 75e-2;
endplate.thickness= 10e-2;

insul.length= endplate.length;
% insul.thickness= 5e-2;
insul.thickness= 0.5e-2;

%% material properties
Cp_1018= 486; K_1018= 51.9; rho_1018= 7870;
Cp_Al= 900; K_Al= 210; rho_Al= 2700;
Cp_elas= 2000; K_elas= 1.2; rho_elas= 1500;
Cp_insul= 1250; K_insul= 0.03; rho_insul= 480;

%% mass dims
% m= 0.49647;
m= 2.11;

m_vol= m/rho_1018;
m_length= elas.length;
m_thickness= m_vol/(m.length^2)

%% test article w/ central mass
Axz= [m.length elas.length endplate.length insul.length].^2;
Ly= [m.thickness elas.thickness endplate.thickness insul.thickness];
rho= [rho_1018 rho_elas rho_Al rho_insul];
Cp= [Cp_1018 Cp_elas Cp_Al Cp_insul];
K= [K_1018 K_elas K_Al K_insul];

[Rt,Ct]= tempcircut(Axz,Ly,rho,Cp,K)
timeconst= Rt.*Ct
```

```
% Experimental VTE test article
% Steady-state temperature response
clear,clc,close all
addpath RefFunctions

%% user spec params
accel_ampl= 3;
RT.cond= 19.685;

w_elas= 4*2.54e-2;
t_elas= 1/16*2.54e-2;

% Conductor
```

```

t_cond= 1/8*2.54e-2;
K_Al= 210;

%%
for kase= 1:2
switch kase
case 1
disp('spec')
G= 3.17e6; eta= 0.08; f0_hz= 1e3;
case 2
disp('experiment')
G= 3.11e6; eta= 0.063; f0_hz= 991;
end

disp(['Modulus: ' num2str(G*1e-6) ' MPa'])
disp(['Loss factor: ' num2str(eta)])

%% derived
A_elas= w_elas^2;
w0= 2*pi*f0_hz;
S= accel_ampl*9.81/w0^2;
zeta= 2*eta/2; %oscillator has 2 dampers
k= A_elas*G/t_elas;
% RT_cond= t_cond/(K_Al*A_elas);

disp(['Acceleration: ' num2str(accel_ampl) ' g''s at ' num2str(f0_hz) ' Hz'])
disp(['Displacement amplitude: ' num2str(S*1e6) ' um'])
disp(['Total elastomer stiffness: ' num2str(k*1e-6) ' MN/m'])

%% sizing
m= K/w0^2;
disp(['Moving mass: ' num2str(m) ' kg'])

%% define functions
% oscillator amplitude at res
A_wn= @(S,zeta) (S./(2i*zeta));

% energy dissipation per cycle at res (each elas)
Qcyc= @(A,S,k,eta) (pi*eta*k.*abs(A-S).^2);

%% Prediction
% amplitude at resonance
A_res= A_wn(S,zeta);
R_wn= abs(A_res)/S;
disp(['Amplification (A/S) = ' num2str(R_wn)])

Qcyc_res= Qcyc(A_res,S,k,eta); % at resonance
disp(['Energy dissipation per cycle = ' num2str(Qcyc_res*1e3) ' mJ'])

Qd_gen= Qcyc_res*f0_hz;
disp(['Power dissipation per cycle = ' num2str(Qd_gen) ' W'])

%% steady-state temp
deltaT= RT_cond*Qd_gen;
disp(['Steady-state temp increase = ' num2str(deltaT) ' degC'])

disp('---')
end

```

```

% Experimental VIE test article
% Thermal circuit parameters for transient temperature model
clear,clc,close all
addpath RefFunctions

%% test article geometry
elas_length= 4*2.54e-2;
elas_width= 1/16*2.54e-2;

ctrplate_width= 0.253*2.54e-2;
ctrplate_length= 4*2.54e-2;

endplate_width= 1/8*2.54e-2;
endplate_length= 5*2.54e-2;

insul_width= 0.5*2.54e-2;
insul_length= 5*2.54e-2;

% material properties
Cp_1018= 486; K_1018= 51.9; rho_1018= 7870;
Cp_Al= 900; K_Al= 210; rho_Al= 2700;
Cp_elas= 2000; K_elas= 1.2; rho_elas= 1500;
Cp_insul= 1250; K_insul= 0.04; rho_insul= 480;

```

```

%% test article w/ central mass
% [1/2 steel mass, elastomer, end plate, insulation]
Axz= [ctrplate.length^2 elas.length^2 endplate.length^2 insul.length^2];
Ly= [ctrplate.width elas.width endplate.width insul.width];
rho= [rho.1018 rho.elas rho.Al rho.insul];
Cp= [Cp.1018 Cp.elas Cp.Al Cp.insul];
K= [K.1018 K.elas K.Al K.insul];

[Rt,Ct]= tempcircuit(Axz,Ly,rho,Cp,K)
timeconst= Rt.*Ct

```

A.1.2 MTE test article response

```

% Induction heating model
clear,clc,close all
addpath RefFunctions

thickness= [1/16 1/8 1/4];
deltaT= zeros(3,1e3);
for n= 1:length(thickness)
    freq= linspace(5,500,1e3);
    accel= 3*9.81;

    w= 2*pi*freq;
    vel= accel./w;

    Bz= 0.45;
    H_conv= 1000;

    sigma= 2.5e7; %Al 6061
    K= 167; cp= 0.896e-3; rho= 2700;

    hz= thickness(n)*2.54e-2;
    hx= 1*2.54e-2; hy= 3*2.54e-2;

    A= accel./w.^2;
    vol= hx*hy*hz;

    Qcyc= pi*sigma*Bz^2*vol*w.*A.^2;
    Qdotcyc= Qcyc./(2*pi./w);

    [Rt,Ct]= tempcircuit(hx*hy,hz,rho,cp,K);
    R_convec= 1./ (H_conv*hx*hy);

    deltaT(n,:)= (Rt+2*R_convec)*Qdotcyc;
end

```

A.2 Data analysis

A.2.1 Elastomer characterization

```

% Generate transfer function model from characterization test data
% Import data from CSV file generated by control & measurement VI
% Run this script on each data file individually to consolidate data into echardat.mat
clear,clc,close all
addpath RefFunctions

% user options
samplerate= 10.24e3; dwnsamp= 2; Fs= samplerate/dwnsamp;
IOchans= [3 4]; IOsens= [10.73 50e-3];
filtfrcqs= [200 2000];
avgspan_hz= 50;

%% raw data import and plot
[datfile,datpath]= uigetfile('*.csv');
filtdata= grabAIOdata(datpath,datfile,samplerate,dwnsamp,IOchans,IOsens,filtfrcqs,[]);
SysModel.Plots(filtdata.accel,filtdata.vel,samplerate/dwnsamp)

```

```

%% generate model
[f,systf,esttf0,esttf1]= TFModelGen(filtdata.vel,filtdata.accel,Fs);
% [Cx,y,F]= mscohere(filtdata.vel,filtdata.accel,[],[],2^nextpow2(10*length(filtdata.accel)),Fs);

%% save data
saveme= 1;
if saveme
global echardat
if isempty(echardat), n= 1; else n= length(echardat)+1; end
echardat{n}.datfile= datfile; echardat{n}.accel.in= filtdata.accel; echardat{n}.vel.out= filtdata.vel;
echardat{n}.f= f; echardat{n}.Fs= Fs; echardat{n}.systf= systf; echardat{n}.esttf0= esttf0; echardat{n}.esttf1= esttf1;
save('echardat','echardat'), disp(['Saved ' datfile ' to column ' num2str(n)])
end

%% bode plot
mag= abs(systf); phs= unwrap(angle(systf))*180/pi;

avgspan= round(length(f)/f(end)*avgspan_hz);
mag2= smooth(mag,avgspan); phs2= smooth(phs,avgspan);

[emag0,eph0]= bode(esttf0,2*pi*f);
mag3= squeeze(emag0); phs3= unwrap(squeeze(eph0));

[emag1,eph1]= bode(esttf1,2*pi*f);
mag4= squeeze(emag1); phs4= unwrap(squeeze(eph1));

%% calculate elastomer properties
[fn,zeta]= calcdamping(f,mag2,phs2,filtfreqs,1);

% device geometry
mass= 1.044;
w_elas= 4*2.54e-2;
t_elas= 1/16*2.54e-2;

eta= mean(zeta);
k= (2*pi*fn)^2*mass;
G= k*t_elas/(2*w_elas^2);

disp(['Estimate: fn= ' num2str(fn) ', zeta= ' num2str(zeta)])
disp(['loss factor = ' num2str(eta) ', stiffness = ' num2str(k) ', modulus = ' num2str(G)])

```

```

% Prepare transfer function data from elastomer characterization tests for comparision
% Import consolidated data file echardat.mat
clc,clear,close all
addpath RefFunctions
load echardat

% processing params
avgspan_hz= 50;
frange= [500 1500];
mass= 1.045;
w_elas= 4*2.54e-2;
t_elas= 1/16*2.54e-2;

% preallocate
fn= zeros(length(echardat),1); zeta= zeros(length(echardat),2);
peakmag= fn; avgpwr= fn;

%% analyze cases
for n= 1:length(echardat)
f= echardat{n}.f;
mag.raw= abs(echardat{n}.systf); phs.raw= unwrap(angle(echardat{n}.systf))*180/pi;

avgspan= round(length(f)/f(end)*avgspan_hz);
mag= smooth(mag.raw,avgspan); phs= smooth(phs.raw,avgspan);

[fn(n),zeta(n,:),peakmag(n)]= calcdamping(f,mag,phs,frange,0);
avgpwr(n)= npsd(echardat{n}.accel.in,echardat{n}.Fs,frange);
end

%% loss factor
eta= mean(zeta,2); %averaged
% eta= zeta(:,1); %bandwidth only

%% parameter comparison
eta.spec= 0.08;
% G.spec= 460;
% G.psi= G*0.000145037738;
fn.spec= 1e3;

rnd.ampl= [0.025 0.05 0.075 0.1 0.15];

```

```

rnd_idx= [7 8 9 5 6]-1;
chr_ampl= [0.025 0.05 0.075 0.1];
chr_idx= [10 11 12 4]-1;

%% averages
eta_avg= mean([eta(rnd_idx); eta(chr_idx)])
fn_avg= mean([fn(rnd_idx); fn(chr_idx)])

k_avg= (2*pi*fn_avg).*2*mass/2
G_avg= k_avg*t_elas./(w_elas.^2)
Gpsi_avg= G_avg.*0.000145037738

```

A.2.2 Heating tests

```

% Import and save CSV data from induction heating test to magtempdata.mat
% Select each folder containing data to augment to file
clear,clc,close all
addpath RefFunctions

tempchans= [1 2]; IOchans= [3 4];
avgtime= 2; reclength= 500;

%% specify path and identify test case
datpath= uigetdir();
datfiles= ls(datpath '\0*.csv');
path_idx= regexp(datpath, '\');
testid= datpath(path_idx(end)+1:end);

%% parse files
freq= zeros(1,size(datfiles,1)); ampl= freq; Tfin= freq; vel= freq;
Trel= zeros(reclength,size(datfiles,1)); Tref= Trel; Thot= Trel; time= Trel;
proadata= cell(1,size(datfiles,1));
for n= 1:size(datfiles,1)
[~,proadata{n}]= grabAIOdata([datpath '\'],datfiles(n,:),[],0,IOchans,[],[],tempchans);
Tref(:,n)= proadata{n}.temp(:,1); Thot(:,n)= proadata{n}.temp(:,2);
[Trel(:,n),Tfin(n)]= calctempdiff(Tref(:,n),Thot(:,n),avgtime);
freq(n)= mean(proadata{n}.freq(:,1)); ampl(n)= mean(proadata{n}.ampl(:,1));
vel(n)= 9.81*ampl(n)./(2*pi*freq(n));
time(:,n)= proadata{n}.time;
end

%% collect values into structure
if exist('magtempdata.mat','file')
load magtempdata
else %create on first call
magtempdata= struct([]);
end
stridx= length(magtempdata)+1; %augment imported structure
magtempdata{stridx}.time= time;
magtempdata{stridx}.Tref= Tref; magtempdata{stridx}.Thot= Thot;
magtempdata{stridx}.Trel= Trel; magtempdata{stridx}.Tfin= Tfin;
magtempdata{stridx}.freq= freq; magtempdata{stridx}.ampl= ampl;
magtempdata{stridx}.vel= vel; magtempdata{stridx}.testid= testid;
save('magtempdata','magtempdata')

```

```

% Prepare consolidated induction heating test data for plotting
% Import data from magtempdata.mat
clear,clc,close all
addpath RefFunctions
load magtempdata

%% interpolate temp vs. velocity
velrange= linspace(0,0.7,1e3); temp_fit= velrange;
vel_sort= cell(1,length(magtempdata)); temp_sort= vel_sort;
for n= 1:length(magtempdata)
[temp_fit(n,:),vel_sort{n},temp_sort{n}]= datafit(magtempdata{n}.vel,magtempdata{n}.Tfin,velrange,2);
end

```

A.2.3 Referenced functions

```

function [filtdata,procdata]= grabAIOdata(datpath,datfile,samplerate,dwnsamp,IOchans,IOsens,filtfrcqs,tempchans)
% Import CSV data saved by control & measurement VI for analysis

%% Raw data
if ~isempty(samplerate)
accelchan= IOchans(1); velchan= IOchans(2);
accelsens= IOsens(1); velsens= IOsens(2);

dat.raw= importdata([datpath datfile]);

acceldata= accelsens*detrend(dat.raw(:,accelchan));
veldata= velsens*detrend(dat.raw(:,velchan));

if dwnsamp~=0
samplerate= samplerate/dwnsamp;
acceldata= decimate(acceldata,dwnsamp);
veldata= decimate(veldata,dwnsamp);
end

% filter
[b,a]= butter(4,filtfrcqs/(samplerate/2));
filtdata.accel= filtfilt(b,a,acceldata);
filtdata.vel= filtfilt(b,a,veldata);
else
filtdata= [];
end

%% Processed data
% thermistor circuit parameters
R_ref= 2.32e3; V_ex= 0.5;

if ~isempty(tempchans) %also grab processed data
dat.proc= importdata([datpath 'proc' datfile]);
procdata.time= dat.proc(:,1)/1e3;

therm.V= dat.proc(:,procdatacolumn(tempchans,3));
procdata.temp= tempcalc(therm.V,R.ref,V.ex);

procdata.freq= dat.proc(:,procdatacolumn(IOchans,1));
procdata.ampl= dat.proc(:,procdatacolumn(IOchans,2));
else
procdata= [];
end

function therm.T= tempcalc(therm.V,R.ref,V_ex)
therm.R= R.ref.*therm.V./(V_ex-therm.V); %resistance
therm.T= ThermistorTempCalc(therm.R,'C'); %temperature

function columnns= procdatacolumn(chans,measnum)
% calculate processed data column number for specified channel (1-4)
% and measurement on that channel (1-3)
% measurements on each channel are [frequency amplitude offset]
% time is in the first column
meas.cols= 3*[0 1 2 3]+1+measnum;
columnns= meas.cols(chans);

```

```

function [f,systf,esttf0,esttf1]= TFModelGen(output.vel,input.accel,Fs)
% generate 2nd order transfer function model between (output) velocity
% response data (from LDV) and (input) base acceleration data

% input time data and convert to freq domian
sysdata= iddata(output.vel,input.accel,1/Fs);
sysfreqdata= fft(sysdata);
angfreqs= get(sysfreqdata,'Frequency');
freqdata.vel= get(sysfreqdata,'OutputData');
freqdata.accel= get(sysfreqdata,'InputData');

% scale velocity to match units of acceleration
freqdata.input= freqdata.accel;
freqdata.output= freqdata.vel*li.*angfreqs/9.81;
sysfreqdata.scaled= iddata(freqdata.output,freqdata.input,1/Fs,'Frequency',angfreqs);
sysdata.scaled= ifft(sysfreqdata.scaled);

accel.out= get(sysdata.scaled,'OutputData');
accel.in= get(sysdata.scaled,'InputData');

time= linspace(0,length(output.vel)/Fs,length(output.vel));
T= time(end);

%% generate the tf
% SysID method

```

```

esttf0= tfest(sysfreqdata.scaled,2,0);
esttf1= tfest(sysfreqdata.scaled,2,1);

% discrete method
nfft= 2^nextpow2(10*Fs*T);
overlap= 2^nextpow2(Fs*T/1000);
nwin= 2^nextpow2(Fs*T/100);
win= rectwin(nwin);
[sysf,f]= tfeestimate(accel.in,accel.out,win,overlap,nfft,Fs);

```

```

function [fn,zeta,peakmag,hpband,Qfactor]= calcdamping(freq,mag,phs,frange,plotme)
% calculate damping ratio and natural frequency from frf data
% optionally specify frequency range [fmin fmax] in Hz for search
% generate bode plot if requested

if ~isempty(frange)
fidx= find(freq>=frange(1),1,'first'):find(freq<=frange(2),1,'last');
freqz= freq(fidx); magz= mag(fidx); phsz= phs(fidx);
else
freqz= freq; magz= mag; phsz= phs;
end

max_idx= find(magz==max(magz));
assert(max_idx>2 && max_idx<length(magz)-1,'Peak not in range')
assert(magz(max_idx)>magz(max_idx+1) && magz(max_idx)>magz(max_idx-1),'Peak not found');

fn= freqz(max_idx);
peakmag= max(magz);

%% half power method
half_idx_all= find(magz>=(max(magz)/sqrt(2)));
dhidx= diff(half_idx_all);
if any(dhidx~=1) %ignore secondary peak
% half_idx_below= half_idx_all(1:find(dhidx~=1,1));
half_idx_above= half_idx_all(find(dhidx~=1)+1:end,1);
half_idx_range= half_idx_above;
else
half_idx_range= half_idx_all;
end

half_idx= [half_idx_range(1) half_idx_range(end)];
zeta(1)= (freqz(half_idx(2))-freqz(half_idx(1)))/(2*freqz(max_idx));

hpband= freqz(half_idx(2))-freqz(half_idx(1));
Qfactor= fn/hpband;

%% phase slope method
pres= 5; %+- Hz for slope calculation
pnum= max(5,round(length(freqz)/freqz(end)*pres)); %use at least 5 pts
pidx= [max_idx-pnum max_idx+pnum];
pslope= (pi/180)*(phsz(pidx(2))-phsz(pidx(1)))/(2*pi*(freqz(pidx(2))-freqz(pidx(1))));
zeta(2)= -1/(2*pi*freqz(max_idx)*pslope);

%% plot (for debugging!)
if plotme
figure,subplot 211
plot(freqz,squeeze(magz)),grid on
line(freqz(half_idx),magz(half_idx),'color','r','linewidth',3)
line(freqz([1 end]),[peakmag peakmag],'color','g')
subplot 212,plot(freqz,squeeze(phsz)),grid on
line(freqz(pidx),phsz(pidx),'color','r','linewidth',3)
line(freqz([1 end]),[0 0],'color','g')
line(freqz([1 end]),[-90 -90],'color','g')
line(freqz([1 end]),[-180 -180],'color','g')
end

```

```

function [avgpwr,psdest]= npsd(sig,Fs,fband)
% calculate psd estimate and integrate over specified frequency range to
% get G-RMS of acceleration data

[psdest,f]= pwelch(sig,[],[],[],Fs);
fidx= find(f>=fband(1),1,'first'):find(f<=fband(2),1,'last');
avgpwr= sqrt(trapz(f(fidx),psdest(fidx)));

```

```

function [yfit,xsort,ysort]= datafit(xdat,ydat,xrange,fitord)

```

```
% sort data and apply polynomial fit of specified order  
% add (0,0) as a data point  
% return evaluated polynomial and sorted data  
  
[xsort,sortidx]= sort(xdat);  
ysort= ydat(sortidx);  
pol= polyfit([0 xsort],[0 ysort],fitord);  
yfit= polyval(pol,xrange);
```

Appendix B

LabVIEW Code

The top-level block diagram for the LabVIEW Virtual Instrument (VI) used for control, monitoring, and data acquisition is shown on the following page. A description of the VI front panel, capabilities of the software, and instructions for use are given in Chapter 3.

